NANOPARTICLE PRECONDITIONING FOR ENHANCED THERMAL THERAPIES IN CANCER

A DISSERTATION
SUBMITTED TO THE FACULTY OF THE GRADUATE SCHOOL
OF THE UNIVERSITY OF MINNESOTA
BY

Mithun M. Shenoi

IN PARTIAL FULFILLMENT OF THE REQUIREMENTS
FOR THE DEGREE OF
DOCTOR OF PHILOSOPHY

ADVISER: JOHN C. BISCHOF

December 2011

Acknowledgements

As the saying goes, it takes a village to raise a child. During my time in graduate school I have had the good fortune of interacting with and receiving the guidance of several individuals who have helped shape my fledgling career.

First of all, I am grateful to my adviser, Dr. John Bischof, who has been a source of knowledge, motivation and support. His passion for the research we do is infectious and has got me through some difficult phases of my experimental work. He has allowed me to make the mistakes I needed to make and learn from them. Undoubtedly, his mentorship has helped me grow as a researcher.

I thank my committee members – Dr. Erik Cressman, Dr. Alison Hubel, Dr. Robert Tranquillo and Dr. Gregory Vercellotti – for their guidance and critique that has enabled me to focus my research.

The majority of the work presented in this thesis would not have been possible without collaboration with several labs. I would like to thank Colleen Forster, Jonathan Henriksen and Dr. Stephen Schmechel at BioNet; John Oja and Jerry Sedgewick at Biomedical Image Processing Lab; Krista Walkowiak and Diana Freeman at Research Animal Resources; Dan Busian, Andrew Fenske and Kelly Fischenic at Fairview University Medical Center – Interventional Radiology; John Belcher and Paul Marker at the Vercellotti lab; Dr. Paul Iaizzo and Bill Gallagher at the Visible Heart Lab; Dr. Kyle Anderson, Dr. Renato Pedro and Dr. Kishore Thekke-Adiyat at Urological Surgery; Dr. Giulio Paciotti at CytImmune Sciences,Inc.; Dr. Greg Metzger and Dr. Devashish

Shrivastava at the Center for Magnetic Resonance Research; and Matt Lahti at Experimental Surgical Services.

I thank the administration of the Medical Scientist Training Program – Dr. Tucker Lebien, Dr. Peter Bitterman, Dr. Yoji Shimizu, Susan Shurson and Nick Berg – for funding and support during my years in the program.

I would not have enjoyed my time in lab without the friendship of past and present members of the Bischof lab group. Thanks to Dr. Jeunghwan Choi, Dr. Hossam El-Khalil, Michael Etheridge, Dr. Raghav Goel, Dr. Jing Jiang, Zhenpeng Qin, Dr. Neha Shah, and Dr. Ramji Venkatasubramanian. Outside of lab, I am grateful to my flag football and cricket team members who have made the weekends quite memorable. I am grateful for the friendship of Hemant, Michelle, Mike and Tanner who have shared the ups and downs of the "MudPhud" journey with me.

This thesis would not have been possible without the belief and support of my parents. Any gratitude I could possibly show them would pale in comparison to all that they have done for me. Lastly, I am grateful to my better half, Devi, for her love, humor and support while always keeping the important things in life in perspective for me.

To My Parents & Devi

Abstract

Nanoparticles show tremendous promise in the safe and effective delivery of molecular adjuvants to enhance local cancer therapy. One important form of local cancer treatment that suffers from local recurrence and distant metastases is thermal therapy. A new concept involving the use of nanoparticle-delivered adjuvants to 'precondition' (alter the vascular and immunological biology) tumors to enhance their susceptibility to thermal therapy has been developed in our lab. Previous work has demonstrated nanoparticle preconditioning of thermal therapies (heat and cold) by a single systemic injection of PEG-coated gold nanoparticles tagged with a vascular targeting agent (TNF-α). In addition, mechanistic studies have shown that 4 hour pre-treatment with native TNF-α induced vascular preconditioning including the up regulation of inflammation (NF-κB) and apoptotic (caspase) pathways accompanied by an intense recruitment of neutrophils. Based on these findings, we hypothesized that vascular preconditioning of nanoparticle-delivered TNF-α is mediated by tumor endothelial (NF-κB) activation leading to leukocyte recruitment and vascular hyperpermeability resulting in a dramatic reduction in tumor blood perfusion. In this work, we used an in vivo model system of cryosurgery of human prostate cancer (LNCaP Pro 5) grown in nude male mice. We show that 4 hour pre-treatment with our nanoparticle system leads to a dramatic reduction in tumor blood perfusion with a simultaneous increase in tumor vascular hyperpermeability. However, we do not see increased NFκB activation in tumor endothelial cells or increased leukocyte recruitment over the same timeframe implicating a different mechanism of preconditioning for nanoparticle-delivered TNF-α compared to native TNF-α. In vivo

leukocyte depletion and NFκB inhibition experiments support these findings by demonstrating that the enhancement of cryosurgical injury is independent of leukocyte recruitment and NFκB activation. We also demonstrate that nanoparticle preconditioning can be used to enhance high temperature thermal therapy in the LNCaP tumor model. Finally, nanoparticle preconditioning was tested in combination with radiofrequency ablation and cryosurgery in a translational model of rabbit kidney tumors. The current work builds on our understanding of the mechanisms of nanoparticle preconditioning for enhancement of thermal therapy which could lead to the identification of novel adjuvants to be used in combination with TNF-α for improved clinical outcomes.

TABLE OF CONTENTS

LIST OF TABLES

LIST OF FIGURES

COPYRIGHT PERMISSION

Permission to use Future Medicine Ltd copyright material

Request from:

- Contact name: Mithun Shenoi
- Publisher/company name: University of Minnesota
- Address: Minneapolis, MN 55455, USA
- Telephone/e-mail: mshenoi@umn.edu

Request details:

- Request to use the following content: Author - Full Article - Nanomedicine, April 2011, Vol. 6, No. 3, Pages 545-563
- In the following publication: PhD Thesis
- In what media (print/electronic/print & electronic): Print & Electronic
- In the following languages: All

We, Future Medicine Ltd, grant permission to reuse the material specified above within the publication specified above.

Notes and conditions:

1. This permission is granted free of charge, for one-time use only.
2. Future Medicine Ltd grant the publisher non-exclusive world rights to publish the content in the publication/website specified above.
3. Future Medicine Ltd retains copyright ownership of the content.
4. Permission is granted on a one-time basis only. Separate permission is required for any further use or edition.
5. The publisher will make due acknowledgement of the original publication wherever they republish the content: citing the author, content title, publication name and Future Medicine Ltd as the original publisher.
6. The publisher will not amend, abridge, or otherwise change the content without authorization from Future Medicine Ltd.
7. Permission does not include any copyrighted material from other sources that may be incorporated within the content.
8. Failure to comply with the conditions above will result in immediate revocation of the permission here granted.

Date: 23/08/2011.....

Future Medicine Ltd, Unitec House, 2 Albert Place, London, N3 1QB, UK
T: +44 (0)20 8371 6080 **F:** +44 (0) 20 8371 6099 **E:** info@futuremedicine.com
www.futuremedicine.com

Order Completed

Thank you very much for your order.

This is a License Agreement between Mithun M Shenoi ("You") and Elsevier ("Elsevier"). The license consists of your order details, the terms and conditions provided by Elsevier, and the payment terms and conditions.

Get the printable license.

License Number	2743161284358
License date	Sep 06, 2011
Licensed content publisher	Elsevier
Licensed content publication	Urology
Licensed content title	Use of Tumor Necrosis Factor–alpha-coated Gold Nanoparticles to Enhance Radiofrequency Ablation in a Translational Model of Renal Tumors
Licensed content author	Renato Nardi Pedro,Thishore Thekke-Adiyat,Raghav Goel,Mithun Shenoi,Joel Slaton,Steve Schmechel,John Bischof,James Kyle Anderson
Licensed content date	August 2010
Licensed content volume number	76
Licensed content issue number	2
Number of pages	5
Type of Use	reuse in a thesis/dissertation
Portion	full article
Format	both print and electronic
Are you the author of this Elsevier article?	Yes
Will you be translating?	No
Order reference number	
Title of your thesis/dissertation	Nanoparticle preconditioning for enhanced thermal therapies in cancer
Expected completion date	Oct 2011
Estimated size (number of pages)	150
Elsevier VAT number	GB 494 6272 12
Permissions price	0.00 USD
VAT/Local Sales Tax	0.0 USD / 0.0 GBP
Total	0.00 USD

ORDER MORE... CLOSE WINDOW

Contribution of Author and Others

This dissertation describes the accumulated doctoral research of the author with contributions and guidance from several collaborators. The author worked closely with the adviser, Dr. John. C. Bischof on the design of experiments, data analysis and preparation of each chapter of this thesis and manuscripts for journal submission with the exception of Appendices A and B. The author worked closely with Dr. Erik. Cressman on Appendices A and B and the associated manuscripts for journal submission. The contribution of the author and others are described below:

Chapter 1: This chapter reviews the nanoparticle preconditioning concept. The present author reviewed the literature, created and edited the manuscript for publication along with Dr. John Bischof. Dr. Robert Griffin, Dr. Neha Shah, Dr. Gregory Vercellotti helped in the conceptualization of the manuscript and assisted in the editing of the manuscript.

- **Shenoi MM**, Shah NB, Griffin RJ, Vercellotti GM, Bischof JC. Nanoparticle preconditioning for enhanced thermal therapies in cancer. Nanomedicine (Lond). 2011 Apr;6(3):545-63.

Chapter 2: This chapter describes the use of nanoparticle preconditioning to enhance thermal therapy in a preclinical tumor model of human prostate cancer. The present author performed all the experiments, created, and edited the manuscript for the following citation. Dr. Stephen Schmechel, Colleen Forster, and Jonathan Henriksen provided support on histopathology.

- Shenoi MM, Schmechel S, Bischof JC. Enhancement of High and Low Temperature Thermal Therapy in Prostate Cancer with Nanoparticle Preconditioning. 2011 (manuscript in preparation for submission to Nanomedicine) Submission invited by editor, Lajos P. Balogh.

Chapter 3: This chapter describes experiments investigating the vascular and immunological mechanisms involved in nanoparticle preconditioning in a preclinical tumor model of human prostate cancer. The present author performed all the experiments, created, and edited the manuscript for the following citation. Dr. Stephen Schmechel, Colleen Forster, and Jonathan Henriksen provided support on histopathology.

- Shenoi MM, Schmechel S, Bischof JC. Vascular and Immunological Mechanisms of Nanoparticle Preconditioning. 2011 (manuscript in preparation for Nano Letters)

Chapter 4: This chapter describes the first use of nanoparticle preconditioning to enhance thermal therapy (radiofrequency ablation) in a translational tumor model. Dr. Renato Pedro, Dr. Kyle Anderson and Dr. John Bischof designed the experiments. Dr. Renato Pedro conducted all the in vivo experiments, data analysis and prepared the manuscript for publication with assistance from Dr. Kishore Thekke-Adiyat. The present author assisted in the data analysis and preparation of the manuscript. Dr. Stephen Schmechel assisted with the histopathological analysis. Leslie Dickinson (VA Medical Center, Minneapolis, MN) assisted with the animal surgeries. Appendix C discusses

experiments that were a direct follow-up to this study.

- Pedro RN, Thekke-Adiyat K, Goel R, **Shenoi M**, Slaton J, Schmechel S, Bischof J, Anderson JK. Use of tumor necrosis factor-alpha-coated gold nanoparticles to enhance radiofrequency ablation in a translational model of renal tumors. Urology. 2010 Aug;76(2):494-8.

Chapter 5: The present author created and edited this chapter of dissertation.

Appendix A: This chapter describes the first set of experiments demonstrating the capability of thermochemical ablation to produce in vivo lesions in a porcine liver model for the treatment of hepatocellular carcinoma. The present author conducted all the experiments, data analysis and assisted in the editing of the manuscript. Dr. Erik Cressman designed the study and prepared the manuscript for publication. Theresa Edelman assisted in designing the study and performed preliminary experiments in support of the main study. Dr. Matthew Geeslin assisted in the data analysis and the editing of the manuscript. Dr. Leah Hennings conducted the histopathological analysis. Yan Zhang performed all the stastistical analysis. Dr. Paul Iaizzo assisted with the in vivo experiments.

- Cressman ENK, Shenoi MM, Edelman TL, Geeslin MG, Hennings LJ, Zhang Y, Iaizzo PA, Bischof JC. In vivo comparison of simultaneous v sequential injection technique for thermochemical ablation in a porcine model. Int J Hyperthermia 2011 (in review).

Appendix B: This chapter describes the follow up study to Appendix A. Experiments were designed to explore the effects of volume and concentration in thermochemical ablation on temperature and volume of coagulated tissues obtained using an in vivo porcine model. The present author conducted all the experiments, data analysis and assisted in the editing of the manuscript. Dr. Erik Cressman designed the study and prepared the manuscript for publication. Dr. Matthew Geeslin assisted in data analysis and preparation of the manuscript. Dr. Leah Hennings conducted the histopathological analysis. Yan Zhang performed all the stastistical analysis. Dr. Paul Iaizzo assisted with the in vivo experiments.

- Cressman ENK, Geeslin MG, Shenoi MM, Hennings LJ, Zhang Y, Iaizzo PA, Bischof JC. Concentration and volume effects in thermochemical ablation in vivo: results in a porcine model. Int J Hyperthermia 2011 (in review).

Appendix C: This chapter describes investigations involving nanoparticle preconditioning to enhance cryoablation in a rabbit VX2 translational tumor model of renal tumors. Dr. Kishore Thekke-Adiyat, Dr. Kyle Anderson and Dr. John Bischof designed the experiments. The present author and Dr. Kishore Thekke-Adiyat conducted all the in vivo experiments, data analysis and prepared the text for the chapter. Dr. Stephen Schmechel assisted with the histopathological analysis. Leslie Dickinson (VA Medical Center, Minneapolis, MN) assisted with the animal surgeries.

Appendix D: This chapter describes preliminary attempts to develop the TRAMP-C2 preclinical tumor model to investigate nanoparticle preconditioning mediated enhancement of cryosurgery. The present author conducted all the experiments, data analysis and created and edited the chapter.

Chapter 1: Nanoparticle Pre-conditioning for Enhanced Thermal Therapies in Cancer

This chapter is a review of the nanoparticle preconditioning concept. A number of opportunities to combine nanoparticles with vascular and immunologically active agents are reviewed. The ability of nanoparticle preconditioning to enhance subsequent thermal therapy in a variety of tumor models is reviewed. Finally, the potential for future clinical imaging to judge the extent of preconditioning and thus the optimal timing and extent of combinatorial thermal therapy is discussed. This chapter was published in the following citation. The article is adapted with permission from Future Medicine Ltd:

- Shenoi MM, Shah NB, Griffin RJ, Vercellotti GM, Bischof JC. Nanoparticle preconditioning for enhanced thermal therapies in cancer. Nanomedicine (Lond). 2011 Apr;6(3):545-63.

1.1. INTRODUCTION

Nanotechnology holds tremendous promise for the treatment of cancer. Recent work has focused on the unique potential of nanotechnology to improve drug delivery, imaging contrast, and heating of tumors over traditional methods in cancer treatment [1, 2]. In some cases, nanoparticles have multifunctional properties or potential for therapy and diagnostics that has led to a new field entitled “theranostics” [3]. There are also increasing opportunities for combinatorial treatment of cancer with nanoparticles [4]. Several classes of nanoparticles, including liposomes, magnetic and metallic, are now in clinical trials for cancer thermal therapy (**Table 1.1**). This report explores the opportunities for nanoparticle based thermal therapy enhancement. Many approaches using nanotechnology are based on the delivery and acute activation of particles to tumors to induce cell death via drug release or thermal cytotoxicity. The work we will review here is distinct in that we refer specifically to a relatively unexplored and exciting opportunity to use nanoparticles to alter the vascular and immunological biology of the tumor (pre-conditioning) to augment the antitumor effects of subsequently applied thermal therapy.

About 1.5 million cases of cancer were projected to be diagnosed in the US in 2009 [5]. The NIH estimates overall costs of cancer in 2008 at $ 228.1 billion with $93.2 billion for direct medical costs (all health expenditures) [5]. Of these, the most prevalent are prostate, breast, colorectal (with metastasis to liver) and lung cancer with 146,000-

Table 1.1. Nanoparticles under Clinical Evaluation that Activate or Enhance Thermal Therapy.

Nanoparticle Class	Examples	Thermal Therapy Application	Company	Indications
LIPOSOMAL	ThermoDox®	Temperature sensitive liposomes release doxorubicin within tumors treated with radiofrequency ablation	Celsion Corporation, New York, NY, USA	Liver and breast cancer
	Myocet™	Liposomally encapsulated doxorubicin administered as neoadjuvant chemotherapy with regional hyperthermia	Sopherion Therapeutics, Princeton, NJ, USA	Metastatic breast cancer
METALLIC	*Aurimune™ (CYT-6091)	Colloidal gold nanoparticle tagged with TNF preconditions solid tumors to thermal therapy	CytImmune Sciences, Rockville, MD, USA	Solid tumors
	AuroLase®	Gold nanoshells passively accumulate within solid tumors and are activated by near infrared laser to heat tumors	Nanospectra Biosciences, Inc., Houston, TX, USA	Head and neck cancer
MAGNETIC	NanoTherm®	Iron oxide particles injected directly into tumors absorb high energy radiation of external magnetic field to heat tumors	MagForce Nanotechnologies AG, Berlin, Germany	Glioblastoma multiforme, prostate cancer, esophageal cancer, pancreatic cancer

* A Phase I clinical trial has been completed with CYT-6091 as a stand-alone solid cancer therapy[6]. Pre-clinical trials have shown efficacy when combined with thermal therapies as discussed in the text.

192,000 new cases each expected in 2009. The primary treatments for these diseases have traditionally been surgical resection, chemotherapy and radiation. However, other approaches are needed for patients who are poor surgical candidates and for those whose primary treatment has failed. This has spurred the growth of alternative approaches including probe based thermal therapies, or thermal "ablative" technologies for cancer over the last 20+ years [7].

Thermal therapies include: cryosurgery (freezing), radiofrequency ablation (RFA), microwave, laser, magnetic fluid hyperthermia and high intensity focused ultrasound (HIFU) [7] (**Table 1.2**). The advantages of thermal therapies include: focal, repeatable, and minimally or non-invasive application with the ability to use image guidance as recently reviewed in a clinically based text on the subject [7]. Unfortunately, while thermal therapies can destroy tissue, a major clinical limitation to their increased use is local recurrence of disease [8, 9]. Researchers in the field have argued that this is generally due to an inadequate understanding and control of the thermal dose, i.e. the necessary temperature and time of exposure needed to ensure killing of all tumor cells [10, 11]. One way to address this is by selectively and controllably reducing the thermal dose required for cytotoxicity between the diseased tissue and normal tissue using combinatorial approaches involving nanoparticles.

Table 1.2. Thermal Therapy Devices in Clinical Use for Solid Tumors. (Note that AuroLase™ and Nano-Cancer® are nanoparticle-based technologies.)

Thermal Therapy	Probe	Company	Indications	Web
CRYOSURGERY	SeedNetTM+	Galil Medical, Yokneam, Israel	Prostate, Kidney Cancers, Uterine Fibroids	www.galil-medical.com
	CryoCare CSTM+	Endocare, Irvine, CA, USA.	Prostate, Kidney, Lung and Liver Cancers	www.endocare.com
	Visica 2TM	Sanarus, Pleasanton, CA, USA.	Breast fibroadenomas	www.sanarus.com
	Various Systems	BryMill, Ellington, CT, USA.	Dermatologic Lesions	www.brymill.com
	Erbokryo CATM	Erbe Medical, Leeds, UK.	General Surgical Use	www.erbe-med.com
RADIOFREQUENCY	Cool-Tip® RF Ablation System	Valleylab, Boulder, CO, USA.	Tumor ablation	www.valleylab.com
	LeVeen needle electrode	Boston Scientific Corp., Natick, MA, USA.	Liver and soft tissue ablation	www.bostonscientific.com
	RITA system	AngioDynamics, Inc., Queensbury, NY, USA.	Surgical oncology, tumor (≤ 7 cm) ablation	www.angiodynamics.com
	HiTT	Berchtold, Tuttlingen, Germany.	Tumor ablation	www.berchtoldusa.com
	Prostiva® RF	Medtronic, Inc., MN, USA	Benign prostatic hyperplasia	www.medtronic.com
HIGH INTENSITY FOCUSED ULTRASOUND	Ablatherm® HIFU	EDAP TMS S.A., Vaulx-en-Velin, France.	Focused surgery, Prostate cancer tumor ablation with imaging	www.edap-tms.com
	ExAblate® 2000	InSightec-TxSonics, Dallas, TX, USA.	Tumor/fibroid ablation with concurrent MR imaging	www.insightec.com
	Sonalleve	Philips, Netherlands	Tumor/fibroid ablation with concurrent MR imaging	www.philips.com
MICROWAVE	Targis®	Urologix, Inc., Minneapolis, MN, USA.	Benign prostatic hyperplasia	www.urologix.com
	Prosatron®	Urologix, Inc., Minneapolis, MN, USA.	Benign prostatic hyperplasia treatment by TUMT®	www.urologix.com

	Microwave AZM-250	Azwell, Inc., Osaka, Japan.	Liver tumor ablation, Deep tissue and surface ablation	
	Prolieve®	Boston Scientific Corp., Natick, MA, USA	Benign prostatic hyperplasia	www.prolieve.com
LASER	INDIGO® Laser System	Indigo Medical, Inc./Johnson & Johnson, Cincinnati, Ohio, USA.	Benign prostatic hyperplasia	www.ethiconendo.com
	GreenLight PV ™ Laser System	AMS, Minnetonka, MN, USA.	Benign prostatic hyperplasia	www.greenlighthps.com
	AuroLase®	Nanospectra Biosciences, Inc., Houston, TX, USA	Refractory head and neck cancer	www.nanospectra.com
MAGNETIC FLUID HYPERTHERMIA	Nano-Cancer®	MagForce Nanotechnologies AG, Berlin, Germany	Glioblastoma multiforme, prostate cancer, esophageal cancer, pancreatic cancer	www.magforce.de

1.2. NANOPARTICLES IN THERMAL THERAPIES

In thermal therapies for cancer, nanoparticles have been investigated mainly for novel methods of in situ delivery of thermal energy to tumors, as recently reviewed [12]. These approaches utilize the unique properties of nanoparticles inherent to their size and composition such as optical and dielectric properties, magnetic susceptibility, thermal or electrical conductivity. The techniques are, in general, minimally invasive and aim to achieve superior localized heating of the entire tumor mass while sparing surrounding normal tissues. For instance, magnetic fluid hyperthermia aims to heat tissue in an alternating electromagnetic field using nanoparticles of specific size and magnetic susceptibility. This was originally pioneered by Gilchrist in the 1950s with iron oxide [13], but remains an approach of interest as evidenced by clinical trials in Europe for treatment of glioblastoma multiforme and prostate tumors (See Magnetic Fluid Hyperthermia, **Table 1.2**) [14, 15]. More recently, photothermal therapy is a growing field where laser light is used to heat nanoparticles (i.e. spherical, rod, and shell particles) with the intention to selectively destroy cells and tissues loaded with nanoparticles. Several novel nanoparticle formulations such as gold nanorods, gold nanocages, carbon nanotubes, etc. are being tested in vitro and in vivo to target tumor cells with the goal of achieving photothermal destruction [16-19]. Von Maltzahn et al. have recently shown that a single injection of polyethylene glycol coated gold nanorods enabled complete photothermal destruction of human xenograft tumors in mice [20]. In a separate study, Zhou et al. have shown the efficacy of copper sulfide nanoparticles in simultaneous in

vivo imaging and photothermal ablation therapy [21]. The real potential of photothermal therapy using nanoparticles is evidenced by the fact that plasmonically active nanoshells are currently in clinical trials in the USA using this technology (See Laser, **Table 1.2**) [22]. In addition, recent work with radiofrequency Joule heating of gold nanoparticles at 13.56 MHz seems promising for heating cancer cells at nanoparticle concentrations far below that necessary for effective magnetic fluid hyperthermia; although exceptionally high powered fields (i.e. 600 W generator) are needed [23]. It is worth noting here that, similar to other nanoparticle-based therapies, the success of these approaches is highly-dependent on tumor-specific localization of the nanoparticle using a targeted approach [24].

A separate multi-modal approach using nanoparticles in thermal therapies involves delivery of chemotherapeutics to enhance direct cell injury mechanisms. Traditional combinatorial approaches involving chemotherapy or radiation therapy have been utilized in the past in conjunction with hyperthermia [25, 26]. Mild hyperthermia impacts tumor physiology by increasing tumor perfusion and vascular permeability [27]. These effects along with perforation of tumor blood vessel walls, microconvection in the tumor interstitium, and perforation of the cancer cell membrane induced by mild hyperthermia are all conducive to improved drug delivery to tumor stromal and parenchymal compartments [28]. Preclinical work on this approach has shown considerable promise in synergistic destruction of tumor cells, however, the data from preliminary clinical trials while mostly positive, have varied in demonstrating synergy

[29-33]. With advances in nanotechnology research, a natural extension of this approach is to package chemotherapeutics in nanoparticle delivery systems for use in combination with thermal therapies. To date the most successful of these strategies is based on liposomal technologies. New clinical trials that involve liposomes with thermal approaches are emerging rapidly. Perhaps the most exciting extension of this concept is the use of a thermally-sensitive liposome that encapsulates anti-cancer agents and is released locally and selectively where the heat is applied. Ponce et al. report on the conception, development and preclinical studies demonstrating increased efficacy using these nanoparticles (liposomes) loaded with doxorubicin in the setting of hyperthermia for cancer therapy [34]. Goldberg et al. report the first preclinical and clinical use of these nanoparticles in conjunction with RFA [35, 36]. In their pilot clinical study on patients with focal hepatic tumors, they show that a single intravenous dose of liposomal doxorubicin (Doxil) administered 24 hours before RFA of the tumors resulted in increased tissue damage at the site of thermal injury compared to RFA alone [35]. These research efforts have resulted in the commercialization of the nanoparticle, ThermoDox^{TM}, and initiation of several clinical trials of combinatorial therapy of ThermoDox^{TM} with hyperthermia or RFA [201]. Emerging work in this area includes thermally-sensitive nanoparticles that release genes (i.e. gene therapy) during hyperthermia [37], or freeze sensitive nanoparticles that release drug locally during cryosurgery [38]. These advancements show the potential clinical utility of nanoparticles to enhance direct destruction of tumor cells with thermal therapy. A new but related concept using nanoparticles functionalized with bioactive ligands to “pre-condition”

vascular and immunological mechanisms of tumor destruction *prior to* thermal therapies (**Figure 1.1**) has also shown significant potential to enhance outcomes as reviewed below.

1.3. Nanoparticle Pre-conditioning of Tumors for Thermal Therapy

We define "pre-conditioning" as the use of a bioactive agent (e.g. TNF-α, arsenic trioxide, interleukins, etc.) to modify the vascular and/or immunological components of the tumor microenvironment so as to make the tumor tissue more susceptible to a secondary treatment such as thermal therapy. Pre-conditioning of the tumor with bio-conjugated nanoparticles requires an understanding of the in vivo mechanisms of thermal injury and the wound healing response that follows. The tumor microenvironment is a complex milieu resultant of the competing interactions between several pro- and anti-tumorigenic components (cytokines, endothelial cells, inflammatory cells, fibroblasts, extracellular matrix elements) [39]. The goal of pre-conditioning is to shift the balance of these interactions in the anti-tumorigenic direction so as to enhance the outcome of thermal therapies (i.e. increased and controlled tumor cell kill, decreased local recurrence). Several components of the tumor microenvironment are amenable to pre-conditioning by drugs already in preclinical or clinical trials (**Table 1.3**).

1.3.1. Selection of Pre-conditioning Agent and Nanoparticle Design

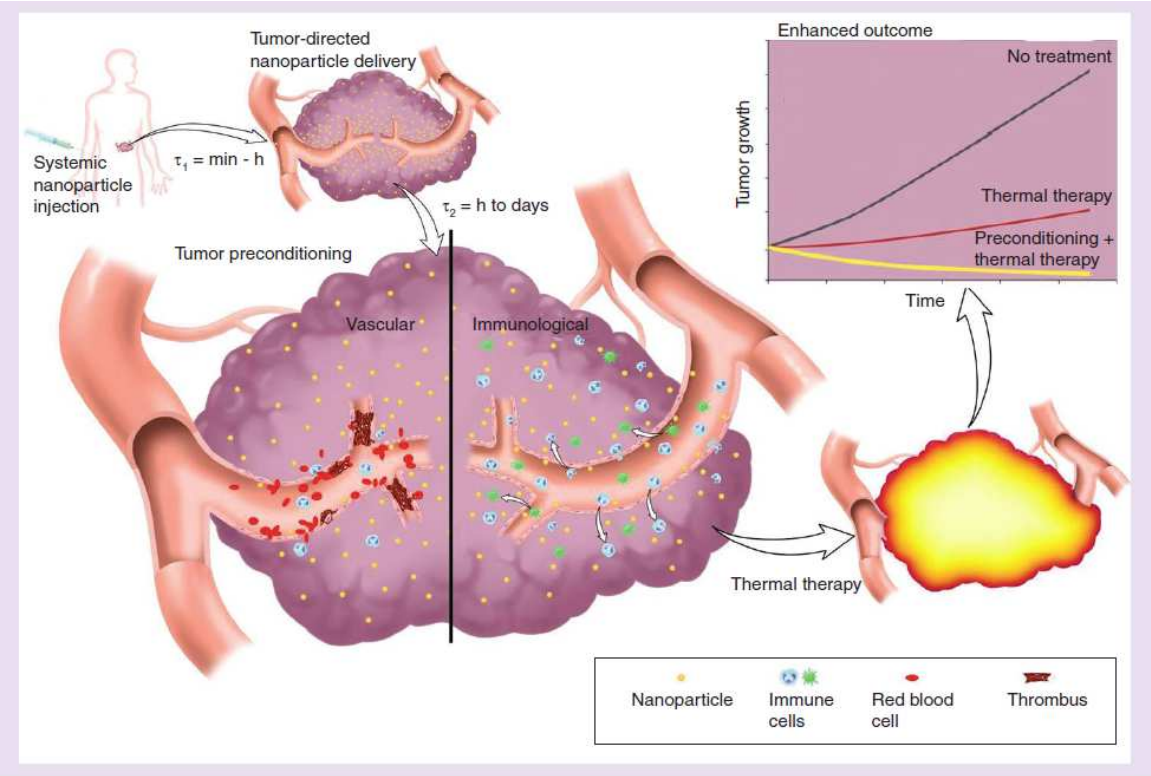

Figure 1.1. Nanoparticle preconditioning of tumor. Preconditioning the tumor using a bioconjugated nanoparticle prior to thermal therapy for achieving enhanced tumor destruction. Systemic injection of the nanoparticle leads to its accumulation in the tumor within a short timeframe (minutes to hours). Localization of the nanoparticle within the tumor initiates vascular and immunological preconditioning events (detailed in text) that reach peak response in a longer timeframe (hours to days). Thermal therapy (heat or cold) is then administered at an optimal time based on nanoparticle preconditioning to achieve superior tumor destruction over thermal therapy alone.

Table 1.3. Potential Pre-conditioning Agents for Thermal Therapies. (This is not intended as a comprehensive list, but only to highlight the potential of tumor microenvironment targets for pre-conditioning.)

Adjuvant Class	Sub-type	Preconditioning Mechanism	Potential Agents	Reference
VASCULAR	Vascular destructive agents (VDAs)	Tumor vascular injury by direct endothelial cytotoxicity, increase junctional retraction of endothelial cells, recruitment of inflammatory infiltrate, etc.	TNF-α	
			CYT-6091*	[40]
			PEG-TNF*	[41]
			CA4-P/CA1-P	[42, 43]
			DMXAA	[44]
			ZD6126	[45]
			AVE8062	[45]
			Arsenic trioxide	[46]
	Vasoactive agents	Increase in tumor vascular permeability	Bradykinin	[47]
			Histamine	
			Serotonin	
			Prostaglandins	
			Leukotrienes	
			Complement (C3a, C4a, C5a)	
			Nitroglycerin	
	Pro-coagulant/ Vasoconstriction	Reduction in tumor perfusion by thrombus formation in tumor vessels	Thromboxane	
			Fibrinogen	[48]
			tPA inhibitor	
			Phenylephrine	
			Pentobarbital	[49]
			Metaraminol	[49]
	TGF-β inhibition	Increase in tumor vascular permeability	TβR-I inhibitor (LY364947)	[50]
IMMUNOLOGICAL	Cytokine	Modify tumor immune environment to activate or recruit antitumor immune	TNF-α	[51]
			IFN- α	[52]

	cell response	PEG-IFN	[53]
		IL-2/Histamine	[54]
		PEG-IL-2	[55]
		IL-12	[56]
Treg modulation	Inhibition of suppressive effects of regulatory T cells on antitumor helper and effector T cell responses	Anti-CTLA4*	[57]
TGF-β inhibition	Inhibition of immunosuppressive effects of TGF- β	Small molecule and antibody inhibitors of TGFβRI and TGFβRII in clinical and preclinical trials	[58]
TLR activation	Immunostimulatory molecules that activate specific TLR receptors on immune cells esp. antigen presenting cells	TLR 2,3,4,5,7,9 agonists in preclinical and clinical trials	[59]
		Imiquimod	[60]
		CpG-ODN	[61]
		LPS	[51]
		BCG-CWS	[62]
		OK-432	[63]
		siRNA-PEI*	[64]
		Anti-CD40-PLA*	[65]

* Agents administered in nanoparticle formulations.

Although a large number and wide variety of potential pre-conditioning agents are available (**Table 1.3**), the biomolecule of interest in our recent studies, TNF-α, is an ideal pre-conditioning agent due to its well-established mechanism of action against the tumor vasculature, potential for sensitizing tumor cells to thermal injury, potential for eliciting an antitumor immune response, and documented clinical success in solid tumor therapy in native and nanoparticle form (although currently limited in scope). In vitro studies conducted by our group have shown that pre-treatment with native TNF-α sensitizes various tumor cell lines to thermal (heat and cold) injury [66-68]; however, the effect is more pronounced in microvascular endothelial cells. This suggests that even though direct cytotoxicity of tumor cells may be enhanced following thermal therapy the primary mechanism of pre-conditioning plays out within the tumor vasculature. CYT-6091 (CytImmune Sciences, Inc., Rockville, USA), a polyethylene glycol (PEG) coated gold nanoparticle tagged with tumor necrosis factor alpha (TNF-α), has been explored by our group to deliver TNF-α to the tumor vasculature and pre-condition the tumor microenvironment for enhancement of thermal (heat and cold) therapies. CYT-6091 has already completed a Phase I clinical trial as a standalone anticancer therapeutic [6, 69]. The significant findings of the trial include lack of dose limiting toxicities or drug related serious adverse events, even at a 3-fold higher dose of 600 μg TNF-α/m^2 than the maximum tolerated dose of native TNF-α [6]. In addition, an absence of a systemic hypotensive response was observed, a major limiting factor that has restricted the use of native TNF-α in the clinical setting to isolated limb perfusion treatment of high-grade sarcomas and melanomas [70]. The base rationale behind attaching the cytokine to a

nanoparticle (CYT-6091) is to reduce systemic toxicity and improve the localization of TNF-α to the tumor tissue. In several preclinical tumor models, we have shown that a *single systemic injection* of CYT-6091 4 hours prior to thermal therapy results in enhanced therapeutic outcome similar to that of previous preclinical work [71], yet with little to no overt toxicity. The toxicity profile of CYT-6091 may be further improved by the addition of a tumor targeting moiety to the gold nanoparticle such as antibodies, peptides or aptamers. This approach, especially using antibodies to target tumor cell receptors, has been widely tested in various cancers and would reduce the exposure of healthy tissues to TNF-α thereby improving its toxicity profile [24]. This nanoparticle design should allow entry in the tumor via the enhanced permeability and retention (EPR) effect and binding onto the tumor cells. A potential caveat of using nanoparticles to pre-condition tumors for enhanced thermal therapies is the ability of the nanoparticles to directly modify the thermal properties of tumor tissue. This is an area of intense research in the nanotechnology community but only a limited number of studies have been conducted to investigate this behaviour of nanoparticles in biological tissues. In one study, Liu and colleagues conducted experiments that suggested an increase in thermal conductivity of ex vivo tissues when injected locally with a large amount of iron oxide nanoparticles (estimated at 5% local particle volume fraction) [72]. In the case of gold nanoparticles, a recent study by Shalkevich et al showed no significant increase in the thermal conductivity of gold nanoparticles suspended in water even at particle volume fraction of 0.11% [73]. These results indicate that incredibly high volume fractions of nanoparticles are required within tumors to affect its thermal properties. Our

biodistribution results for CYT-6091 yield tumor particle volume fractions on the order of 10^{-5}% when injected intravenously [74]. Similar particle volume fractions on the order of 10^{-8}-10^{-5}% were obtained in another study using 20-100 nm diameter neutral PEG coated gold nanoparticles [75]. Thus, we can safely assume that changes in the thermal properties of tumors by nanoparticles do not contribute to the thermal sensitization obtained by the pre-conditioning mechanisms described below.

1.3.2. Pharmacokinetics and Biodistribution

The use of nanoparticles for pre-conditioning the tumor is dependent on delivery of the molecular payload to the tumor site. A limited number of studies have been conducted to determine the pharmacokinetics and biodistribution of gold nanoparticles in vivo. These studies usually look at the effect of size, shape, charge, coating and targeting moiety on the biodistribution of nanoparticles. De Jong et al. studied the effect of size on the biodistribution of gold nanoparticles in naïve rats at 24 hours after intravenous injection [76]. Their results showed that the highest accumulation of nanoparticles occurred in the liver with the 10 nm nanoparticles showing widespread accumulation in various organs. Another study of gold based core-shell particles showed that the maximum tumor accumulation occurs at 24 hours whereas the overall highest accumulation occurs in the spleen (up to 24 days) [77]. More recently, Perrault et al. conducted an elaborate study of the effect of particle size (20-100 nm) and surface chemistry (amount of PEG) on the pharmacokinetics and biodistribution of PEG coated gold nanoparticles [75]. In that study, athymic nude mice implanted with human breast cancer xenograft tumors were

used to systematically examine how particle design can be optimized towards efficient tumor targeting. The authors of the study note that two desirable properties of the nanoparticles for tumor targeting - small hydrodynamic diameter and long half-lives - appear to converge when particles below 50 nm are protected with a PEG layer of moderate molecular weight (MW 5 kDa). To support this claim, they present results on the permeation of different sized PEG coated gold nanoparticles through the tumor interstitial space with the smallest diameter (20 nm) particles migrating furthest away from the tumor vasculature (**Figure 1.2B**). These and a host of other studies, mainly using liposomal nanoparticles, have led to three major insights into in vivo biodistribution of nano-sized agents: 1) smaller particles (20-200nm) are readily taken up in the tumor due to leaky vasculature (EPR effect); 2) surface modification with hydrophilic polymers (PEG) can reduce uptake by reticuloendothelial (RES) organs (such as liver and spleen); 3) attachment of the targeting moieties on the particle surface results in selective (but not exclusive) uptake by the target organs or tumors [78]. These insights were incorporated in the development of CYT-6091 (a 30 nm diameter colloidal gold nanoparticle coated with PEG and tagged with TNF-α) and resulted in promising biodistribution results obtained in preclinical studies [79].

In our recent studies, a certain degree of tumor targeting of CYT-6091 was verified through pharmacokinetic and biodistribution studies (**Figure 1.2**) [74]. A single intravenous injection of CYT-6091 resulted in preferential accumulation of bioactive TNF-α in human prostate xenograft tumors (LNCaP Pro 5) grown in the hindlimb of

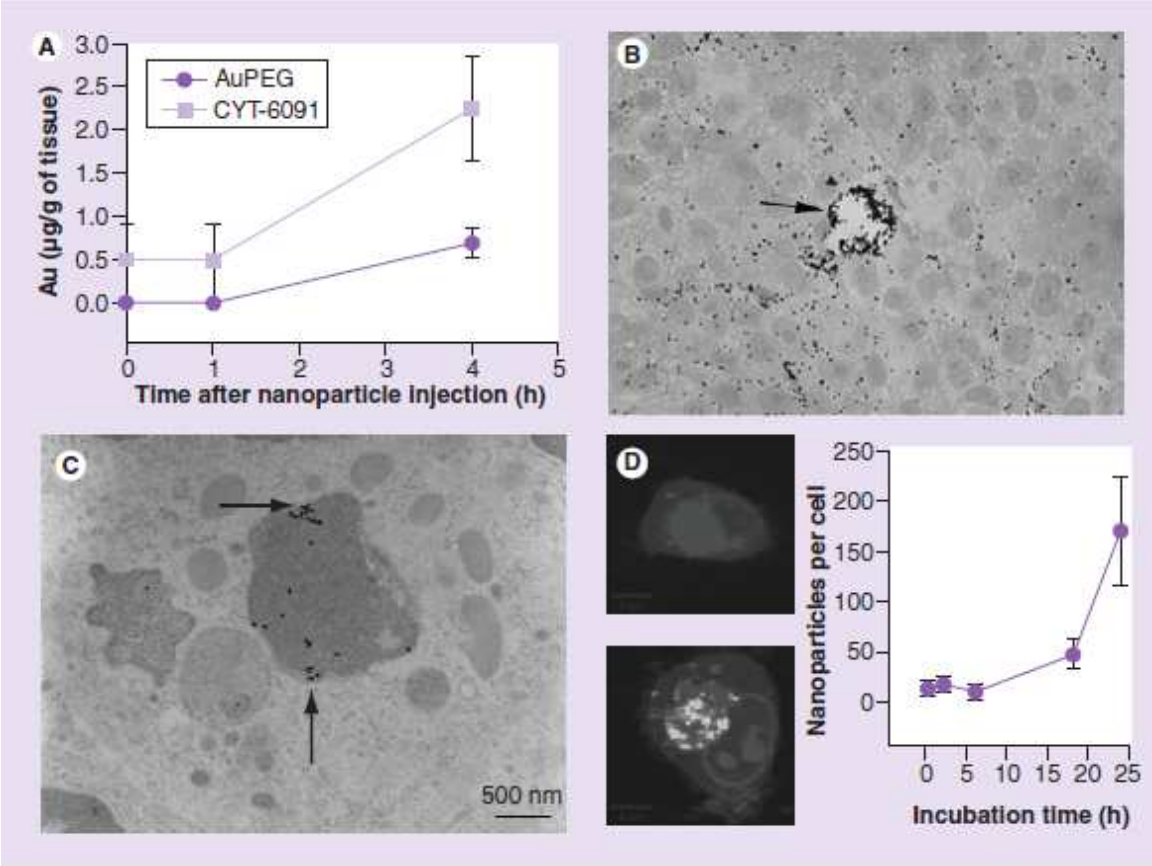

Figure 1.2. Nanoparticle Uptake in Cancer during Pre-conditioning. (a) Control NP and CYT-6091 accumulation in prostate tumors based on atomic emission spectroscopy (AES) measurements of gold. Presence of TNF-α on the nanoparticle increases its uptake in the tumor [74]. Results are expressed as mean ± SD. (b) 8 hours post injection, 20 nm control nanoparticles migrate far into the interstitial space of the tumor from blood vessel (arrow) Adapted with permission from [75] Copyright 2009 American Chemical Society. (c) Electron micrograph of prostate tumor 3 days post injection shows CYT-6091 NPs scattered around in tumor individually or in membrane bound organelles (arrows). (d) In vitro uptake analysis of LNCaP (prostate cancer) cells with confocal Raman microscopy shows no internalization of CYT-6091 at 2 hours (top) incubation whereas perinuclear localization (bottom, particles in green) after 24 hours of incubation. Quantitative analysis of cellular uptake via AES shows increasing cellular uptake over time (right).

nude mice within 4 hours as compared to the liver and spleen, the major organs of the reticuloendothelial system that play a vital role in nanoparticle clearance. We also detected that the presence of TNF-α influenced the biodistribution of CYT-6091 by extending the blood circulation time of the gold nanoparticle with reduced uptake in the liver 4 hours after injection [74]. Importantly, loading of the nanoparticle in tumor tissue was also significantly increased by the presence of TNF-α on the surface of the injected particles (**Figure 1.2A, 1.2C)**. These findings are in line with previously published data [79]. We have also conducted in vitro studies using confocal Raman microscopy to non-invasively image the uptake of CYT-6091 by LNCaP tumor cells revealing unique spectroscopic features corresponding to the intracellular localization of gold nanoparticles over 2 to 24 hours at the membrane, cytoplasm or nucleus (**Figure 1.2D**) [80]. These results established that targeted delivery of TNF-α to tumors by CYT-6091 was possible with limited adverse side effects while also setting the timeframe over which pre-conditioning of the tumor may occur prior to thermal therapy. We have focused much of our recent attention on this particle to develop improved combined treatment strategies since it encompasses features that we hypothesized would be ideal for sensitization of tumors to subsequent thermal exposures and is progressing in clinical testing (Phase II). There is therefore significant potential to translate the pre-conditioning approach to the clinic in the relatively near future.

1.3.3. Vascular Pre-conditioning by TNF-α or other agents

Systemic delivery of TNF-α through the bloodstream likely leads to its interaction with TNF receptor 1 (TNFR-1) on the luminal side of tumor-associated endothelial cells, setting off a cascade of intracellular molecular interactions that are grouped into two major pathways: NFκB-activated pro-inflammatory pathway and caspase-mediated apoptotic pathway. In vivo inhibition studies have revealed that the NFκB-activated pro-inflammatory pathway in endothelial cells is critical for pre-conditioning the tumor with native TNF-α to enhance thermal therapy [66]. These pro-inflammatory changes result from de novo gene transcription and translation of proteins mediated by NFκB and require around 2 to 6 hours to reach peak response [81]; thus, setting the 4 hour timeframe to obtain effective pre-conditioning. The pro-inflammatory changes induced by TNF-α include vascular hyperpermeability, increased expression of cell adhesion molecules and chemokines (ICAM-1, VCAM-1, E-selectin, P-selectin, CXCL8), recruitment of leukocytes (neutrophils, monocytes), leukocyte-mediated endothelial cell injury, increased synthesis of tissue factor, increased procoagulant activity and decreased anticoagulant activity (**Figure 1.3A-B, 1.4**) [70, 81, 82]. Consistent with these results, Farma et al. measured the rate of interstitial accumulation of an intravenously administered fluorescent marker in TNF-α sensitive and resistant tumors and showed that CYT-6091 induced a selective and rapid alteration of permeability of the tumor vasculature that was tissue factor dependent [83].

Such vascular changes may also be elicited by other potential pre-conditioning agents (**Table 1.3**). For example, vascular destructive agents (VDAs) target endothelial

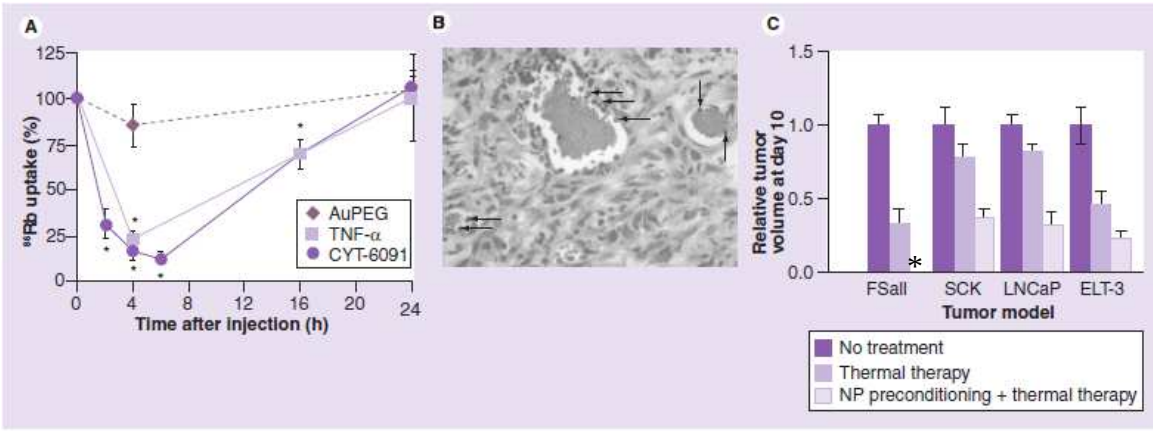

Figure 1.3. Thermal Therapy Enhancement by Pre-conditioning with TNF-α Tagged Gold Nanoparticles. (a) Blood perfusion changes within SCK mammary carcinoma tumors assessed by uptake of radioactive rubidium in tumors after CYT-6091, TNF-α and Control NP systemic injection [67]. CYT-6091 produces the maximum decrease in tumor blood perfusion 4-6 hours after systemic injection. Results are expressed as mean ± SEM and normalized to untreated controls. * Indicates statistically significant difference from untreated control. (b) H&E stain of a TRAMP-C2 tumor grown in a dorsal skin fold chamber, 4 hours after topical administration of native TNF-α, showing thrombus formation and neutrophil margination in blood vessels. (c) Tumor growth delay data with and without CYT-6091 pre-conditioning in pre-clinical tumor models: FSaII fibrosarcoma & SCK mammary carcinoma with heat [67, 68] and LNCaP prostate carcinoma & ELT-3 uterine leiomyoma with cryosurgery [84, 85]. Results are expressed as mean ± SEM and normalized to control tumor volumes at Day 10 after therapy. In some cases, Day 10 volumes were linearly extrapolated from adjacent data points. * Indicates that Day 10 data is not available as tumors completely regressed by Day 4 [67].

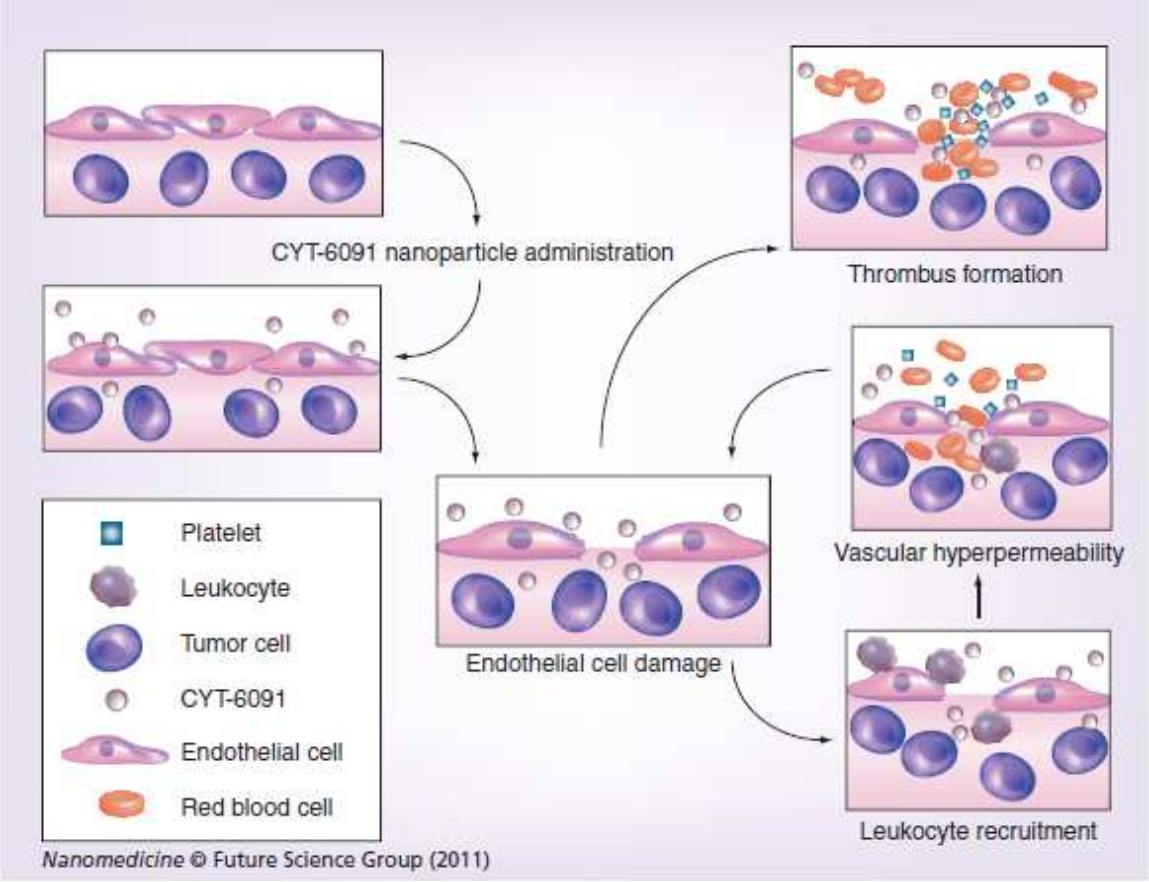

Figure 1.4. Proposed Mechanism of Pre-conditioning with TNF-α Tagged Gold Nanoparticles. Schematic showing interaction of CYT-6091 with tumor endothelium and cells leading to pro-inflammatory pre-conditioning events i.e. vascular hyperpermeability, recruitment of leukocytes (neutrophils, monocytes, lymphocytes), leukocyte-mediated endothelial cell injury, increased synthesis of tissue factor, increased procoagulant activity and decreased anticoagulant activity.

cells and pericytes of established tumor vasculature to cause complete tumor vascular shutdown. We have demonstrated that the FDA-approved anti-leukemic agent Arsenic Trioxide has such effects on the microvasculature of solid tumors [46, 86-88]. This likely occurs due to severe oxidative stress and cell death in the vasculature upon exposure to arsenic which leads to vascular stasis and sensitivity to thermal therapy. One subset of VDAs, tubulin-binding agents (e.g. CA4P), disrupt endothelial cytoskeleton or interfere with cell-to-cell contact leading to increased vascular permeability, exposure of basement membrane and induction of the coagulation cascade resulting in thrombosis. Another subset of VDAs, flavonoids (e.g. DMXAA), have a more complex mechanism of action involving DNA damage to endothelial cells inducing apoptosis and upregulation of NFκB pathways similar to the purported mechanism of action of CYT-6091 leading to tumor vascular shutdown [45]. These VDAs are already in phase I and II clinical trials for cancer therapy and represent ideal first-line candidates for tagging on to nanoparticles for pre-conditioning tumors prior to thermal therapies [45, 89]. Other well-studied molecules/drugs such as vasoactive agents (bradykinin, prostaglandins, leukotrienes, etc.) that induce vascular permeability or pro-coagulant molecules (thromboxane, tPA, etc.) that induce vasoconstriction and thrombosis could also be tested as pre-conditioning agents when tagged on to nanoparticles for selective and non-toxic delivery to tumor vasculature (See **Table 1.3**). Many of these agents do not exhibit their activity on the tumor vasculature alone. Instead, immunological reactions to the cell death occurring in the tumor (such as leukocyte recruitment due to the damage response by the vasculature) often appears to be an intrinsic component of their mechanisms of action. Systemically

administered native TNF-α or CYT-6091 may activate circulating blood cells such as neutrophils which would increase their recruitment to the tumor vasculature [90]. These pro-inflammatory changes in the host and the tumor act synergistically with vascular (coagulation and thrombosis) responses after thermal therapy-induced tissue damage to contribute to the enhanced tumor destruction observed after these combined treatments.

1.3.4. Immunological Pre-conditioning

Ongoing research in our group has implicated that neutrophil-endothelial cell interaction following combined nanoparticle and thermal therapy leads to endothelial cell apoptosis that further enhances the ultimate antitumor effects of vascular pre-conditioning [91]. However, it is unclear if the role of neutrophils in tumor destruction ends here. There is evidence to suggest that neutrophils play a larger role in causing direct tumor cell death as well as in modulating the downstream antitumor adaptive immune response [92]. The dual nature of immune cells in relation to the tumor microenvironment is well-recognized and studied in macrophages and T lymphocytes [93, 94]. Thus, there exists an opportunity for immunological pre-conditioning of the tumor which could involve polarization of tumor-associated macrophages to enhance tumor kill or by promotion of cytotoxic T lymphocyte mediated tumor destruction. This type of pre-conditioning could act in concert with vascular pre-conditioning mechanisms as may be the case with CYT-6091. TNF-α is known to promote antitumor immune responses and current research in our group is geared towards understanding the role of TNF-α and CYT-6091 in modulating the adaptive immune response and long term wound involution following

thermal therapy [95]. Several other immune modulating biomolecules (**Table 1.3**) have shown potential to act as pre-conditioning agents as well. For example, a variety of cytokines (e.g. IL-2, IL-12, IFN-α in addition to TNF-α) are in clinical trials as antitumor therapeutics especially in combination with chemotherapy (**Table 1.3**).

Anti-CTLA4 antibodies are another particularly exciting prospect as pre-conditioning agents because they have been extensively researched and are also already in clinical trials though not in combination with thermal therapies. These antibodies are known to successfully inhibit the immunosuppressive environment of tumors to elicit an effective antitumor immune response however their clinical use is limited by autoimmunity side effects due to the high systemic dose required [96]. To overcome this limitation, Lei et al. have tested a nanoparticle system loaded with anti-CTLA4 antibodies in a preclinical tumor model showing increased antitumor activity with decreased toxicity compared to native antibodies [57]. Other immune modulating agents such as TGF-β inhibitors and toll-like receptor (TLR) agonists are also gaining immense clinical interest as antitumor therapeutics (**Table 1.3**). By taking into account the mechanisms of thermal injury (heat and cold) in their selection, a wide variety of vascular and immunological pre-conditioning agents with near term potential would be expected to have great potential to be combined with nanotechnology to enhance thermal therapies in cancer and avoid the typical side effects encountered with each type of agent when used systemically on their own.

1.3.5. Mechanisms of Thermal Injury

The vast amount of literature on thermal therapies differentiates between three forms of thermal (heat and cold) injury in tumor tissues: direct cell injury, vascular injury and immunological injury [97-99]. In cold-based therapies (i.e. cryosurgery), the tissue is frozen usually to a cryogenic (i.e. < -40 °C) temperature. In this process, damage to cells typically occurs by a phase change event of intracellular or extracellular water (liquid to solid) causing either extreme dehydration or intracellular ice formation [97]. This can in turn lead to biochemical events such as protein denaturation or peroxidation of lipids that terminate in necrosis or apoptosis of the cells [97, 99]. In a distinct but related manner, heating of cells yields phase change within the macromolecules (protein, DNA, lipids) of cells themselves. However, most of the research evidence points to protein denaturation as the rate limiting step in direct cell injury due to heating [100]. If these events are sub-lethal there is usually heat shock response that can interact with the proteins and lipids and keep the cell alive, however, once the injury is too severe cell death occurs again by necrotic or apoptotic mechanisms [100]. In the case of both heat and cold direct cell injury, the end result is membrane destabilization and hyperpermeability [97, 98]. Pre-conditioning agents that decrease the threshold for hyperpermeability of cell membranes could thus improve nanoparticle uptake and facilitate delivery of cytotoxic drugs via nanoparticles into tumor cells. Microenvironmental factors such as tumor blood flow, pH and oxygenation are known to affect the thermosensitivity of tumor cells and thus present an opportunity for modulation by pre-conditioning agents to increase the thermosensitivity of tumor cells [98]. For example, blood flow acts as a heat sink and

source in hyperthermic and cryotherapy respectively hindering the attainment of lethal end temperatures within the tumor tissue during thermal therapy. Direct cell injury is an important mechanism of thermal injury; however, in vivo it is supplemented by vascular injury mechanisms that extend the thermal damage. During cold-based therapies, microvascular shutdown usually occurs at –20 °C after moderate cooling and thawing rates in a variety of tissues, although this can occur at slightly higher temperatures in tumors [97]. Similarly, hyperthermia even at mild supraphysiological temperatures can cause microvascular dysfunction and shutdown in tumor tissues [27]. One possible difference between heat and cold injury is the amount of tumor tissue that undergoes reperfusion after the initial thermal insult. Blood flow, which will cease during the freezing event, is usually re-established after thaw. However, after thermal therapy only the volume of tumor tissue exposed to lower hyperthermic temperatures ($<50^{o}$C) can undergo reperfusion due to the central part of the thermal lesion exposed to higher temperatures being coagulated or thermally fixed [101]. This mechanistic difference may affect ischemia-reperfusion injury differentially in thermal injury by heat versus cold based therapies. It is now well-established that vascular injury progresses beyond the initial thermal insult (both heat and cold) and typically peaks at day 3 following thermal therapy [97, 98]. Tumor endothelial cell damage is the hallmark of vascular injury leading to increased vascular leakage, vessel wall adhesiveness and coagulation and thrombotic events within the tumor vasculature [98]. This progressive cessation of blood flow leads to ischemia within tumor tissue and necrosis of tumor cells. This mechanism of thermal injury is exploited in the use of CYT-6091 as a pre-conditioning agent and

serves as the rationale for exploring other vascular pre-conditioning agents (**Table 1.3**) for use in combination with thermal therapies. The progression of vascular injury in the thermal lesion is also accompanied by recruitment of inflammatory cells (neutrophils) that could be responsible for the progressive nature of vascular damage or may be directly exerting cytotoxic effects on remnant viable tumor cells within the thermal lesion [92, 102, 103].

The final, relatively poorly understood, mechanism of immunological stimulation/injury in thermal therapies is based on the premise that thermal injury activates a host-mediated antitumor immune response. Sabel provides a thorough review on the conflicting set of preclinical studies examining the immune response to cryosurgery [104]. The immune response following hyperthermia is also actively being studied [105]. However, there is still a lack of clear understanding of the exact mechanisms of the immune response following thermal therapies partly due to distinct differences observed when time/temperature history and local versus whole body heating are considered. There is evidence to suggest that necrotic cells releasing ‘danger signals’ are more efficient at inducing an immune response than apoptotic cells [106]. Thus we may hypothesize that thermal therapies resulting in an increased fraction of necrotic versus apoptotic cells would be more amenable to immunological injury. It is also conceivable that certain thermal therapies may induce a greater release of ‘danger signals’ and thus a stronger antitumor immune response from the host which could be yet another way to differentiate between heat and cold based therapies. For example, the

coagulative and thermally fixed zone formed in high temperature therapies could prevent the release and exposure of danger signals to the host immune cells indicating possibly leading to a variable immune response compared to cold based therapies. Various studies have demonstrated synergistic antitumor effects when combining immunotherapy and thermal therapies (both heat and cold) (**Table 1.3**). In general, there is much still to be learned about the role of inhibitory elements of the immune system and the induction of effective antitumor immunity by thermal or other methods. It seems imperative that the immune portion of the antitumor effect of vascular damaging nanoparticle and thermal therapy delivery strategies must be accounted for by using immunocompetent models as much as possible or in addition to xenograft models.

We have demonstrated numerous positive tumor responses in our models with nanoparticle pre-conditioning for improved hyperthermia and cryosurgery in both immunocompetent and immunocompromised models (**Table 1.4)**.

1.3.6. Nanoparticle Enhanced Hyperthermia

The first demonstration of nanoparticle pre-conditioning enhancement of tumor thermal therapy was conducted by Visaria et al. [68]. In this work, SCK hindlimb tumors grown in A/J mice and FSaII hindlimb tumors grown in C3H mice were injected with a single intravenous dose (250 μg TNF-α/kg) of CYT-6091 4 hours prior to heating for 60 min at 42.5^{o}C using a water bath. These preclinical studies in mice showed significant increases in heat-induced tumor growth delay with CYT-6091 pre-conditioning prior to

Table 1.4. Preclinical Evaluation of CYT-6091 as a Pre-conditioning Agent for Thermal Therapy.

Tumor Cell Line	CYT-6091 Dose*	Animal Model	Thermal Therapy	Significant Outcomes**	Reference
LNCaP Pro 5 prostate carcinoma	200 μg/kg	Mouse hindlimb	Cryoprobe: -120°C%	25% complete remission, significant TGD#	[84]
	200 μg/kg	Mouse hindlimb	Cryoprobe: -40°C%	Significant TGD	[107]
	200 μg/kg	Mouse DSFC	Cryoprobe -120°C%	Iceball edge = tumor necrosis edge	[84]
ELT-3 uterine fibroma	80-200 μg/kg	Mouse hindlimb	Cryoprobe -120°C%	Significant TGD	[85]
SCK mammary carcinoma	125-250 μg/kg	Mouse hindlimb	Hot Water Bath: 42.5°C, 60 min	Significant TGD, enhanced tumor perfusion defect	[68]
FSaII fibrosarcoma	50-250 μg/kg	Mouse hindlimb	Hot Water Bath: 42.5-43.5°C, 60 min	Significant TGD, enhanced tumor perfusion defect	[67]
VX2 carcinoma	200 μg/kg	Rabbit kidney	Radiofrequency ablation	Enhanced tumor cell death in ablation zone	[108]
	200 μg/kg	Rabbit kidney	Cryoprobe: -100 °C%	Decreased metastases	[109]

* CYT-6091 dose was administered 4 hours prior to thermal therapy.
** Compared to thermal therapy alone.
# Tumor growth delay
% Lowest temperature achieved by cryoprobe.

hyperthermic treatment (**Figure 1.3C**) [67, 68]. Up to 80% reduction in tumor blood flow as assessed by uptake of the radioactive tracer rubidium, was also measured at 4 hours after CYT-6091 injection that is consistent with known localized mechanisms of TNF-α vascular effects and damage in tumors (**Figure 1.3A-B**). This accentuation of hyperthermic injury also shows clear dose dependency. Our group has also conducted preliminary translational studies using VX2 tumors grown in rabbit kidneys. Administering CYT-6091 prior to RFA yielded a significantly larger zone of central necrosis (i.e. 23% increase in ablation volume) than RFA treatment alone on histological evaluation 3 days after the procedure. Control tumors that were not treated with RFA also showed a significant reduction in tumor volume after CYT-6091 treatment alone although not as much as RFA plus CYT-6091 group [108, 109]. This reduction in tumor volume after CYT-6091 treatment alone within 3 days usually occurs after multiple injections over time and may be attributed to the unique nature of the VX2 tumor physiology (i.e. more susceptible) [6]. Typically, our in vivo studies in mice yield significantly less tumor growth delay when CYT-6091 is administered without thermal therapy [67, 68]. Clinically, a multiple dosing schedule was used in a Phase I trial in which CYT-6091 was administered as a standalone cancer therapeutic [6, 69].

1.3.7. Nanoparticle Enhanced Cryosurgery

We have also extensively investigated CYT-6091 particles for pre-conditioning tumors to enhance cryosurgical injury in preclinical models. Cryosurgery was conducted using a Joule-Thomson based argon cryoprobe with the tip temperature maintained at -100^{o}C.

Systemic injection of 200 μg TNF-α/kg of CYT-6091 4 hours prior to cryosurgery of human prostate cancer xenograft (LNCaP Pro 5) and uterine fibroid (ELT-3) tumors grown in hindlimb of nude mice resulted in significant tumor growth delay and in some cases complete remission compared to mice injected with an equivalent dose of native TNF-α or the control nanoparticle without TNF-α (**Figure 1.3C, 1.5**) [84, 85]. Furthermore, mice administered with CYT-6091 displayed no overt toxicity whereas nearly 25% of mice injected with native TNF-α prior to cryosurgery died within several hours after the therapy. Since tumor kill by cryosurgery is highly dependent on the temperature and rate of temperature change experienced by the tumor, in subsequent studies we used the dorsal skin fold chamber (DSFC) tumor model coupled with real time infrared imaging and thermocouple measurements to obtain the spatial temperature profile of the tumor tissue during and immediately after cryosurgery. Similar to hyperthermic injury, we also discovered a dose-dependence of CYT-6091 for enhancement of cryosurgical injury [84, 85]. In a pilot translational study using VX2 tumors grown in rabbit kidneys, we also obtained a significant decrease in the rate of peritoneal carcinomatosis (metastases) in animals treated with cryosurgery and CYT-6091 compared to cryosurgery alone [109]. This was an unexpected finding and further investigations are underway in preclinical tumor models to interpret whether this was a direct effect on mechanisms of tumor spread or a stimulation of antitumor immunity.

1.3.8. Potential for Enhanced Imaging by Nanoparticle Pre-Conditioning. While we have shown that nanoparticle pre-conditioning is capable of enhancing both hyperthermic

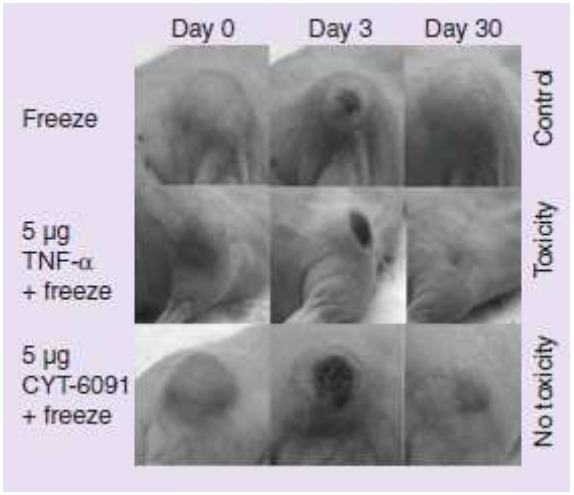

Figure 1.5. Cryosurgical Destruction of LNCaP Hindlimb Tumors. 200 µg TNF-α/kg of CYT-6091 was intravenously administered 4 hours prior to cryosurgery of LNCaP hindlimb tumors grown in nude mice. Cryosurgery was conducted using a Joule-Thomson based argon cryoprobe with the tip temperature maintained at -100^{o}C. Cryosurgery was conducted until the edge of the iceball overlapped the visual edge of the tumor. Toxicity (animal death) and tumor growth was monitored for a period of 30 days after treatment. The results show that CYT-6091 pre-conditioning followed by cryosurgery enables complete tumor regression without toxicity whereas significant toxicity is associated with native TNF-α pre-conditioning [84].

and cryosurgical injury in solid tumors, another important potential of this concept lies in its ability to enhance the clinical imaging techniques associated with thermal therapies. For instance, pre-conditioning events can be imaged to provide longitudinal monitoring of the state of pre-conditioning to optimize the time of administration of the secondary treatment. We have already shown that the administration of CYT-6091 is accompanied by a significant 80% reduction in tumor perfusion [67, 68]. Hence, current imaging technologies such as computed tomography (CT), magnetic resonance imaging (MR) or even contrast enhanced ultrasound (CEUS) may prove useful in measuring perfusion drops associated with pre-conditioning that signal an optimal timing for thermal therapy [110, 111]. Similarly, the development of myeloperoxidase-specific imaging agents offers the unique opportunity of monitoring the tumor biology before and after therapy by imaging the recruitment of neutrophils into the tumor tissue [112, 113]. Recent data collected in our lab has shown, on histology, the presence of a neutrophil rich inflammatory infiltrate that peaks at day 3 after TNF-α enhanced cryosurgery (**Figure 1.6A-B**) [91]. In this work, LNCaP tumors were grown in DSFCs implanted on nude mice. Tumors were pre-conditioned using topical administration of 200 ng native TNF-α 4 hours prior to cryosurgery. Intravital imaging, thermography, and post-sacrifice histology and immunohistochemistry were used to longitudinally assess iceball location and the ensuing biological effects (e.g. neutrophil infiltration) after cryosurgery with and without TNF-α pre-treatment within the DSFC tumor tissue. In a separate experiment using TRAMP-C2 tumors grown subcutaneously in nude mice, we have also shown that this recruitment of neutrophils to the tumor site post cryosurgery can be non-invasively

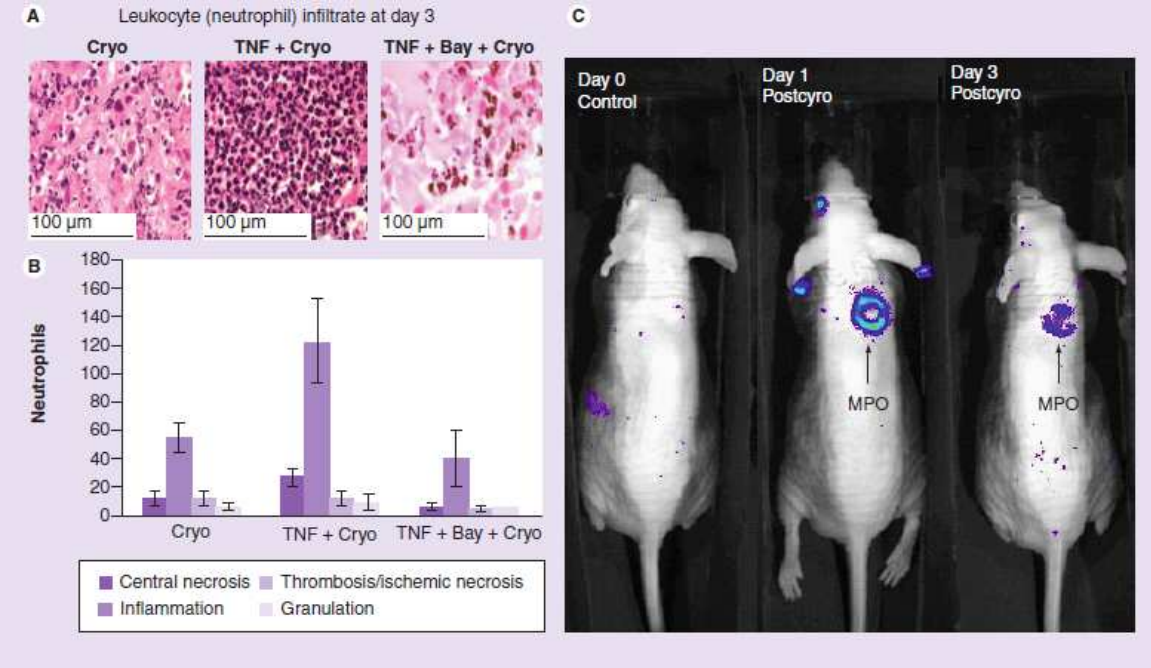

Figure 1.6. Potential for Non-invasive Imaging of Neutrophil Infiltration into Thermal Lesion. (a) Leukocyte (neutrophils) infiltrate at day 3 post cryosurgery with or without TNF-α pre-conditioning. Animals were treated with cryosurgery alone, TNF-α 4 hours pre-conditioning plus cryosurgery, or NFκB inhibitor BAY followed by TNF-α 4 hours pre-conditioning plus cryosurgery. Representative image of neutrophilic infiltrate with H&E staining was taken under high power (100× magnification) within the inflammation zone (scale bar =100µm). (b) Quantification of neutrophils within each histological zone under high power field. The average number of neutrophils was measured in five representative fields in each histological layer for each sample. The bar values represent mean ± SD of three to four independent experiments for each treatment. The numbers of neutrophils per field were significantly different between the combinatorial treatment and cryosurgery alone (*, $p<0.05$) [91]. (c) Luminol bioluminescence imaging of myeloperoxidase (MPO) activity in TRAMP-C2 tumors in vivo following cryosurgery (unpublished results).

imaged using luminol bioluminescence imaging (**Figure 1.6C**, unpublished results). Based on these preliminary findings, we speculate that the enhancement of neutrophil recruitment by nanoparticle pre-conditioning can be imaged and quantified using myeloperoxidase-specific imaging agents. Additionally, since we have shown that these pre-conditioning events (perfusion drop and neutrophil recruitment) persist and are enhanced after thermal therapy, we hypothesize that they may be used to quantify treatment effects and serve as prognostic indicators of the outcome of thermal therapy. This hypothesis is the basis of ongoing work in our group.

Nanoparticle pre-conditioning can also be used to predict the lethality of the thermal therapy in the case of cryosurgery. Many clinical imaging technologies including ultrasound, CT and MR easily distinguish the edge of the cryosurgical iceball in vivo [114]. Unfortunately, the current guideline for cancer destruction by freezing requires temperatures below a critical -40 °C isotherm [115, 116]. This is achieved in less than 50% of the total 3D iceball volume, assuming the iceball to be roughly elliptical and the probe temperature to be roughly -160 °C [117]. It has understandably led to confusion about how much of the tissue and/or cancer to freeze during cryosurgery. This confusion persists today and undoubtedly contributes to under and over freezing that yield local recurrence and complications respectively. With nanoparticle pre-conditioning, we have shown in the DSFC model that we can move the tissue-destruction isotherm to -0.5 °C, suggesting that cryosurgical destruction can be effectively doubled and intra-operative imaging of the iceball correlates to destruction, since in such conditions, “what you see

(iceball) is what you get (destruction)" [84, 118]. This finding also translated to the hindlimb model in which cryosurgery was performed until the edge of the iceball overlapped with the visible edge of the tumor yielding apparent remission in a significant percent of animals (**Figure 1.5**) [84]. These data suggest the clinical use of a nanoparticle system, such as CYT-6091, could enable the surgeon for the first time to visualize the zone of tumor destruction by simply imaging the ice formation during cryosurgery.

1.4. CONCLUSIONS

The concept of pre-conditioning the tumor microenvironment using nanoparticles is relatively new and many avenues of basic and clinical research particularly for use in the field of thermal therapy enhancement remain largely open. Our group has demonstrated the use of a gold nanoparticle system (CYT-6091), which has recently completed a Phase I clinical trial and moved into Phase II as a standalone cancer therapeutic, to pre-condition a variety of preclinical tumor models prior to thermal therapies (using both heat and cold) (**Table 1.4**). Pharmacokinetic and biodistribution studies of CYT-6091 have shown tumor-specific drug and nanoparticle localization and we have demonstrated that a single systemic injection of the nanoparticle at a critical time period (4 hours) prior to thermal therapy suffices to pre-condition the tumor with no overt toxicity. Further, vascular (perfusion defect) and immunological (leukocyte recruitment) mechanisms responsible for pre-conditioning using CYT-6091 have been demonstrated by various techniques and suggest imaging as a possible clinical tool for assessment of

the optimal time for subsequent thermal therapy intervention. Thermal therapy outcomes after appropriate pre-conditioning with CYT-6091 have been able to induce tumor regression without toxicity (**Table 1.4, Figures 1.3, 1.5**), establishing the validity of this clinically realistic approach.

1.5. FUTURE PERSPECTIVE

The constantly evolving and heterogeneous nature of cancer has resulted in a shift from single agent therapy to multi-drug regimens and combinatorial therapies for improved local and metastatic control. This is particularly true for thermal therapy in cancer which is currently dominated by regional hyperthermia combined with standard-of-care chemotherapy and/or radiotherapy for a wide variety of tumors. More recently, focused minimally invasive thermal therapy approaches such as cryosurgery, microwave, and radiofrequency ablation (**Table 1.2**) are also finding favor with clinicians and several clinical trials are in progress to test the efficacy of combinatorial therapy using these techniques with chemotherapeutics. A small subset of these trials involves thermal therapies with commercially manufactured nanoparticles (**Table 1.1**). This subset of clinical trials represents the successful realization of preclinical research efforts over the past decade in nanomedicine and heralds a new future in cancer therapy. Some of the key challenges going forward are: (1) selection of the appropriate nanoparticle, pre-conditioning agent and thermal therapy for the specific tumor type; (2) demonstration of selective nanoparticle delivery, safety and efficacy and expanded understanding of

nanomedicine toxicological considerations; (3) timing and guidance of thermal therapy perhaps by imaging pre-conditioning after nanoparticle administration; and (4) controlling the extent of thermal intervention necessary to kill the tumor. As we await future nanoparticle development and optimization, even today there may be few barriers to the use of existing manufactured nanoparticles (i.e. CYT-6091) to pre-condition and treat solid cancers with thermal therapies in Phase I/II clinical trials.

1.6. SUMMARY

- Clinical acceptance of current thermal therapy approaches for local treatment of solid tumors is hindered by local recurrence and distant metastases following therapy.
- Nanoparticles are being investigated as mediators for novel methods of in situ delivery of thermal energy to tumors, such as magnetic fluid hyperthermia, photothermal therapy, radiofrequency heating, etc.
- Nanoparticles delivering chemotherapeutics to tumor tissue also show clinical utility in enhancing direct destruction of tumor cells in combination with thermal therapy.
- Nanoparticle pre-conditioning is a new concept using nanoparticles functionalized with bioactive ligands to enhance vascular and immunological mechanisms of tumor destruction by thermal therapies.
- CYT-6091, a 30nm diameter colloidal gold nanoparticle coated with PEG and tagged with TNF-α, has shown efficacy in pre-conditioning tumors for enhancement of thermal (heat and cold) therapies.

- Pharmacokinetics and biodistribution studies have shown selective accumulation of CYT-6091 and pre-conditioning of tumors within 4 hours of systemic administration.
- We have demonstrated that CYT-6091 enhances thermal therapies primarily via vascular pre-conditioning with some evidence for immunological pre-conditioning events.
- Pre-clinical studies in mouse and rabbit tumor models have shown significant enhancement of tumor destruction by thermal therapies when CYT-6091 is used for pre-conditioning the tumor vasculature.
- Imaging of pre-conditioning events such as perfusion drop and inflammatory cell recruitment may be used to quantify treatment effects and serve as prognostic indicators of the outcome of thermal therapy.
- In cryosurgery, nanoparticle pre-conditioning can move the critical isotherm of tumor cell death to the iceball edge (-0.5^{o}C), suggesting that intra-operative imaging of the iceball would directly correlate to the region of tumor destruction.
- Based on these positive results for nanoparticle pre-conditioning, improved multifunctional nanoparticles with alternative ligands could be designed to enhance thermal therapies by decreasing systemic toxicity and increasing tumor targeting with the ultimate goal of reducing local recurrence and distant metastases and reducing morbidity in patients.

Chapter 2: Nanoparticle Preconditioning of Thermal Therapy in a Preclinical Model of Prostate Cancer

This chapter describes the use of nanoparticle preconditioning to enhance thermal therapy in a preclinical tumor model of human prostate cancer. This is the first time that high and low temperature thermal therapies and their enhancement by nanoparticle preconditioning are directly compared in a given preclinical tumor model of prostate cancer. This was performed in both two dimensional (dorsal skin fold chamber) and three dimensional (hindlimb) tumor models in nude mice.

- Shenoi MM, Schmechel S, Bischof JC. Enhancement of High and Low Temperature Thermal Therapy in Prostate Cancer with Nanoparticle Preconditioning. 2011 (manuscript in preparation for submission to Nanomedicine) submission invited by editor, Lajos P. Balogh.

2.1. INTRODUCTION

Prostate cancer is the most common malignancy and the second leading cause of cancer-related deaths among males in the United States of America [119, 120]. Most patients with prostate cancer have well differentiated tumors (Gleason grade < 6) and will respond to monotherapy with surgery, radiation or thermal therapy including cryosurgery. However, high-grade disease (Gleason grade >8-10), which makes up 15-20% of patients with prostate cancer, is responsible for greater than 50% of the deaths attributed to prostate cancer [121]. Such patients are at high risk for both local and distant recurrences. Patients with high-grade disease require multimodal therapy with available options including radiation plus androgen ablation, and clinical trials are investigating the combination of surgery and chemotherapy [122]. Better treatments are urgently needed for these patients with high grade prostate cancer who are at high risk for local recurrence.

Tumor vasculature is an attractive therapeutic target in the ongoing battle against cancer as evidenced by the large number of clinical trials involving small molecule vascular disruptive agents (VDAs) [123]. Numerous pre-clinical studies have demonstrated the efficacy of combining VDAs with hyperthermia, radio- and chemo-therapy and many of these approaches are now under clinical evaluation [43, 123]. However, these trials show negligible improvement in the efficacy of frontline therapies, i.e. chemotherapy and radiation, by the addition of VDAs. They are also plagued by dose

limiting toxicities of the VDAs [123]. This pattern of anti-cancer drug failure is similar to what happened with native TNF in the early 1990's when systemic TNF administration for cancer treatment was associated with induction of a 'cytokine storm' resembling many signs and symptoms of endotoxic shock resulting in limited use of TNF in cancer therapy [124]. Hence, there exists an enormous clinical need for new directions of investigations in combination therapies.

Nanomedicines are gaining increasing traction in the advancement of cancer therapy due to their ability to selectively and safely deliver a therapeutic payload to tumors with the added potential for improved diagnostics and imaging. Concurrently, thermal ablation therapies are also gaining clinical acceptance for the treatment of focal malignancies in several organs including prostate. Several technologies have been developed for the delivery of thermal energy to tumor tissues. These include radiofrequency ablation (RFA), cryoablation, high-intensity focused ultrasound (HIFU), microwaves, lasers, etc. These can simply be classified into low temperature cryosurgery (cryoablation) and high-temperature thermal therapy (RFA, HIFU, microwave, etc.).

A combination therapy utilizing a thermal ablation therapy along with a nanoparticle formulation of a VDA (i.e. TNF) could make a considerable clinical impact in cancer treatment.

Native TNF has been combined successfully with hyperthermia (<43^{o}C) in preclinical tumor models with high therapeutic efficacy [43]. Prior to the current study, our lab has also successfully demonstrated that nanoparticle delivered TNF (CYT-6091) can precondition hyperthermia and cryosurgery in a variety of preclinical tumor models [67, 68, 84]. However we have not demonstrated that high-temperature thermal therapy (>50^{o}C) and cryosurgery could be accentuated in the same tumor model for prostate cancer. We describe here the use of a gold nanoparticle delivery system for TNF to selectively modify, or precondition, tumor vasculature so as to enhance the antitumor effects of a secondary challenge i.e. thermal therapy (heat and cold).

2.2 MATERIALS AND METHODS

Cell Culture

LNCaP Pro 5 cells were cultured as adherent monolayers in Dulbecco's modified Eagle's medium (DMEM)/F12 media (BD Biosciences, San Jose, CA) supplemented with 10% of fetal bovine serum, 100 U/ml penicillin, 100 µg/ml streptomycin, and 10^{-9} mol/L dihydrotestosterone (DHT) as previously described [118]. Cultures were maintained in a 37°C/5% CO2/95% humidified air environment. Cells were subcultured (1:6) twice per week, by rinsing flasks with Hank's balanced salt solution (HBSS), followed by trypsinization, enzyme neutralization, and reseeding.

Animals

All animal protocols were reviewed and approved by the University of Minnesota Institutional Animal Care and Use Committee. 6-8 week old athymic male NU/J mice were obtained from the Jackson Laboratory (Bar Harbor, ME). Animals implanted with dorsal skin fold chambers (DSFCs) were housed in neonatal incubators under conditions of higher than normal humidity at 37°C to maintain tissue microvasculature [94]. When appropriate, animals were anesthetized by an i.p. injection of ketamine (100 mg/kg) and xylazine (10 mg/kg).

DSFC and Tumor Cell Implantation

A DSFC was implanted in each nude mouse as previously described [84]. Immediately after DSFC implantation and on day 4 after implantation, 1 million LNCaP Pro 5 cells suspended in 40 μl Matrigel (BD Biosciences, San Jose, CA) that had been diluted 3:1 in serum-free medium were seeded into the DSFC chamber window. Thermal therapy experiments were performed between day 12 and 14 following DSFC implantation, when tumor cells were found to cover the entire chamber window as previously reported [84, 91, 118].

Hindlimb Tumor Seeding

5 million LNCaP Pro 5 cells suspended in 100 μl Matrigel (BD Biosciences, San Jose, CA) that had been diluted 3:1 in serum-free medium were injected s.c. into the hindlimb of the mouse. Experiments were performed after 4 to 5 weeks, when the tumors reached a diameter of 6 to 8 mm.

Nanoparticle Administration

CYT-6091 (CytImmune Sciences, Inc., Rockville, MD, USA) at a dose containing 5 μg of TNF-α was diluted in 100 μl DI water and injected via tail vein into the mice 4 hours prior to thermal therapy. In experiments with control nanoparticles, AuPEG (PEGylated colloidal gold nanoparticle without TNF-α, CytImmune Sciences, Inc.) were administered in the same manner at an equivalent dose to injected CYT-6091 based on total surface area of injected particles. The 5 μg TNF-α dose and 4 hour time period were chosen based on previous work with CYT-6091 [68, 84].

DSFC Cryosurgery

Cryosurgery was performed as described previously [66, 84]. Briefly, animals were anesthetized, DSFC windows were removed and a 1 mm diameter brass extension tip fitted to a 5 mm cryoprobe (Endocare, Irvine, CA) was inserted into the center of the DSFC for 55 seconds (to attain temperatures of -85°C) followed by passive thawing at room temperature. The temperature was monitored throughout the procedure using an infrared camera ThermoVision (FLIR Systems, Boston, USA) and thermocouples placed at 2, 3 and 4 mm radial positions around the DSFC center [84].

DSFC High-Temperature Thermal Therapy

Animals were anesthetized and loaded into a sterilized polycarbonate tube with the DSFC exposed. DSFC windows were removed and heating was initiated from the central

portion of the window using a 1 mm diameter brass extension tip fitted to a temperature controlled soldering iron tip (RadioShack Digital Soldering Station 64-053, RadioShack, Fortworth, TX, USA). When the soldering iron is set to temperature of 150^{o}C a temperature of 80^{o}C was obtained at the end of the brass extension tip. This allowed a radial heating front to develop from the center of the DSFC tissue and the temperature to be monitored using infrared thermography and thermocouples similar to the cryosurgery procedure. The soldering iron was switched off when the thermocouple positioned 2 mm away from the center of the DSFC reached 45^{o}C and the tissue was allowed to passively cool to room temperature. Total heating time was less than 10 min.

Hindlimb Cryosurgery and High-temperature Thermal Therapy

Cryosurgery was performed using a cryosurgical system (Endocare, Inc., Irvine, CA, USA), as described previously, with a 1 mm probe tip modification on a 3 mm tip cryoprobe [84]. A small incision was first made in the center of the hindlimb tumor with a 21-gauge needle to allow insertion of the probe tip without deformation of the tumor. The cryoprobe was activated by allowing the argon cryogen to flow, and the 1 mm probe tip temperature was set at -120 ºC. Freezing was performed conservatively under infrared thermographic guidance until the 0°C isotherm reached the visible edge of the tumor. The tumor was then passively thawed to room temperature. For high-temperature thermal therapy, the 1 mm diameter brass extension tip was fitted to a temperature controlled soldering iron tip (RadioShack Digital Soldering Station 64-053, RadioShack, Fortworth, TX, USA) and inserted into the tumor after a small incision was made with a 21-gauge

needle. The soldering iron was switched on at the lowest temperature (150^{o}C) setting and the tumor was heated conservatively under infrared thermographic guidance until the 40°C isotherm reached the visible edge of the tumor. The soldering iron tip was then removed and the tumor was passively cooled to room temperature.

Vascular Stasis Measurement

On days 1 and 3 following thermal therapy (with or without nanoparticle administration), 0.1 ml of 10 mg/ml 70-kDa FITC-labeled dextran (Sigma, St. Louis, MO) was injected into the tail vein of each animal. Intravital imaging of tumor vasculature in the DSFC was performed using a Nikon inverted fluorescent microscope equipped with a 20× objective (Nikon, Melville, NY) and silicon intensified transmission camera (Hamamatsu, Bridgewater, NJ) as previously described [66, 84, 91]. The average radius at which patent blood vessels with blood flow were clearly visible defined the region of vascular stasis and was measured at four perpendicular radial directions relative to the chamber center. The stasis area was calculated as π x (average radius)^2.

Tumor Growth Delay Measurement

Baseline tumor size in the hindlimb was measured prior to cryosurgery. Tumor growth is reported relative to the size prior to cryosurgery. Tumor volumes were measured every 3 days for 30 days after thermal therapy. Tumor dimensions were measured using calipers and volumes were calculated and reported as 0.53 × width × length × height [84, 85].

Histology

Animals were sacrificed at day 3 post DSFC cryosurgery or high-temperature thermal therapy immediately after vascular imaging. The entire tumor tissue attached to the chamber was fixed in 10% buffered formalin (Sigma, St. Louis, MO), embedded in paraffin, sectioned at 4 μm and stained with hematoxylin-eosin (H&E). Histologic sections were digitized using Leica MZ FL III fluorescence stereomicroscope (Leica Microsystems, Heerbrugg, Switzerland), and the area of central necrosis was analyzed using ImageJ (NIH, Bethesda, MD, USA).

Statistics

Statistical significance was determined using the wilcoxon test in R statistical software [125]. If the difference was at the level of $p<0.05$, it was determined significant. Otherwise, the difference between two measurements was not significant, i.e., $p>0.05$. Data are represented as mean ± SE.

2.3. RESULTS & DISCUSSION

NP preconditioning enhances cryosurgery in a 2D DSFC tumor model

Cryosurgical injury in DSFC LNCaP tumors was assessed in three groups of nude mice: a) Control (receiving only cryosurgery), b) AuPEG and c) CYT-6091. Mice in AuPEG and CYT-6091 groups were injected with the corresponding nanoparticle 4 hours prior to cryosurgery. Cryosurgical injury was assessed by vascular stasis measurements after 70kDa FITC-dextran injection at Day 1 and Day 3 post treatment and Day 3 histology of

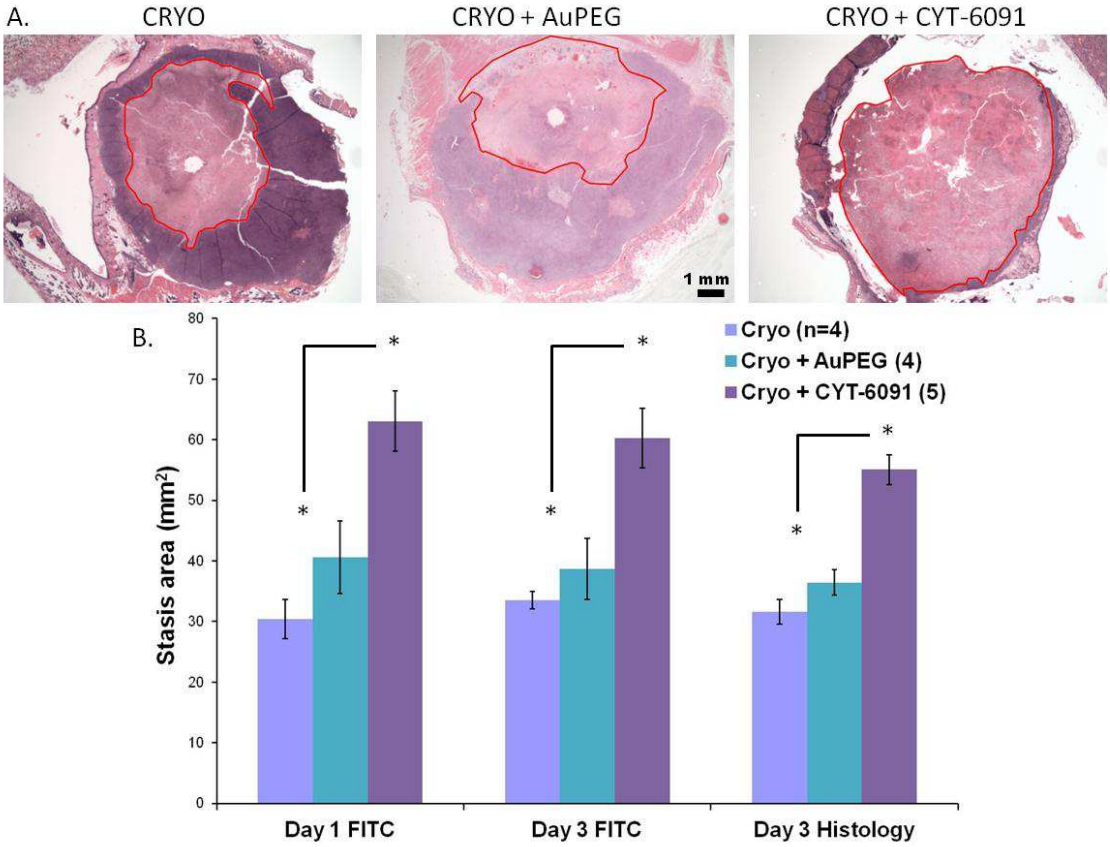

Figure 2.1. NP preconditioning enhances cryosurgical injury in DSFC LNCaP tumors. A) Representative H&E stained sections of entire DSFC tumors at Day 3 after cryosurgical treatment with or without nanoparticle preconditioning. Histological stasis areas are outlined in each section. B) Vascular and histological stasis area measurements. Data presented as mean ± SE. (* indicates $p < 0.05$)

Treatment	n	Treatment	Thermal Threshold	Radial Threshold	**Treated Volume Increase**
Cryosurgery	4	-	-8.0 ± 1.9 °C	3.3 ± 0.1 mm	
	4	+ AuPEG	-7.3 ± 2.0 °C	3.5 ± 0.2 mm	
	5	+ CYT-6091	8.3 ± 1.0 °C	4.4 ± 0.2 mm	**80% (+ CYT-6091 effect)**
Heat	6	-	40 ± 1.2 °C	3.2 ± 0.2 mm	
	4	+ AuPEG	42 ± 1.0 °C	3.0 ± 0.2 mm	
	5	+ CYT-6091	36 ± 1.0 °C	4.1 ± 0.1 mm	**61% (+ CYT-6091 effect)**

Table 2.1. Summary of effects of nanoparticle preconditioning on enhancement of thermal therapy in DSFC LNCaP tumors.

the cryosurgical lesion (**Figure 2.1, 2.2B**). The area of vascular stasis was significantly greater in the CYT-6091 group compared to the control ($p = 0.02$, Day 3) and AuPEG ($p = 0.03$, Day 3) groups at Day 1 and Day 3 as shown in **Figure 2.1B**. No significant difference was evident between Day 1 and Day 3 measurements. This translates to an 80% increase in the treated tumor volume with nanoparticle preconditioning (**Table 2.1**). The lowest temperatures measured at the edge of the stasis region reflect the increased susceptibility of the tumor to cryosurgical injury after nanoparticle preconditioning. CYT-6091 administration reduced the thermal threshold of injury from $-8.0 \pm 1.9^{o}C$ and $-7.3 \pm 2.0^{o}C$, in the control and AuPEG groups respectively, to $8.3 \pm 1.0^{o}C$ (**Table 2.1**).

Day 3 histology of the treated tumors revealed distinct histological zones concentric to the cryoprobe tract characteristic of cryosurgical lesions as reported previously (**Figure 2.1A**) [91, 118]. A zone of central necrosis was present immediately adjacent to the cryoprobe tract and characterized by increased eosinophilic staining with necrotic tumor cells with absent or pyknotic nuclei undergoing karyorrhexis and karyolysis and few scattered inflammatory cells. In the control and AuPEG groups the central necrotic zone was surrounded by a ~0.5-1mm band of inflammatory cells (mostly neutrophils) which in turn was surrounded by a thrombosis/ischemic necrosis zone and viable tumor tissue. In the CYT-6091 group, the central necrosis zone was larger with almost no inflammatory cells. Additionally, the inflammatory band and the zone of thrombosis/ischemic necrosis were narrower and closer to the edge of viable tumor tissue. The histological stasis areas (defined by the boundary between the cryosurgical

lesion and the edge of viable tumor tissue) obtained at Day 3 correlated well with the trend seen in the vascular stasis areas i.e. the histological stasis area of CYT-6091 group was significantly larger than the control and AuPEG groups. The slight difference observed in the CYT-6091 group between the Day 3 histology and vascular stasis areas was not statistically significant ($p = 0.31$).

NP preconditioning enhances high-temperature thermal therapy in a 2D DSFC tumor model

Similar to cryosurgery, thermal injury by high-temperature thermal therapy (HTT) in DSFC LNCaP tumors was assessed in three groups: a) Control (receiving only HTT), b) AuPEG and c) CYT-6091. Temperature profile during the course of high-temperature thermal therapy (HTT) was characterized within the DSFC (**Figure 2.2A**) and temperatures >50^{o}C were obtained in the tumor within 2 mm of the probe tip (80^{o}C). Thermal injury was assessed by vascular stasis measurements after FITC-dextran injection at Day 1 and Day 3 post treatment and Day 3 histology of the thermal lesion (**Figure 2.3**). The area of vascular stasis was significantly greater in the CYT-6091 group compared to the control ($p = 0.02$, Day 3) and AuPEG ($p = 0.02$, Day 3) groups at Day 1 and Day 3 as shown in **Figure 2.3B**. This translates to a 61% increase in the treated tumor volume with nanoparticle preconditioning (**Table 2.1**). As in cryosurgery, CYT-6091 administration reduced the thermal threshold of injury from 40 ± 1.2^{o}C and 42 ± 1.0^{o}C, in the control and AuPEG groups respectively, to 36 ± 1.0^{o}C (**Table 2.1**).

A.

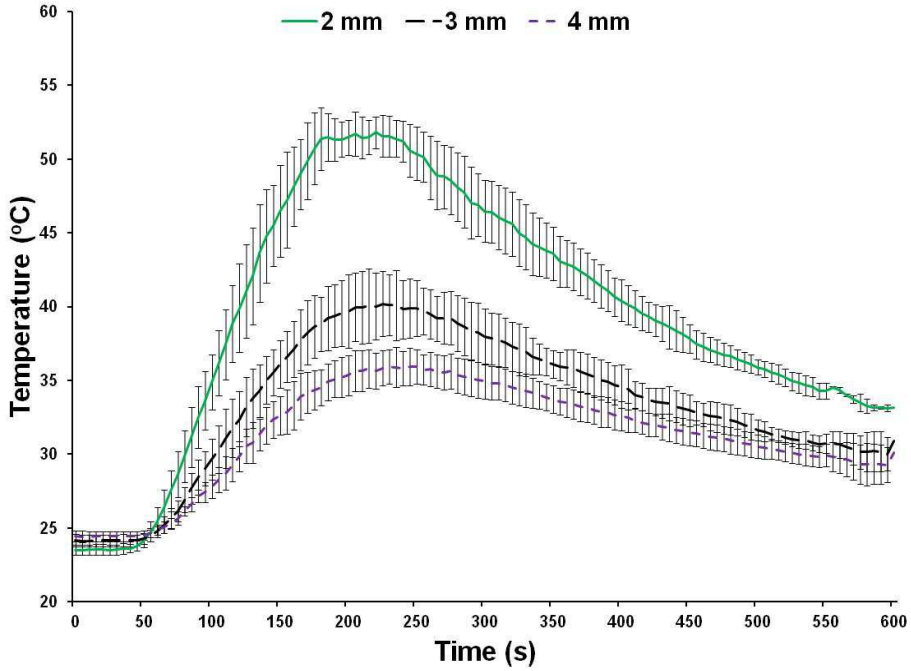

B.

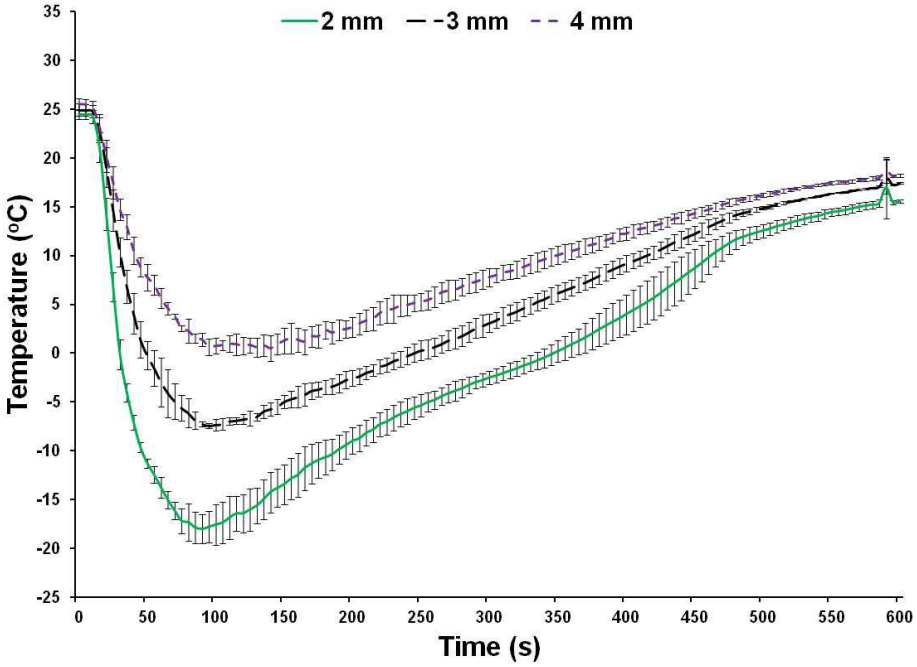

Figure 2.2. Graph of the temperatures recorded by thermocouples at 2, 3, and 4 mm radial locations in DSFC LNCaP tumor tissue during A. high-temperature thermal therapy and B. cryosurgery. Data presented as mean ± SE for each time point.

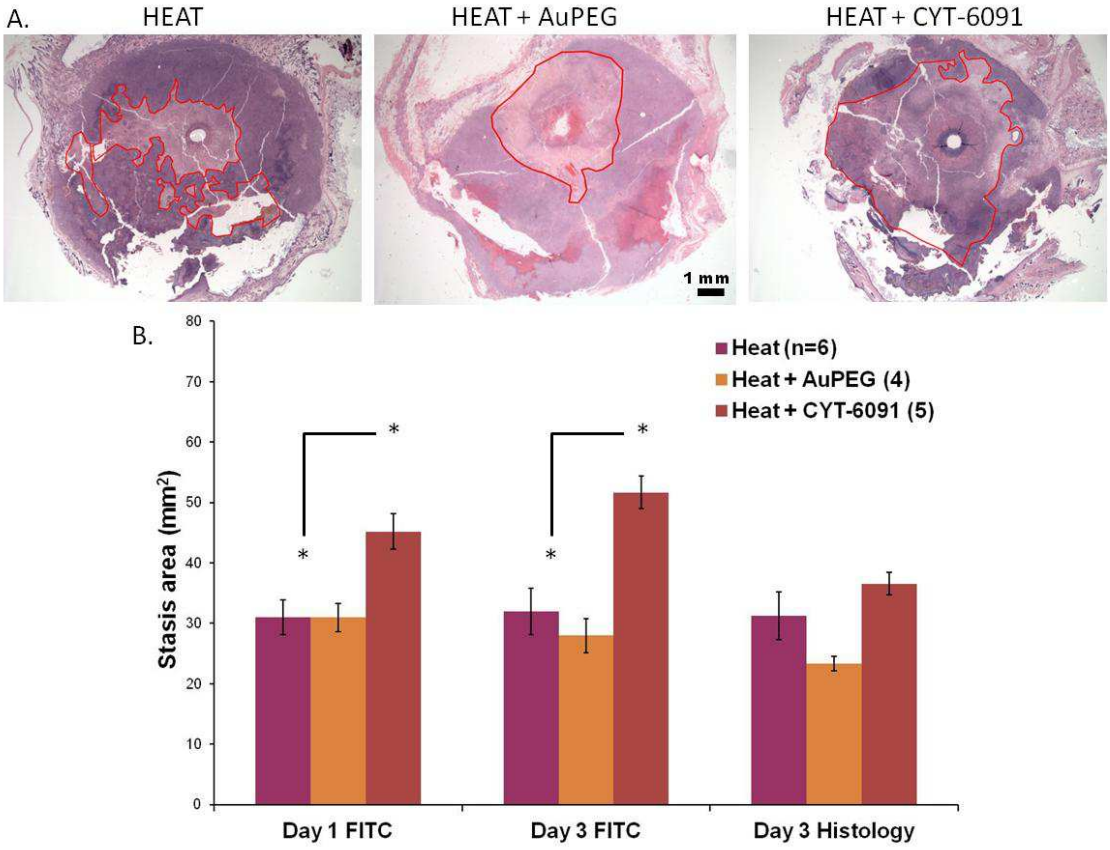

Figure 2.3. NP preconditioning enhances thermal injury in DSFC LNCaP tumors. A) Representative H&E stained sections of entire DSFC tumors at Day 3 after high-temperature thermal treatment with or without nanoparticle preconditioning. Histological stasis areas are outlined in each section. B) Vascular and histological stasis area measurements. Data presented as mean ± SE. (* indicates $p < 0.05$)

Day 3 histology of the HTT treated tumors revealed distinct histological zones concentric to the probe tract characteristic of thermal lesions as reported previously (**Figure 2.3A**) [126-128]. The histologic zones were similar to those seen after cryosurgery with some marked differences. The tissue within the central necrotic zone immediately adjacent to the probe tract appeared "thermally fixed" with architectural and cytologic preservation similar to that seen after formalin fixation. Also, the central necrotic zone had less intense eosinophilic staining compared to cryosurgical lesions and more nuclear staining. The edge of the thermal lesion was in general less circular with more jagged edges compared to the cryosurgical lesions obtained. The histological stasis area obtained at Day 3 was significantly lower than the vascular stasis area for the CYT-6091 group ($p < 0.01$). However, there was no statistically significant difference between the control and AuPEG groups' histological and vascular stasis areas.

NP preconditioning enhances cryosurgery in a 3D hindlimb tumor model

Tumor growth delay was assessed in four groups to demonstrate enhancement of cryosurgery by nanoparticle preconditioning. The groups were: a) Control (no treatment), b) Cryo (receiving cryosurgery alone), c) AuPEG (receiving AuPEG 4 hrs prior to cryosurgery), and d) CYT-6091 (receiving CYT-6091 4hrs prior to cryosurgery). Cryosurgery was performed conservatively until the edge of ice formation reached the visible edge of the tumor as guided by infrared thermography. The volume of CYT-6091 tumors regressed significantly to 50 ± 5.6% within 6 days of cryosurgery (**Figure 2.4A**). The volume of AuPEG tumors regressed to a lesser extent to 73 ± 8.9% whereas no

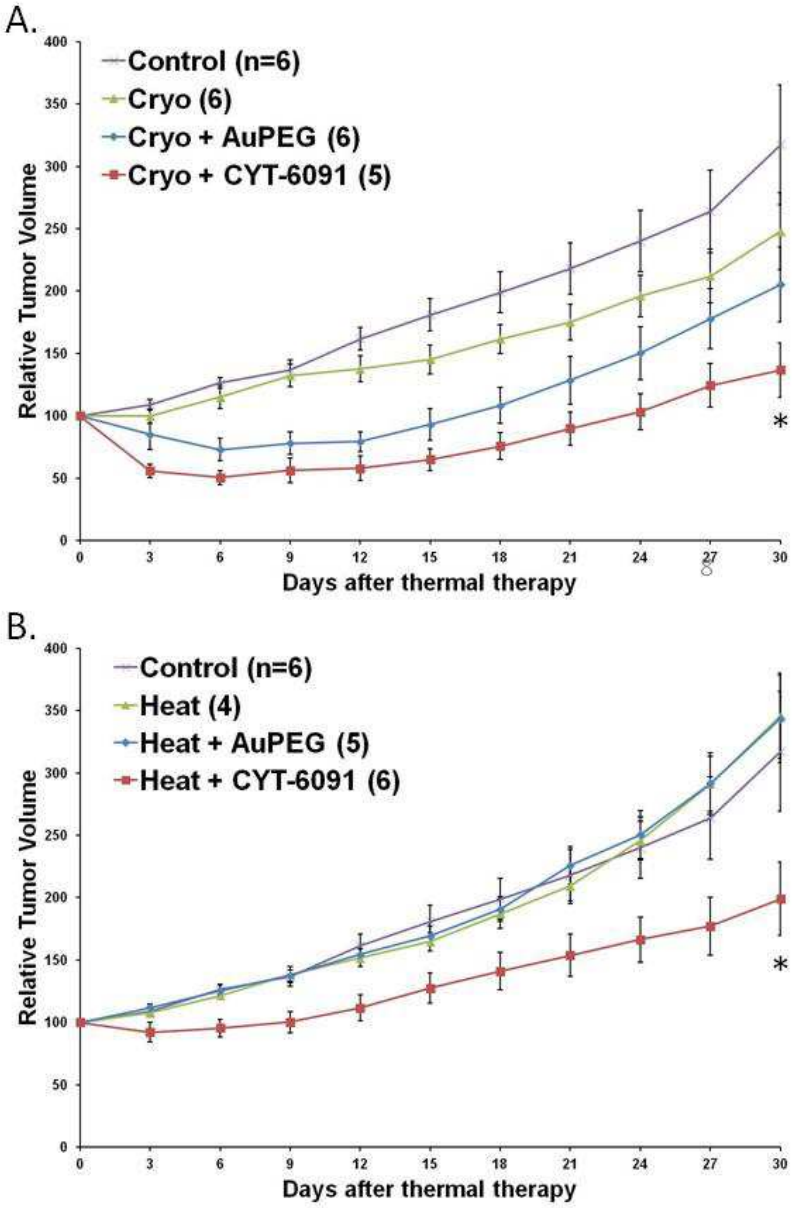

Figure 2.4. NP preconditioning enhances thermal therapy in hindlimb LNCaP tumors. A) Tumor growth delay after cryosurgery of hindlimb LNCaP tumors with and without nanoparticle preconditioning (* $p<0.05$, between CYT-6091 and both the control and cryo groups). B) Tumor growth delay after high-temperature thermal therapy of hindlimb LNCaP tumors with and without nanoparticle preconditioning (* $p<0.05$, between CYT-6091 and all other groups).

regression was seen in the control or cryo groups. At Day 30 after cryosurgery, the relative tumor volumes of control, cryo and AuPEG groups were not statistically different from each other. CYT-6091 group relative tumor volumes were significantly lower than the control and cryo groups ($p = 0.02$) but not significantly different from the AuPEG group. No signs of toxicity were observed in any of the animals.

NP preconditioning enhances high-temperature thermal therapy in a 3D hindlimb tumor model

Tumor growth delay was also assessed in four groups to demonstrate enhancement of HTT by nanoparticle preconditioning. The groups were: a) Control (no treatment), b) Cryo (receiving HTT alone), c) AuPEG (receiving AuPEG 4 hrs prior to HTT), and d) CYT-6091 (receiving CYT-6091 4hrs prior to HTT). HTT was performed conservatively until the visible edge of the tumor reached 40^{o}C as guided by infrared thermography. In this case there was no regression of tumor volumes in any group. However, over the course of 30 days following HTT, the CYT-6091 tumors exhibited a greater growth delay compared the other groups (**Figure 2.4B**). At Day 30 after HTT, the relative tumor volumes of control, HTT and AuPEG groups were not statistically different from each other but CYT-6091 group relative tumor volumes were significantly lower than all the other groups ($p = 0.02$, AuPEG). No signs of toxicity were observed in any of the animals.

2.4. CONCLUSIONS

The data presented here shows that NP preconditioning can enhance cryosurgery and high-temperature thermal therapy (HTT) in a preclinical prostate cancer model in both 2D DSFC and 3D hindlimb tumor models with no systemic toxicity. Thermal thresholds of injury were reduced in both heat and cold thermal therapies by NP preconditioning. In the 2D DSFC model, NP preconditioning led to an 80% increase in the treated tumor volume by cryosurgery while a 61% increase was obtained with HTT. Despite the conservative thermal threshold protocols (edge of tumor = iceball edge or 40^{o}C) used for hindlimb thermal therapy a significant therapeutic benefit (tumor growth delay) was still realized due to NP preconditioning. Importantly, there were no deaths in any of the animal groups which is in agreement with previous data obtained in our lab [84, 85].

Chapter 3: Nanoparticle Preconditioning Mechanisms – Vascular and Immunological Events

This chapter describes experiments to elucidate the vascular and immunological mechanisms involved in nanoparticle preconditioning in a preclinical tumor model of human prostate cancer.

- Shenoi MM, Schmechel S, Bischof JC. Vascular and Immunological Mechanisms of Nanoparticle Preconditioning. 2011 (manuscript in preparation for Nano Letters)

3.1. INTRODUCTION

Nanoparticle preconditioning has been shown to enhance thermal therapy with potential to be expanded to other combination therapies (i.e. radiation, chemotherapy) in the future. Before this approach can be widely accepted and used, the underlying mechanisms of this pre-conditioning are still needed. As described in our recent review, pre-conditioning can be achieved by a variety of agents (see Table 1.3, Chapter 1), however, the most mature nanoparticle technology is CYT-6091, a gold nanoparticle tagged with TNF-α. White blood cells, endothelial cells and tumor cells are the components of tissue which are directly affected by TNF-α. TNF-α induces expression of adhesion molecules such as ICAM-1, VCAM-1, and selectins on endothelial cells, thus leading to an enhancement in leukocyte rolling and adhesion. It produces vascular damage by inducing endothelial cell apoptosis and also stimulates them to release cytokines for angiogenesis [129]. TNF-α also activates neutrophils and monocytes by upregulation of adhesion molecules and promotes coagulation [130]. The adhered neutrophils migrate to the interstitium and produce various cytokines (TNF-α, IL-1, IL-8, PDGF) amplifying the inflammatory effect. Neutrophil apoptosis can also be stimulated by TNF-α [131]. Tumor cells also have receptors for TNF-α binding. Thus, each of the cells involved in tumor microenvironment (endothelial, leukocytes, tumor) shows some effect on exposure to TNF-α. The response to TNF-α is based on complex factors and final response depends on the dominance of the two molecular pathways (apoptotic death and inflammatory).

TNF-α has multiple effects on the tissue vasculature. Increase in flux of leukocytes cause an alteration in blood flow, primarily in capillaries and venules. A decrease in tissue blood perfusion facilitates propagation of thermal ablation by reducing heat sink/source effects due to blood perfusion. Oxidative stress as a result of ischemia/reperfusion injury in cryoablation has been postulated to induce activation of NF-κB through a yet to be identified mechanism. Inflammatory cells themselves release TNF-α and thus mediate inflammation, which is considered to be critical in defining the edge of the thermal lesion. Thus pre-exposure to TNF-α can cause many changes in the tumor microcirculatory environment, which may lead to enhancement of thermal therapy.

Previous research in our lab has been directed towards establishing the therapeutic efficacy of adjuvant mediated preconditioning in enhancing thermal injury in a variety of preclinical tumor models. More recently, the cellular and molecular mechanisms of native TNF preconditioning of cryosurgical injury was studied in LNCaP tumors [66, 91]. In addition, the majority of this work was focused on the progression of the cryosurgical injury over the course of 7 days after cryosurgery. Limited work has been done to date to understand the vascular and immunological events that occur during NP preconditioning. Based on the work conducted in our lab so far, a model for nanoparticle preconditioning was proposed (see Figure 1.4, Chapter 1) and tested via the experiments described in this chapter. The goals of this work were to understand the NP preconditioning mechanisms, including the role of neutrophils in NP preconditioning, and whether nanoparticle delivery of TNF affected the preconditioning mechanisms.

3.2. MATERIALS AND METHODS

Cell Culture

LNCaP Pro 5 cells were cultured as adherent monolayers in Dulbecco's modified Eagle's medium (DMEM)/F12 media (BD Biosciences, San Jose, CA) supplemented with 10% of fetal bovine serum, 100 U/ml penicillin, 100 µg/ml streptomycin, and 10^{-9} mol/L dihydrotestosterone (DHT) as previously described [118]. Cultures were maintained in a 37°C/5% CO2/95% humidified air environment. Cells were subcultured (1:6) twice per week, by rinsing flasks with Hank's balanced salt solution (HBSS), followed by trypsinization, enzyme neutralization, and reseeding.

Animals

All animal protocols were reviewed and approved by the University of Minnesota Institutional Animal Care and Use Committee. 6-8 week old athymic male NU/J mice were obtained from the Jackson Laboratory (Bar Harbor, ME). Animals implanted with dorsal skin fold chambers (DSFCs) were housed in neonatal isolettes under conditions of higher than normal humidity at 37°C to maintain tissue microvasculature [94]. When appropriate, animals were anesthetized by an i.p. injection of ketamine (100 mg/kg) and xylazine (10 mg/kg).

DSFC and Tumor Cell Implantation

A DSFC was implanted in each nude mouse as previously described [84]. Immediately after DSFC implantation and on day 4 after implantation, 1 million LNCaP Pro 5 cells suspended in 40 μl Matrigel (BD Biosciences, San Jose, CA) that had been diluted 3:1 in serum-free medium were seeded into the DSFC chamber window. Thermal therapy experiments were performed between day 12 and 14 following DSFC implantation, when tumor cells were found to cover the entire chamber window as previously reported [84, 91, 118].

Nanoparticle Administration

CYT-6091 (CytImmune Sciences, Inc., Rockville, MD, USA) at a dose containing 5 μg of TNF-α was diluted in 100 μl DI water and injected via tail vein into the mice 4 hours prior to thermal therapy.

NFκB Inhibition

For molecular inhibition of NFκB, the NFκB inhibitor BAY 11-7085 (EMD Biosciences, San Diego, CA; dissolved in DMSO at 10 mg/ml) was topically applied in the DSFC at a dose of 0.4 mg/kg for 15 min [66]. In one experiment after BAY treatment, or without pre-treatment with BAY, CYT-6091 was administered as described above. In another experiment, after BAY treatment, or without pre-treatment with BAY, 200 ng/mouse of TNF-α (a gift from CytImmune Science, Inc., Rockville, MD; dissolved in 30 μl saline), or a sham mixture of saline, was topically applied for 15 min. All animals were treated with cryosurgery 4 hours later as described below.

VCAM-1 Inhibition

For VCAM inhibition, 60 μg of anti-mouse VCAM-1 monoclonal antibody (MAb) (Vector Laboratories, Burlingame, CA) was applied topically 4 hours after CYT-6091 injection [132]. The anti VCAM-1 MAb blocks the binding of α4β1 integrins to VCAM-1. Cryosurgery procedure was performed 15 min after VCAM inhibition.

In vivo Neutrophil Depletion

24 hours prior to CYT-6091 injection, mice were injected intraperitoneally with 150 μg purified RB6-8C5 rat monoclonal antibody (BD Pharmingen, Rockville, MD) in order to systemically deplete granulocytes [133]. Cryosurgery was performed 4 hours after CYT-6091 injection. Systemic depletion was confirmed in a separate set of mice injected with the same dose of RB6-8C5 antibody. About 60-80 μl of blood was collected by facial vein puncture from each mouse on day 1, 2, 3 and 4 after antibody injection and analyzed using an automated cell counter (Hemavet 950, Drew Scientific, Oxford, Connecticut, USA).

DSFC Cryosurgery

Cryosurgery was performed as described previously [66, 84]. Briefly, DSFC windows were removed and a 1 mm diameter brass extension tip fitted to a 5 mm cryoprobe (Endocare, Irvine, CA) was inserted into the center of the DSFC for 55 seconds (to attain temperatures of -100°C) followed by passive thawing at room temperature. The

temperature was monitored throughout the procedure using an infrared camera ThermoVision (FLIR Systems, Boston, USA) and thermocouples placed at 2, 3 and 4 mm radial positions around the DSFC center [84].

Vascular Stasis Measurement

On days 1 and 3 following cryosurgery, 0.1 ml of 10 mg/ml 70-kDa FITC-labeled dextran (Sigma, St. Louis, MO) was injected into the tail vein of each animal. Intravital imaging of tumor vasculature was performed using a Nikon inverted fluorescent microscope equipped with a 20× objective (Nikon, Melville, NY) and silicon intensified transmission camera (Hamamatsu, Bridgewater, NJ) as previously described [66, 84, 91]. The average radius at which patent blood vessels with blood flow were clearly visible defined the region of vascular stasis and was measured at four perpendicular radial directions relative to the chamber center. The stasis area was calculated as π x (average radius)^2.

Vascular Permeability Assessment

TNF-α induced vascular permeability was assessed as previously described [83]. One hour after i.v. administration of CYT-6091 (5 μg of TNF-α) or topical administration of 200 ng of TNF-α as described above, 0.1 ml of 10 mg/ml 70-kDa FITC-labeled dextran was injected into the tail vein of each animal. Images of the DSFC tumor vasculature were obtained every 10 min after FITC-dextran injection up to 1 hour using an Olympus BX50 fluorescent microscope (Olympus Inc., Tokyo, Japan) equipped with a 10X

objective and Spot Diagnostic camera (Diagnostic Instruments Inc., MI, USA). Images were analyzed using ImageJ software (NIH, Bethesda, MD, USA).

Assessment of Tumor Perfusion

Animals were anesthetized by an i.p. injection of ketamine and xylazine at 100 and 10 mg/kg, respectively. 10^6 colored microspheres (10 μm diameter, E-Z-Trac Ultraspheresy, E-Z-Trac Inc., Los Angeles, CA) were injected into the left ventricle of anesthetized mice before they were sacrificed after 2 min. Tumors were harvested, weighted, and microbeads were isolated and counted according to the manufacturer's instructions.

Luminol Bioluminescence Imaging

Mice with hindlimb tumors treated with thermal therapy with and without CYT-6091 injection (see Materials and Methods, Chapter 2) were imaged at Day 1, 3 and 7 after therapy using the Xenogen IVIS 200 imaging system (Caliper Life Sciences, Hopkinton, MA). Mice were anesthetized using ketamine/xylazine and injected i.p. with 100 μl of 50 mg/ml luminol (Gold Biotechnology, St. Louis, MO) solution 10 minutes prior to imaging (exposure time, 300 sec; binning, 4; FOV, 20 cm; f/stop, 1; no optical filter).

Histology and Immunohistochemistry

Animals were sacrificed 4 hours after CYT-6091 injection or at day 3 post DSFC cryosurgery immediately after vascular imaging. The entire tumor tissue attached to the

chamber was fixed in 10% buffered formalin (Sigma, St. Louis, MO), embedded in paraffin, and sectioned at 4 μm.

Silver staining: For visualizing nanoparticle accumulation within the tumor, deparaffinized sections were washed in DI water, 0.02 M sodium citrate (pH 3.5), and DI water in that order. Sections were silver enhanced using LI Silver® (Nanoprobes, Inc., Yaphank, NY) and counter stained with hematoxylin and eosin (H&E).

Myeloperoxidase (MPO) staining: Immunohistochemistry detecting MPO (1:2000; A0398, DAKO, Glostrup, Denmark) was performed on deparaffinized sections using the Rabbit on Rodent-HRP polymer kit (BioCare Medical, Concord, CA, USA) followed by 3,3'-Diaminobenzidine (DAB) chromagen staining. Tissue sections were counterstained with hematoxylin according to standard protocols and scanned using Aperio ScanScope (Axiovision Technologies, Toronta, Ontario, Canada) and analyzed using Aperio ImageScope software. On Day 3 post cryosurgery sections, digital annotation regions were applied around the zones of central necrosis and the inflammatory bands to quantify the respective areas on each section. The number of MPO positive cells in 5 representative regions within each histological zone was counted using light microscopy at 40X magnification.

Fibrin(ogen) staining: Immunohistochemistry detecting fibrinogen (1:2000; A0080, DAKO) was performed on deparaffinized sections using the Rabbit on Rodent-HRP

polymer kit (BioCare Medical) followed by 3,3'-Diaminobenzidine (DAB) chromagen staining. Sections were counterstained with hematoxylin according to standard protocols and scanned using Aperio ScanScope (Axiovision Technologies) and analyzed using Aperio ImageScope software. For quantification of fibrinogen staining intensity, digital annotation regions were applied in representative areas of each tumor section and pixels that exceeded threshold limits were quantified (as a % of total) using Color Deconvolution v9 algorithm (Aperio, Vista, CA).

Endothelial NFκB Activation and Microvessel Analysis: A new double staining protocol for identifying endothelial cells with NFκB activation in the nucleus was developed. Briefly, immunohistochemistry detecting endothelial cell marker CD31 (1:25, Clone: SZ31, Dianova, Hamburg, Germany) was performed on deparaffinized sections using Rat on Mouse AP-Polymer kit, BioCare Medical) followed by fast red staining (Vulcan Fast Red chromagen kit 2, BioCare Medical). Sections were rinsed in DI water and underwent denaturing treatment for 5 min using Denaturing Solution Kit (BioCare Medical). After this step, immunohistochemistry detecting NFκB p65 (1:5000, Gene Tex, Irvine, CA, USA) was performed using the Rabbit on Rodent-HRP polymer kit (BioCare Medical, Concord, CA, USA) followed by 3,3'-Diaminobenzidine (DAB) chromagen staining. Nuclei were counterstained with hematoxylin according to standard protocols and sections were scanned using Aperio ScanScope (Axiovision Technologies, Toronto, Ontario, Canada) and analyzed using Aperio ImageScope software. Digital annotation regions were applied in representative areas of each tumor section and pseudocolored

markup images depicting overlap of individual stains were generated using Color Deconvolution v9 algorithm (Aperio, Vista, CA). Black regions on the markup images indicated overlap of all three stains i.e. NFκB positive endothelial cell nuclei. The number of positive nuclei was counted using ImageJ (NIH) Colour Threshold and Analyze Particle macros. Microvessel analysis v1 algorithm (Aperio) was applied to the same annotation regions to count the number of vessels. Endothelial NFκB activation is reported as a ratio of the number of positive nuclei to the total number of vessels. The Microvessel analysis v1 algorithm was also used to generate histograms of the lumen area of the vessels to test differences between control and CYT-6091 treated DSFC tumors.

Statistics

Statistical significance was determined using the wilcoxon test in R statistical software [125]. If the difference was at the level of $p<0.05$, it was determined significant. Otherwise, the difference between two measurements was not significant, i.e., $p>0.05$. Data are represented as mean ± SE.

3.3. RESULTS AND DISCUSSION

Based on our previous work using native TNF as a preconditioning agent, a model was proposed (see Figure 1.4, Chapter 1) for the vascular and immunological mechanisms involved in nanoparticle preconditioning of tumors. The experiments reported in this chapter were designed to probe each aspect of the model and verify or extend our knowledge of the mechanisms of vascular and immunological preconditioning.

Tumor localization of CYT-6091

We first verified that intravenously injected gold nanoparticles were getting to the tumor tissues in vivo by examining histological sections of the tumor harvested 4 hrs after nanoparticle injection. CYT-6091 nanoparticles were visualized in tumor sections by silver enhancement which precipitates silver on gold nanoparticles to enable visualization by light microscopy. Tumor localization of CYT-6091 nanoparticles 4 hrs after i.v. injection was confirmed on H&E stained sections for DSFC (**Figure 3.1A**) and hindlimb (**Figure 3.1B**) LNCaP tumors. In both tumors at 4 hrs, nanoparticles were found in the vascular and perivascular regions with little or no extravasation into the interstitial space. CD31 IHC and silver enhancement of these tumors showed that the nanoparticles were in close proximity and interacting with the tumor endothelium (**Figure 3.1C**). Tumor sections analyzed at 24 hrs after CYT-6091 injection showed nanoparticles both in the perivascular region and extravasated out into the tumor interstitium. Localization of the nanoparticles to the tumor endothelium is expected as TNF present on CYT-6091

nanoparticles acts as a ligand for TNFR1 receptors present in abundance on tumor endothelial cells [134].

Effect of NP preconditioning on tumor endothelial NFκB activation

After verifying that CYT-6091 localized to the tumor, we tested the next step in the model which is endothelial NFκB activation. Previous work in our lab has implicated the TNF-α mediated NFκB inflammatory pathway as being essential for preconditioning of cryosurgery by topical administration of native TNF-α [66]. It was also shown that NFκB

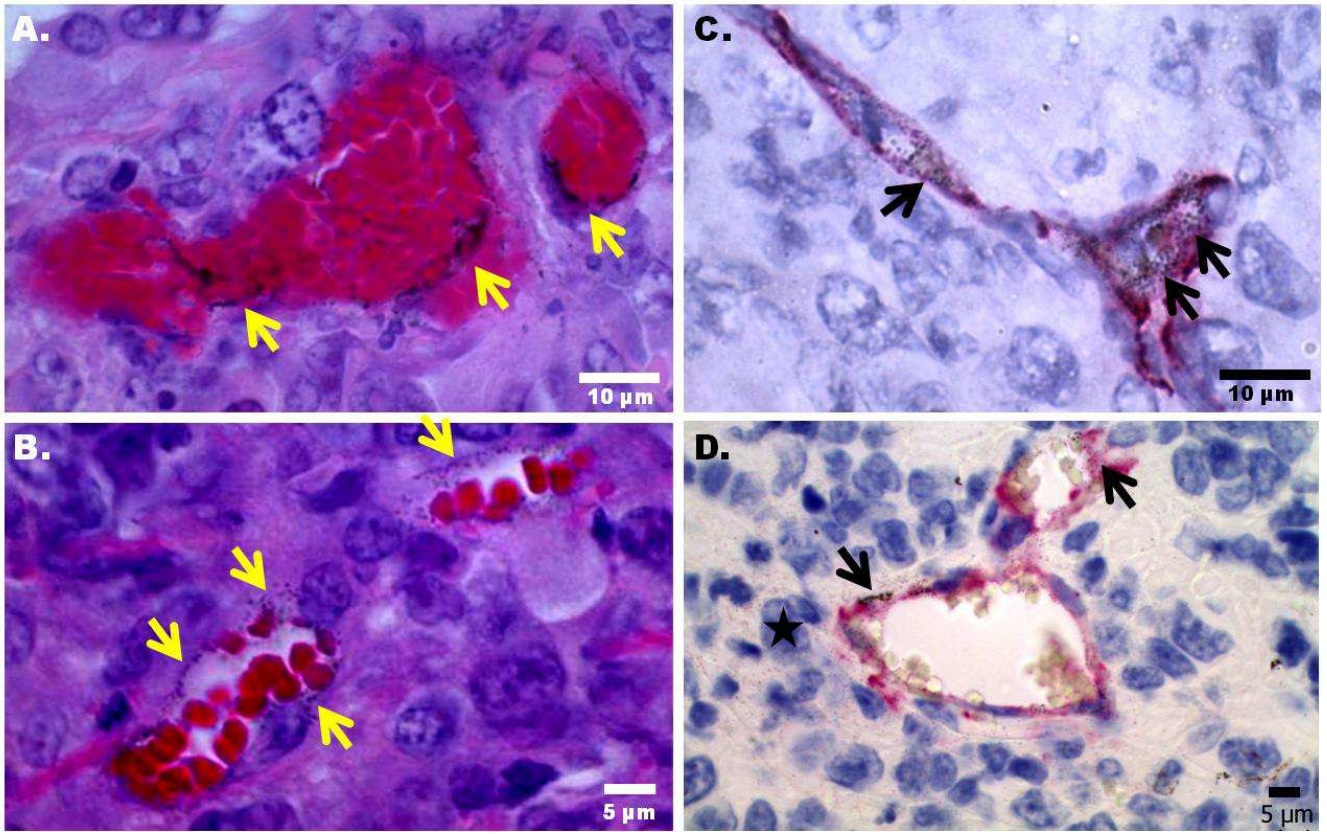

Figure 3.1. Localization of CYT-6091 nanoparticles around the vasculature of LNCaP tumors. A, B) H&E sections of DSFC (A) and hindlimb (B) 4 hrs after i.v. injection of CYT-6091. C, D) CD31 IHC sections of LNCaP tumors 4 hrs (C) and 24 hrs (D) after i.v. injection of CYT-6091. Black areas/specks on the sections indicated by arrows are silver precipitates on the gold nanoparticles. * indicates an area with extravasated nanoparticles seen as tiny black specks in the tumor interstitium.

activation was upregulated throughout the DSFC tumor tissue (i.e. tumor, endothelial and fibroblast cells) 4 hrs after topical administration of 200 ng of native TNF-α [91]. In this study, CYT-6091 nanoparticles were injected intravenously and showed negligible extravasation out of the tumor vasculature at 4 hrs indicating that the actions of TNF-α on the nanoparticle are mainly directed towards the tumor endothelium. Thus the number of NFκB positive endothelial nuclei per tumor vessel was compared between control and CYT-6091 treated tumors at 4 hrs. No difference was present in tumor endothelial NFκB activation between control (3.13 ± 0.14 positive nuclei/vessel) and CYT-6091 (3.07 ± 0.39) groups (**Figure 3.2**).

Molecular inhibition of NFκB and VCAM-1

To further understand the role of the NFκB pathway in NP preconditioning molecular inhibition studies of NFκB and VCAM-1 was carried out. Previous work in our lab has shown that molecular inhibition of the NFκB pathway using BAY 11-7085 reduces the enhancement of cryosurgical injury in DSFC LNCaP tumors by preadministration of 200 ng of topical TNF [66]. This led to the theory that the NFκB pathway is critical for the preconditioning response by TNF. We first sought to verify these findings by repeating the inhibition study using topical TNF. As expected, topical administration of 200 ng of TNF 4 hrs prior to cryosurgery significantly increased the vascular stasis area at Day 1 and 3 compared to cryosurgery alone (**Figure 3.3A**). BAY-11-7085 administration prior to TNF delivery reduced this enhancement of the cryosurgical injury response at Day 3 (**Figure 3.3A**). The vascular stasis area decreased from 53.3 ± 0.7 mm^2 with TNF

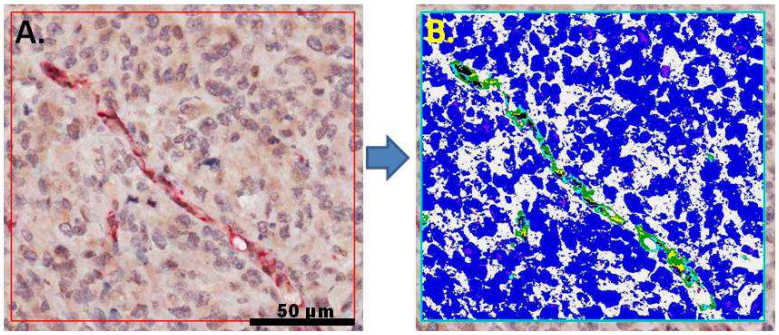

C.

Treatment	# positive nuclei per vessel
Control	3.07 ± 0.39
CYT-6091 4hrs	3.12 ± 0.14

Figure 3.2. Effect of NP preconditioning on tumor endothelial NFκB activation. DSFC LNCaP tumor tissues were costained using CD31 and NFκB p65 specific antibodies along with hematoxylin nuclear counterstaining. Sections were digitized and markup images (B) depicting overlap of stains were generated. Black regions in the markup image indicate NFκB positive endothelial nuclei which were compared between control and CYT-6091 treated tumors (C).

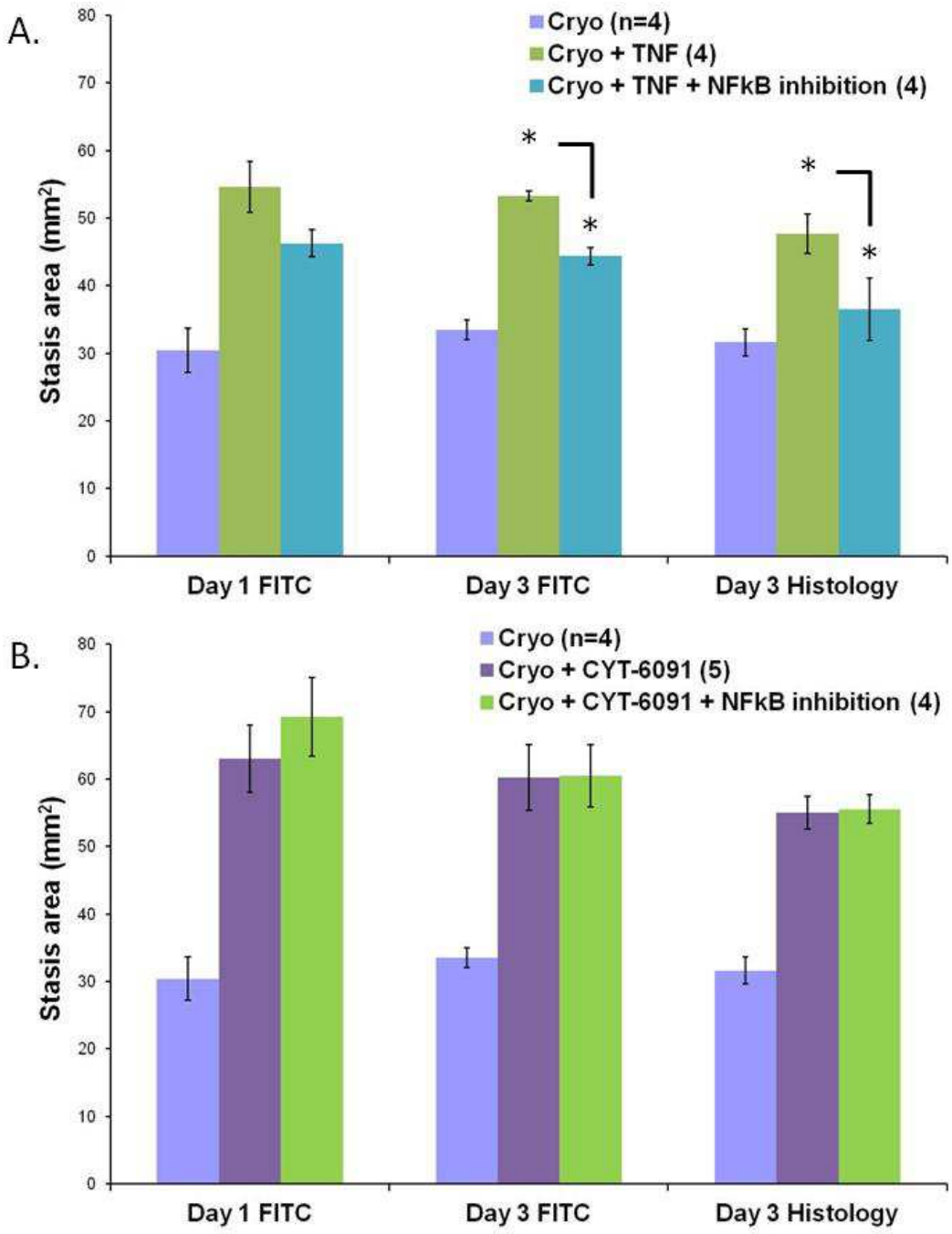

Figure 3.3. Molecular inhibition of NFκB activation. A) Inhibition of NFκB activation using BAY 11-7085 reduces the enhancement of cryosurgical injury by topical TNF delivery in DSFC LNCaP tumors. B) Inhibition of NFκB activation using BAY 11-7085 does not reduce NP preconditioning mediated enhancement of cryosurgical injury in DSFC LNCaP tumors.

preconditioning to 44.4 ± 1.3 mm^2 with NFκB inhibition ($p<0.05$). This decrease in vascular stasis area correlated with a decrease in the histological stasis areas from 47.7 ± 3.0 mm^2 with TNF preconditioning to 36.52 ± 5.0 mm^2 with NFκB inhibition ($p<0.05$).

Having verified that NFκB inhibition worked for native TNF, we sought to test whether NFκB inhibition would reduce nanoparticle TNF mediated enhancement of cryosurgical injury. Vascular stasis area of 60.3 ± 4.9 mm^2 was obtained with CYT-6091 preconditioning which was not significantly reduced by NFκB inhibition, 60.5 ± 4.6 mm^2 ($p>0.05$) (**Figure 3.3B**). This was confirmed by measuring the histological stasis area which correlated well with the vascular stasis area and also showed no significant attenuation of the cryosurgical injury due to NFκB inhibition (**Figure 3.3B**).

NFκB is a potent upregulator of inflammatory pathways and in particular leads to upregulation of cell adhesion molecules such as ICAM-1 and VCAM-1 that are important for recruitment of leukocytes [135]. Our lab has shown that antibody inhibition of VCAM-1 administered 4 hrs after topical TNF administration to DSFC LNCaP tumors reduces the enhancement of cryosurgical injury (Jiang et al., unpublished results). However, VCAM-1 inhibition failed to reduce nanoparticle preconditioning mediated enhancement of cryosurgical injury at Day 3 after therapy (**Figure 3.4**). Interestingly, the vascular stasis area obtained at Day 1 with VCAM-1 inhibition (40.9 ± 1.6 mm^2) was lower than the CYT-6091 group (60.3 ± 4.9 mm^2, $p<0.05$) indicating that although VCAM-1 inhibition delayed the development of the cryosurgical lesion it could

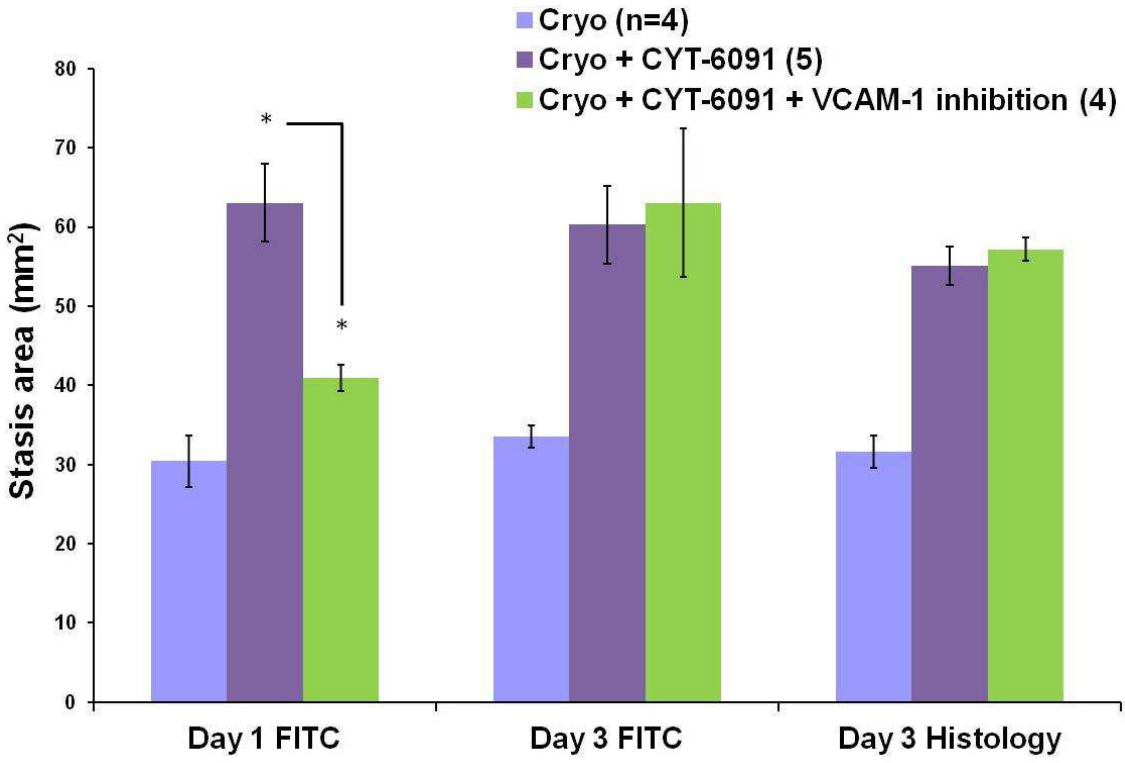

Figure 3.4. VCAM-1 antibody inhibition. Monoclonal antibody mediated inhibition of VCAM-1 does not reduce NP preconditioning mediated enhancement of cryosurgical injury in DSFC LNCaP tumors.

not reduce the maximum extent of injury obtained at Day 3. Taken together these results implicate a lesser role, if any, for NFκB activation pathway in NP preconditioning compared to preconditioning by topical delivery of native TNF.

NP preconditioning induced tumor vascular hyperpermeability

Farma et al have previously demonstrated that intravenously administered native TNF-α and CYT-6091 induces vascular hyperpermeability in vivo in a TNF-sensitive MC38 tumor cell line [83]. We sought to qualitatively verify these findings in our DSFC LNCaP tumor model. Tumor vasculature was monitored by fluorescence imaging using i.v. injection of 70kDa FITC-dextran between 1-2 hrs after systemic administration of CYT-6091 (5 µg TNF-α) and topical administration of 200 ng of native TNF-α separately. Both CYT-6091 and native TNF-α induced a robust vascular leak of FITC-dextran dye from the tumor vasculature (**Figure 3.5**). As expected, the intravascular fluorescence intensity of imaged tumor vessels diminished over time while extravascular fluorescence increased, causing the image to get blurry.

Effect of NP preconditioning on tumor vessel size

CD31 stained tumor sections showed dilated microvessels in the CYT-6091 treated group compared to control (**Figure 3.6A,B**). A microvessel analysis algorithm was used to

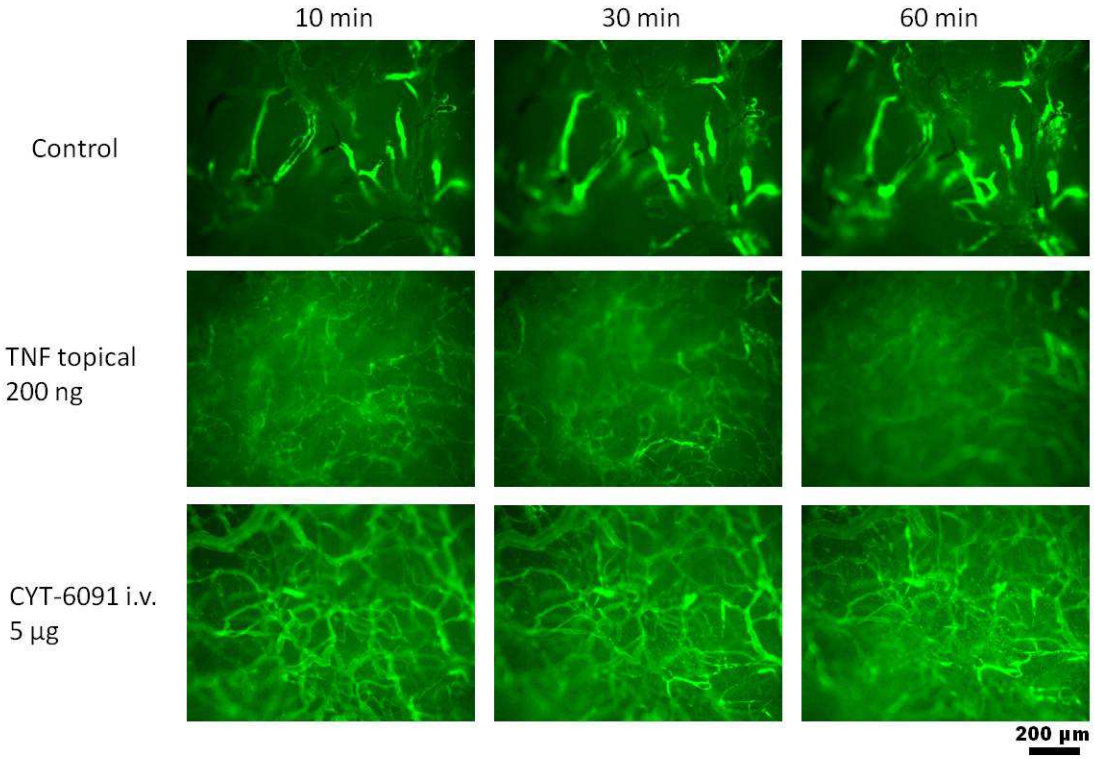

Figure 3.5. Effect of nanoparticle preconditioning on tumor vascular hyperpermeability. Topical and nanoparticle (CYT-6091) delivery of TNF-α induces vascular leak of macromolecules (70 kDa FITC-dextran) within 2 hrs of administration. FITC-dextran was intravenously injected 1 hr after TNF-α administration. 10, 30 and 60 minutes refer to time points after FITC-dextran injection.

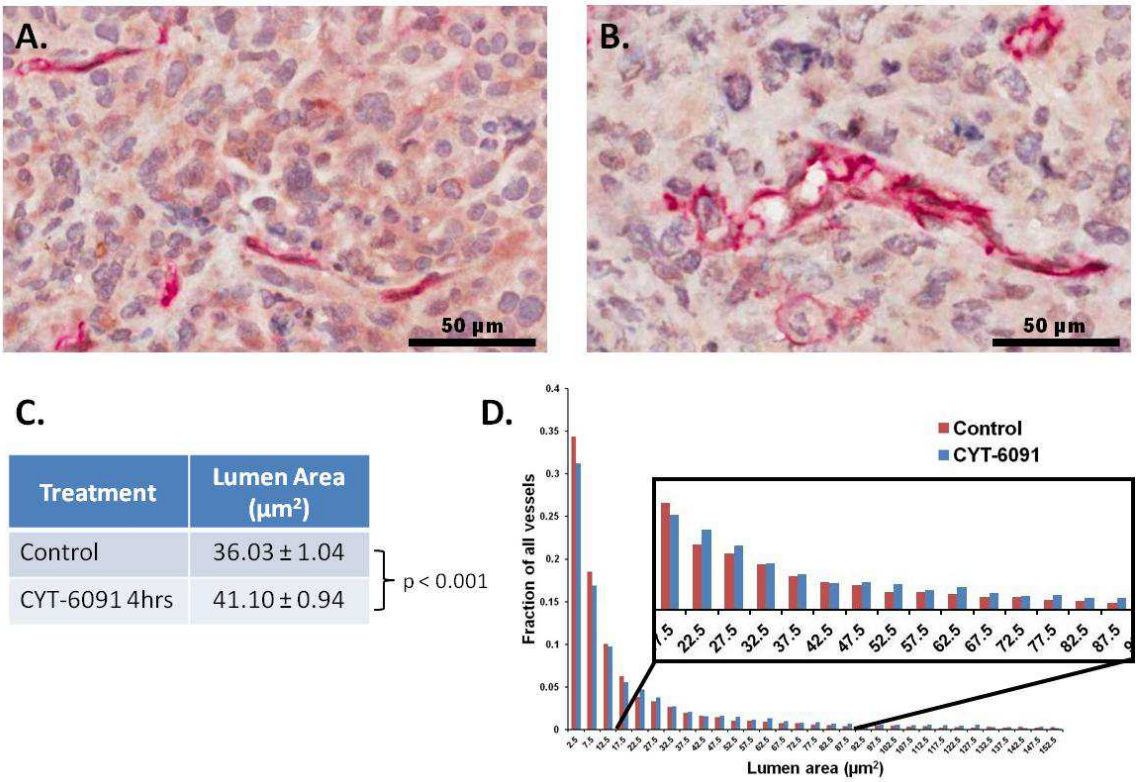

Figure 3.6. Effect of NP preconditioning on vessel size of DSFC LNCaP tumors. A) CD31/NFκB costained section of control tumor. B) CD31/NFκB costained section of CYT-6091 treated tumor. C) Summary of lumen areas obtained for control and CYT-6091 groups. D) Histogram of lumen areas binning fraction of all vessels analyzed in each group into 5 μm^2 intervals.

quantify the change in tumor vessel size 4 hrs after systemic administration of CYT-6091. Over 5000 vessels were analyzed in each group and a significant increase in vessel lumen area was obtained in the CYT-6091 group (41.10 ± 0.94 μm^2) compared to control (36.03 ± 0.94 μm^2, $p<0.001$) (**Figure 3.6C**). Histograms of the lumen areas generated for both groups showed a clear shift towards higher values for the CYT-6091 group (**Figure 3.6D**). These results are similar to previous results reported by our group i.e. TNF induces vasodilation of tumor blood vessels [118]. In that study Chao et al reported a 1.5-fold increase in the vessel diameter which would correspond to a 2.25-fold increase in the lumen area. However, in that study 0.2ng of native TNF was delivered topically on the DSFC tumor. Also their estimates were based on visual observation of changes in vessel diameter and not detailed histological analysis as was done in the present study.

NP preconditioning induced tumor perfusion drop and fibrin formation

Our lab has previously shown that CYT-6091 elicits an 80% drop in perfusion of SCK and FSaII tumors using a rubidium uptake method however until now we have not studied the effect of nanoparticle administration on LNCaP tumor perfusion [67, 68]. Tumor perfusion was studied by measuring microbead accumulation in hindlimb tumor tissue at specific time points after nanoparticle administration (**Figure 3.7**). 4 hours after injection of CYT-6091 (5 µg TNF-α), tumor perfusion dropped to 19.8 ± 8.2% of controls ($p = 0.002$). This drop in perfusion persisted up to 6 hrs (16.1 ± 6.1%) after nanoparticle injection. Increasing the dose of CYT-6091 to 10 µg TNF-α, did not drop tumor perfusion further at 6 hrs (19.9 ± 6.6%). Interestingly, AuPEG also dropped tumor

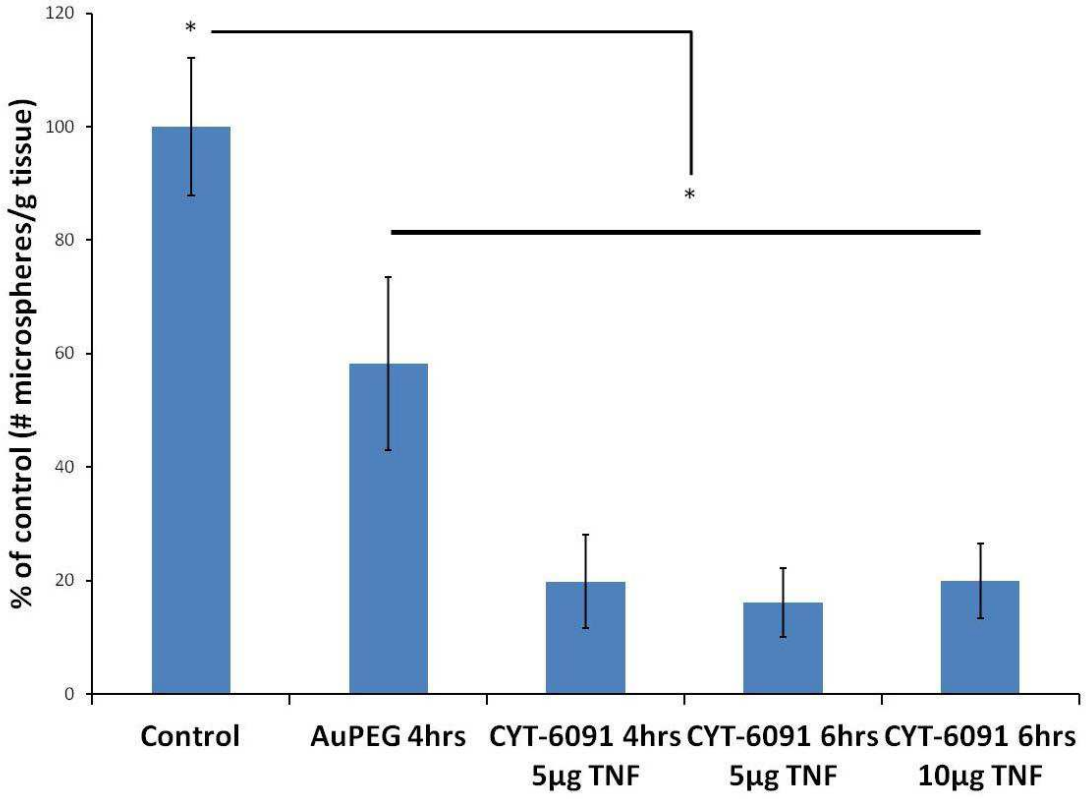

Figure 3.7. Effect of nanoparticle preconditioning on hindlimb LNCaP tumor perfusion. Data presented as mean ± SE. (* indicates that values of all groups are statistically lower than control, $p < 0.05$)

perfusion to 58.2 ± 15.3% 4 hrs after injection ($p = 0.01$). The perfusion drop induced by CYT-6091 at 4 hrs was accompanied by enhanced fibrinogen staining in DSFC tumors (**Figure 3.8**). Numerous regions of petechial hemorrhage were also present in CYT-6091 treated tumor sections. These results are in agreement with regions of complete vascular stasis observed within DSFC LNCaP tumors at 4 hrs after CYT-6091 administration (data not shown).

Role of neutrophils in NP preconditioning

The role of inflammatory cells especially neutrophils in determining the maximum extent of the cryosurgical lesion is well documented [136]. However the functional role of neutrophils in NP preconditioning is still unclear. Previous data from our lab showed an increased recruitment of inflammatory infiltrate into DSFC LNCaP tumors 4 hrs after topical administration of 200 ng native TNF [91]. This was accompanied by significantly higher recruitment of neutrophils in the inflammatory zone of the Day 3 cryolesion with TNF preconditioning compared to cryosurgery alone [91]. We hypothesized that increased recruitment of neutrophils is essential for the enhanced cryosurgical lesion due to NP preconditioning.

We first investigated the recruitment of neutrophils to DSFC LNCaP tumor tissue during the 4 hour period after CYT-6091 administration by myeloperoxidase staining. The number of neutrophils (average count of MPO positive cells in 5 random high power fields in at least 4 tumor samples), present in tumor tissues was small and no significant

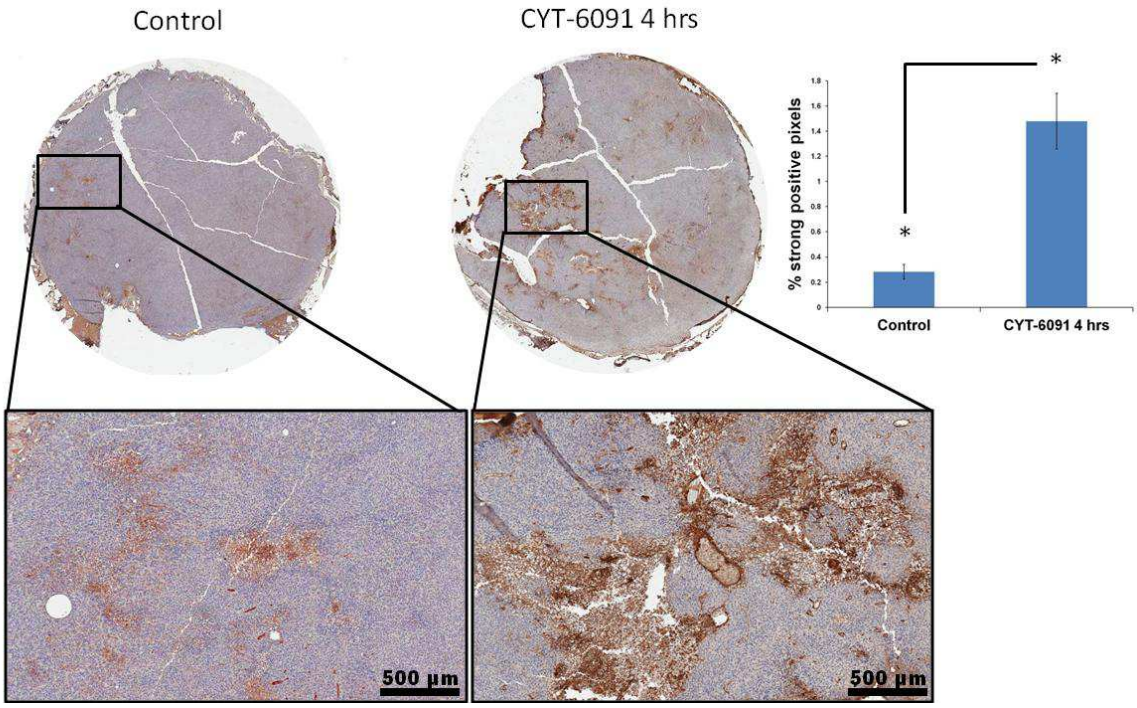

Figure 3.8. Effect of nanoparticle preconditioning on fibrin(ogen) deposition in DSFC LNCaP tumors. Fibrinogen stained sections of DSFC LNCaP tumors with and without CYT-6091 preadministration are shown. Data presented as mean ± SE. (*, $p < 0.05$)

differences were observed between neutrophil numbers in control tumors (0.60 ± 0.35) or tumors injected with AuPEG (1.50 ± 0.41) or CYT-6091 (1.10 ± 0.26) for 4 hrs (**Figure 3.9**).

Next, we tested the functional role for neutrophils in NP preconditioning by systemic depletion of neutrophils prior to CYT-6091 injection and cryosurgery. Systemic depletion of circulating neutrophil numbers by i.p. injection of anti-Ly6G (RB6-8C5) antibody was confirmed (**Figure 3.10**). Neutrophil counts in mouse blood decreased to 11.2 ± 3.5% of baseline values 24 hrs after antibody injection. Neutrophil counts recovered to baseline values within 4 days of antibody injection (**Figure 3.10**). To test the role of neutrophils in NP preconditioning, RB6-8C5 antibody was administered 24 hrs prior to CYT-6091 injection to deplete circulating neutrophil numbers prior to NP preconditioning. Cryosurgery was performed in neutrophil-depleted mice 4 hrs after CYT-6091 injection. Systemic neutrophil depletion did not reduce nanoparticle preconditioning mediated enhancement of cryosurgical injury at Day 1 or Day 3 after therapy (**Figure 3.11**). Vascular stasis area of 60.3 ± 4.9 mm^2 was obtained with CYT-6091 preconditioning which was not significantly decreased by neutrophil depletion, 60.2 ± 2.6 mm^2 ($p>0.05$) (**Figure 3.11**). This was confirmed by measuring the histological stasis area which correlated well with the vascular stasis area and also showed no significant attenuation of the cryosurgical injury due to neutrophil depletion (**Figure 3.11**).

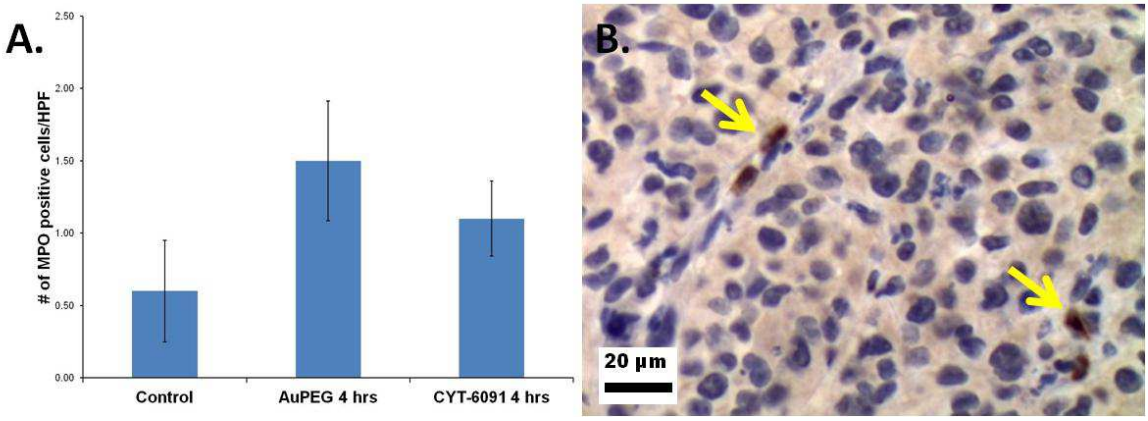

Figure 3.9. Neutrophil recruitment during NP preconditioning. A) High field power count of myeloperoxidase (MPO) positive cells i.e. neutrophils during NP preconditioning. B) Representative image of DSFC LNCaP tumor containing MPO positive cells.

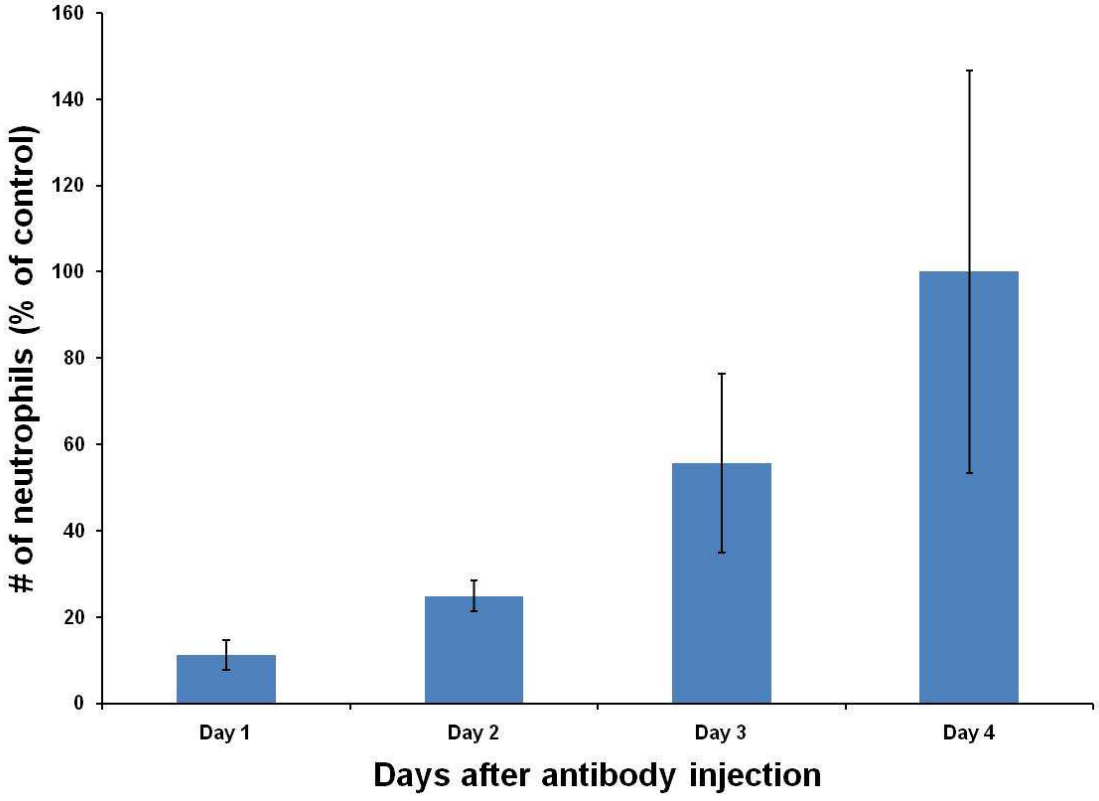

Figure 3.10. Anti-Ly6G Ab depletes circulating neutrophils in vivo. 150 µg of RB6-8C5 Ab was injected i.p. into nude mice and serial blood draws from facial vein was done over 4 days and circulating neutrophil number obtained using an automated blood cell counter.

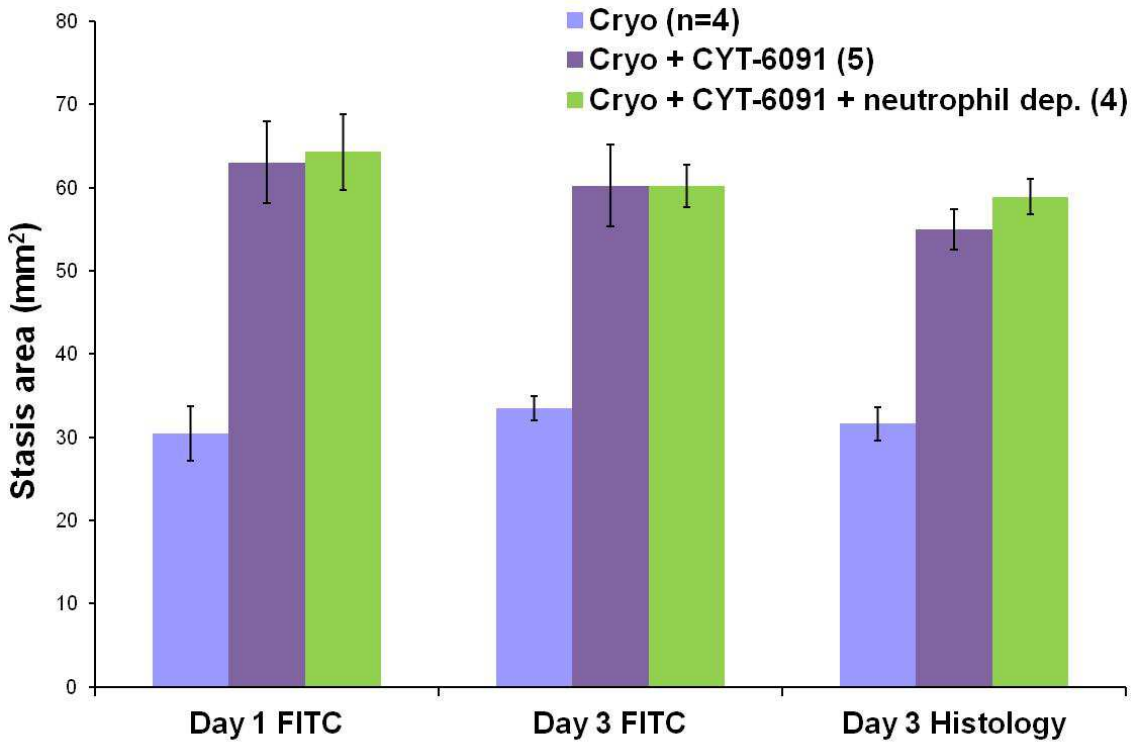

Figure 3.11. Neutrophil depletion does not reduce NP preconditioning mediated enhancement of cryosurgical injury.

Lastly, we analyzed neutrophil recruitment in the cryosurgical lesion at Day 3 following DSFC LNCaP tumor cryosurgery. The following groups were compared: a) Cryo only (cryosurgery alone), b) Cryo + CYT-6091 (CYT-6091,5 µg TNF, i.v. injection 4 hrs prior to cryosurgery), c) Cryo + CYT-6091 + Neutrophil depletion (systemic neutrophil depletion 24 hrs before CYT-6091,5 µg TNF, i.v. injection followed 4 hrs later by cryosurgery), and d) Cryo + TNF (TNF,200 ng µg TNF, topical administration 4 hrs prior to cryosurgery). Representative cross sections of the Day 3 lesions are presented in **Figure 3.12** with the corresponding neutrophil counts in **Figure 3.13**. The cryo only lesion showed the characteristic histologic zones associated with cryosurgical injury i.e. a central necrotic zone adjacent and concentric to the cryoprobe tract surrounded by a band of inflammatory infiltrate, zone of thrombosis/ischemic necrosis and viable tumor tissue. The cryo + CYT-6091 lesion was markedly different with a large central necrotic zone surrounded by a thin band of inflammatory infiltrate and viable tumor tissue. The number of neutrophils present in the inflammatory band was not different in the cryo + CYT-6091 group (15020 ± 5964) compared to the cryo only group (39651 ± 10371). In the cryo + CYT-6091 + neutrophil depletion group a similar trend was seen with a larger central necrotic zone surrounding the cryoprobe tract and a thin inflammatory band on the boundary of the viable tumor tissue. The cryo + TNF group had a central necrotic zone larger than the cryo only group but smaller than the CYT-6091 treated groups. This group had a broad dense inflammatory band with a large number of neutrophils that was substantially higher than the other three groups (**Figure 3.13**). To summarize, we obtained a larger central necrotic zone in the CYT-6091 treated

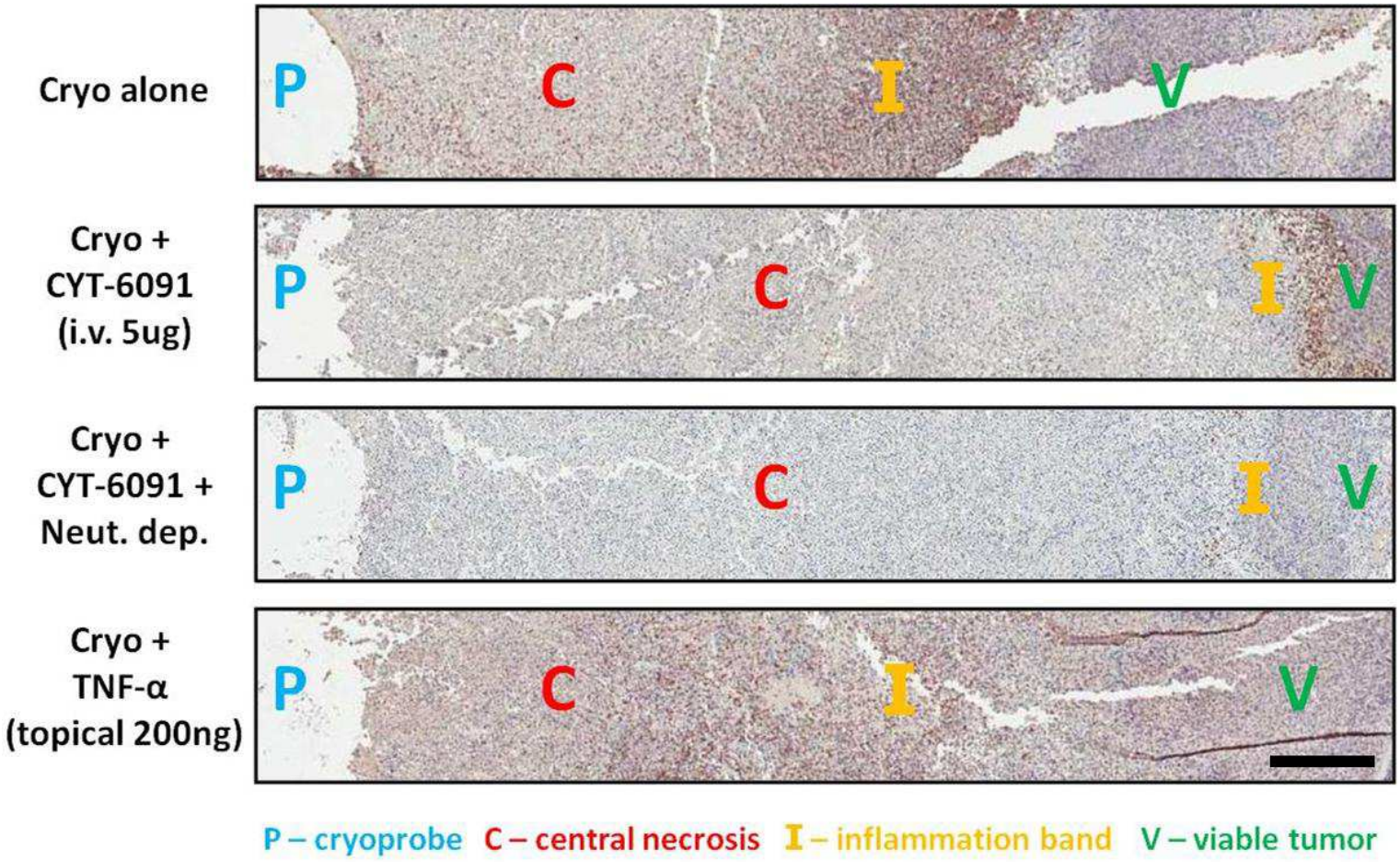

Figure 3.12. Neutrophil recruitment in the cryosurgical lesion at Day 3 following DSFC LNCaP tumor cryosurgery. Representative MPO stained sections are shown for each group. (Scale bar = 500 µm)

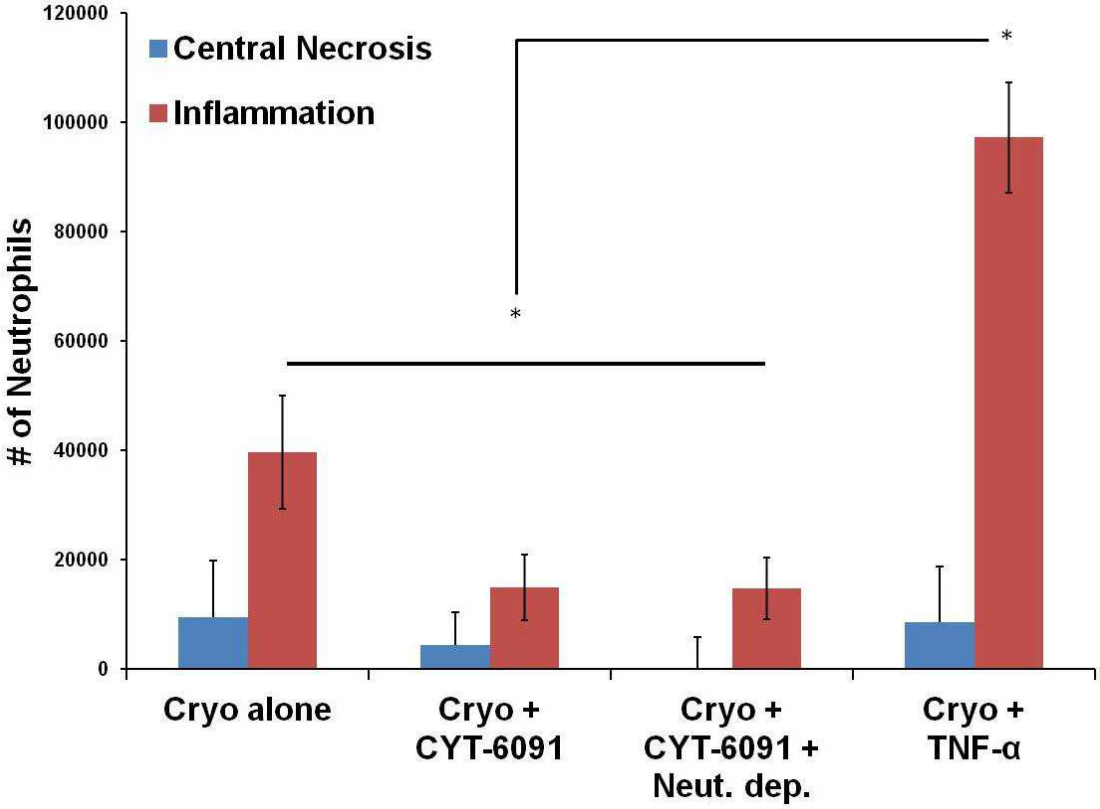

Figure 3.13. Neutrophil counts in histological zones of the cryosurgical lesion at Day 3 following DSFC LNCaP tumor cryosurgery. (*, $p<0.05$)

group with a low number of neutrophils compared to a slightly smaller central necrotic zone in the topical TNF treated group but with a large number of neutrophils.

Non-invasive luminol bioluminescence imaging of neutrophil recruitment following thermal therapy in hindlimb LNCaP tumors

Based on our previous preconditioning work with topical TNF preconditioning yielding a dense inflammatory infiltrate at day 3, we hypothesized that any increase in the inflammatory infiltrate brought about by NP preconditioning can be non-invasively monitored and quantified by luminol bioluminescence imaging [91, 112]. Luminol is a redox-sensitive compound that upon systemic administration reacts specifically with myeloperoxidase to emit blue luminescence [112]. We sought to utilize this feature of luminol to non-invasively image neutrophil infiltration into the thermal lesion. Following hindlimb LNCaP tumor cryosurgery or high-temperature thermal therapy with or without nanoparticle preconditioning, mice were injected with luminol on Day 1, 3 and 7 following therapy and the bioluminescence emitted from the tumor region was imaged and quantified (**Figure 3.14**). Although a bioluminescent signal was present and easily imaged, no clear statistically significant trends are exhibited in either cryosurgery or HTT groups. Taken together with the previous set of experiments, the role of neutrophils in NP preconditioning seems to be limited.

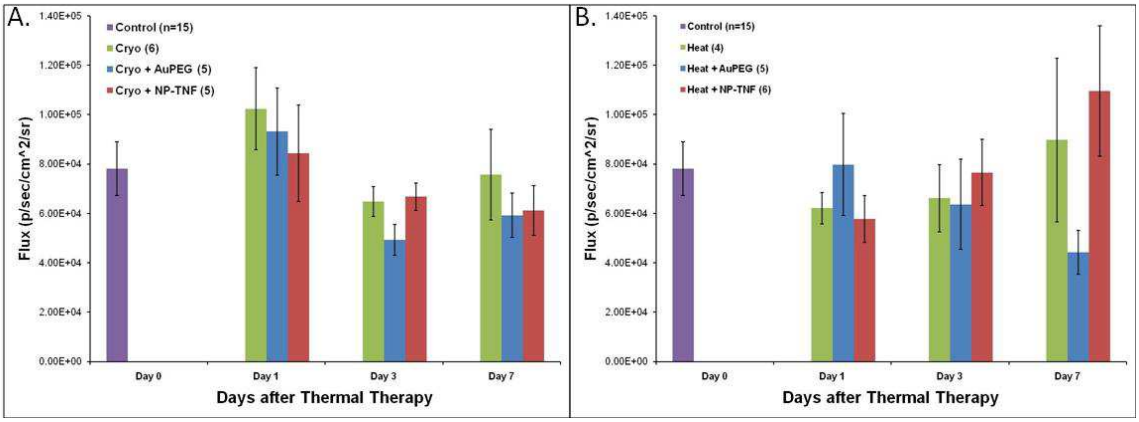

Figure 3.14. Luminol bioluminescence imaging of hindlimb LNCaP tumors post cryosurgery (A) or high-temperature thermal therapy (B) with and without nanoparticle preconditioning.

3.4. CONCLUSIONS

The model for NP preconditioning proposed originally (see Figure 1.4, Chapter1) was changed based on the experimental results obtained in this chapter (**Figure 3.15**). One major change was that the endothelial event leading to downstream changes in tumor vascular permeability and perfusion is not endothelial activation of NFκB. The lack of difference in number of NFκB positive nuclei together with the results of the molecular inhibition studies of NFκB and VCAM-1 support this claim. In addition, the role of neutrophils seems to be non-essential for NP preconditioning indicating that vascular events dominate the preconditioning mechanism. The induction of vascular hyperpermeability in tumor tissue has significant implications in clinical imaging and combination therapy with chemotherapeutics as discussed later. The dramatic 80% drop in perfusion seen in other tumor models was demonstrated between 4-6 hrs after CYT-6091 injection in LNCaP tumors as well. The differences seen in the preconditioning responses of native TNF and CYT-6091 to molecular inhibition studies and neutrophil recruitment is likely due to the differences in delivery method (topical vs i.v.) and effective dose interacting with the tumor tissue. 200 ng of native TNF administered topically yields a much higher effective dose of TNF when compared to 5 µg of nanoparticle bound TNF delivered systemically. Also, topical delivery of native TNF leads to direct exposure of tumor cells to a high dose of exogenous TNF which could make them more susceptible to a secondary challenge i.e. thermal therapy.

Summary of NP preconditioning events

a.	NP tumor localization:	around tumor vasculature
b.	Endothelial NFκB activation:	not significant @ 4 hrs
c.	Leukocyte recruitment:	not significant @ 4 hrs
d.	Microvascular changes:	increased lumen area @ 4 hrs
e.	Vascular hyperpermeability:	increased @ 1-2 hrs
f.	Tumor perfusion:	significant (80%) drop @ 4-6 hrs
g.	Fibrin deposition:	increased @ 4 hrs

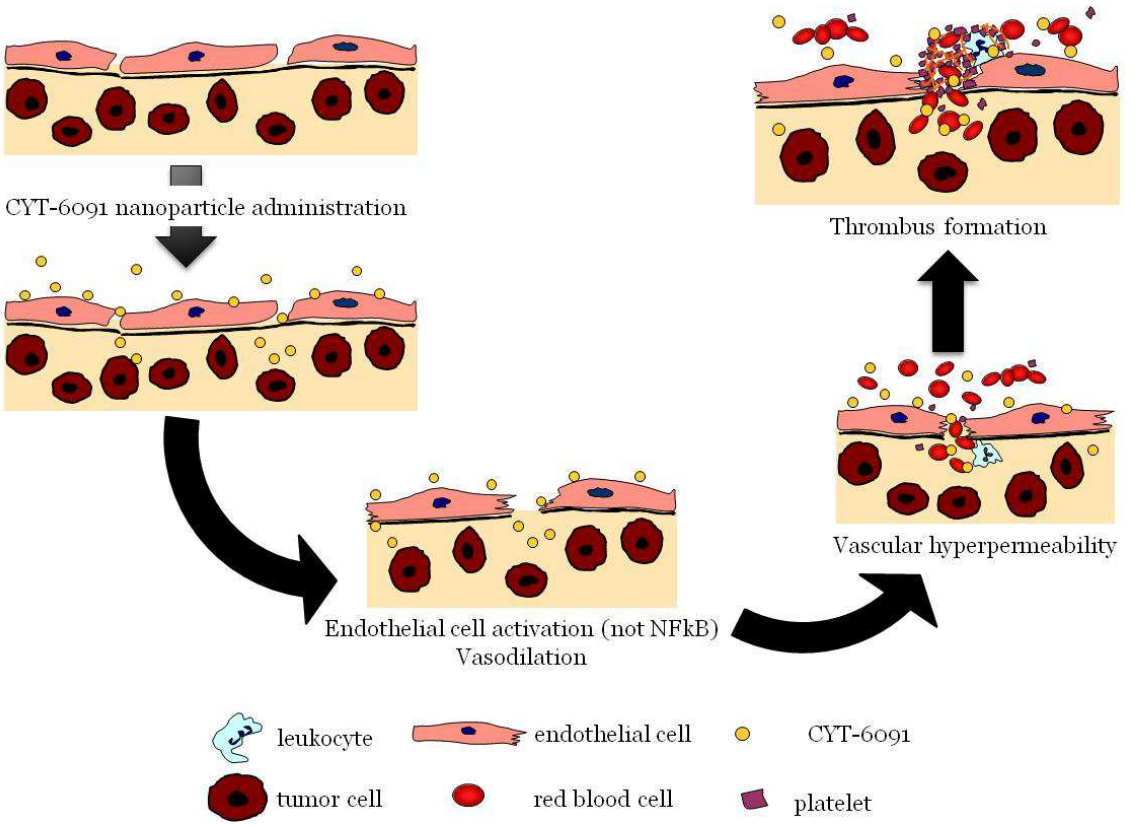

Figure 3.15. Revised Mechanism of Preconditioning with TNF-α Tagged Gold Nanoparticles.

Chapter 4: Use of Tumor Necrosis Factor–alpha-coated Gold Nanoparticles to Enhance Radiofrequency Ablation in a Translational Model of Renal Tumors

This chapter describes the first use of nanoparticle preconditioning to enhance thermal therapy (radiofrequency ablation) in a translational tumor model. This chapter was published in the following citation. The article is reproduced with permission from Elsevier:

- Pedro RN, Thekke-Adiyat K, Goel R, Shenoi M, Slaton J, Schmechel S, Bischof J, Anderson JK. Use of tumor necrosis factor-alpha-coated gold nanoparticles to enhance radiofrequency ablation in a translational model of renal tumors. Urology. 2010 Aug;76(2):494-8.

4.1. INTRODUCTION

The treatment of renal cell carcinoma (RCC) has progressed rapidly from the use of radical nephrectomy as the sole surgical treatment option to the increasing use of thermal ablative technologies, such as radiofrequency ablation (RFA) today. However, the use of nephron-sparing surgical treatment options has remained limited [137]. Ablative treatments such as RFA offer a minimally invasive and technically simple therapeutic option for small renal tumors. However, the number of tumors amenable to ablative therapies is limited because of restrictions on tumor size, relation to renal hilar structures, and tumor proximity to adjoining vital organs [138].

Studies of high temperature thermal lesions have demonstrated that there are specific zones of cell injury as distance from the thermal probe increases [139, 140]. The inner zone (closer to the RFA probe) experiences the highest temperatures and comprises complete cell death. Coagulative necrosis is the landmark of this area. Next is a noticeable rim of thrombosis and vascular congestion. Grossly, a red halo is easily seen surrounding the margins of the inner paleo-area of necrosis. External to this line of thrombosis, there is another layer of edema, inflammation, and partial cell injury amid viable cells. This is the incomplete kill zone, where there is a mixture of viable and nonviable cells. Beyond this zone, cellular viability remains intact.

To adequately treat a renal lesion with RFA, it is necessary to push the region of total cell death beyond the margin of the tumor. Unfortunately, the heat-induced injury within the incomplete kill zone extends even farther. Patient selection for percutaneous RFA becomes very important to limit damage to nearby vital organs, such as intestine, because heat-induced injury must extend well beyond the tumor edge. Previous efforts using liposomal doxorubicin attempted to increase the size of the complete cell death zone, but this technique has had limited clinical application [141].

The possible solutions for augmenting thermal injury without increasing the energy deposition are to reduce tumor blood flow before heating and to increase the thermal sensitivity of the tumor and the tumor endothelium. Tumor necrosis factor–α (TNF-α) is of particular interest because it can affect both the cell and vasculature of the tumor with high potency. Unfortunately, systemic administration of TNF has dose-limiting toxicity; therefore, there is a need for selective tumor delivery of TNF to minimize systemic toxicity. Recently, gold nanoparticle-TNF-α — a delivery system capable of escaping phagocytic clearance by the reticuloendothelial system — has been investigated [74]. It showed that the gold nanoparticles preferentially extravasated the tumor vasculature to accumulate TNF within the tumor interstitium while concomitantly reducing the accumulation of TNF in healthy organs that maintain greater control of vascular permeability, consequently limiting the systemic toxic effects [74].

Based on the aforementioned premise, our goal was to investigate TNF-α–coated gold nanoparticles in a rabbit animal model as a novel molecular adjuvant to enhance RFA in the kidney. Our hypothesis was that use of this novel nanoparticle would minimize the size of the incomplete kill zone and thus maximize the volume of complete cell death.

4.2. MATERIALS AND METHODS

VX2 Carcinoma: Tumor Implantation

After we received approval from our Institutional Animal Care and Use Committee was obtained, New Zealand female rabbits weighing 2.2-2.7 kg were implanted with VX2 tumor in the hind limb or kidney. The animals were first anesthetized with an intramuscular injection of a solution containing ketamine (40 mg/kg), xylazine (5 mg/kg), and acepromazine (1 mg/kg), and they were then intubated and maintained on anesthesia for the surgical procedure by administering 0.75% isoflurane with 1 L/min of oxygen. Standard perioperative monitoring was performed. Because the VX2 tumors cannot be propagated in vitro using standard cell culture methods, the tumors were expanded in a subgroup of our animal model. This was done in vivo in the hind limb of our animal model by implanting a 1-mm3 tumor fragment under the fascia of the hind limb musculature. Tumors were harvested 2-3 weeks after implantation when a grossly visible and palpable mass of not, vert, similar3-cm diameter was obtained. The animal was then sacrificed and harvested tumors were sliced into 1-mm3 fragments, frozen, and stored in

sterile conditions within 1 mL of phosphate-buffered saline solution at −70°C for future use. For tumor implantation in the kidneys, a midline abdominal incision was made and both kidneys were exposed. A 1-mm3 piece of VX2 tumor was then implanted in the subcapsular region of the lower pole of the right kidney to prevent liver adhesions and the upper pole of the left kidney.

Radiofrequency Ablation

To achieve an optimal size of the tumor for ablation, a pilot study of 10 animals (20 kidneys) were implanted with VX2 tumors, and the diameter of the tumor on the cortical surface was measured using digital calipers at various time points after implantation. Radiofrequency ablation was performed after induction and maintenance of anesthesia as described before. The midline abdominal incision was reentered and the renal tumor mass was isolated from the surrounding organs and tissues. A modified 4-tine RF electrode (Starburst SDE, Rita Medical Systems, Mountain View, CA) and standard generator (1500× generator Rita Medical Systems) were used. The only modification to the electrode was to cut the central fixed tine 4 mm from its base. The target temperature, ablation time, and length of the probe tines were the 3 variables of the RFA system that could be adjusted to attain a desired ablation area. Care was taken to insert the probe into the tumor mass perpendicular to the cortical surface of the tumor. Our goal was to create a thermal injury zone that was contained within the tumor. This was achieved with the following settings: target temperature of 60°C, treatment time of 2 minutes, and tine deployment of 7 mm. The size and morphology of the ablation area with these settings

were consistently reproduced in multiple trials and used in the final treatment groups described next. Data from this pilot group was used solely to determine optimal RFA settings and timing of optimal tumor growth.

Nanoparticle Description

CYT-6091 (CytImmune Sciences, Rockville, MD) is a multivalent drug consisting of a nanoparticle of colloidal gold bonded to not, vert, similar400 TNF-a molecules and thiol-derivatized polyethylene glycol (PEG). The gold core of the nanoparticle is 30 nm, whereas the PEG brush layer extends another 10 nm from the surface and assists the particle in avoiding the reticuloendothelial system (RES), thereby passively accumulating in the leaky tumor microvasculature and allowing active binding of the TNF-a with tumor cells [74, 79].

Treatment Groups

RFA only

Ten kidneys with VX2 tumor were treated with RFA 10-14 days after the implant (see result on optimal tumor growth). The settings used for the ablation were 60°C target temperature for 2 minutes and tine deployment of 7 mm, for the reasons mentioned before. The tumors were easily located after exposure of the kidneys and the RFA probe was inserted into the center of the visible tumor mass on the surface of the kidney.

Nano only

Ten kidneys with VX2 tumor were treated only with CYT-6091 10-14 days after the implant. The drug was administered intravenously 4 hours before the surgical procedure at a dose of 200 μg/kg. This dose has previously been shown to enhance thermal therapies in various preclinical tumor models [67, 68, 84]. The surgical procedure comprised only dissection and exposure of the kidney and visualization of the tumor mass, without any invasive manipulation.

RFA plus Nano

Ten kidneys with VX2 tumor were treated with RFA in addition to CYT-6091 10-14 days after the implant. The drug was administered intravenously 4 hours before the surgical procedure at a dose of 200 μg/kg. The surgical procedure comprised kidney dissection and tumor identification. RFA was performed as described previously.

Sham

Seven kidneys with VX2 tumor were used in the sham group. These animals did not receive either RFA treatment or CYT-6091. The same surgical steps were performed in these animals as for the aforementioned groups. VX2 tumor was implanted into the kidneys and allowed to grow for 10-14 days. The sham procedure comprised only dissection and broad exposure of the kidney and visualization of the tumor mass, without any invasive manipulation.

Postablation Monitoring and Postsacrifice Analysis

From the injection of CYT-6091 through the perioperative period after the RFA procedure, the blood pressure, oxygen saturation, and temperature were monitored. Subsequently, the rabbits were checked daily for signs of malaise, poor appetite, low activity level, respiratory difficulty, or other signs of systemic illness. Postoperative monitoring was done with the intent of identifying side effects caused by CYT-6091. Necropsy was performed 4 days after the procedure. Using the initial pilot study rabbits, an initial histologic analysis was done at various time points ranging from 1-7 days to determine the optimal time after ablation for histologic analysis. At 4 days post ablation, the different zones of cell injury could be identified easily within the treatment area on hematoxylin and eosin (H&E) staining. A single pathologist with significant experience in thermal injury histology reviewed all slides and was blinded to the treatment groups.

The kidneys were harvested, immediately bivalved, and cut into 3-mm-thick slices perpendicular to the probe track. The tissue sections underwent overnight formalin fixation and standard histologic processing with H&E staining. The slides were scanned at a magnification of 20× using an Aperio scan scope CS scanner (Aperio Technologies, Vista, CA). The zones of complete cell death and total thermal injury (zone of complete cell death plus zone of incomplete cell death) were measured from the center of probe tract using the scanned images. The zone of complete cell death was measured from the center of the probe to the first viable cell (**Figure 4.1**). The zone of thermal injury was measured from the probe center to the last dead cell. The zone of incomplete cell death

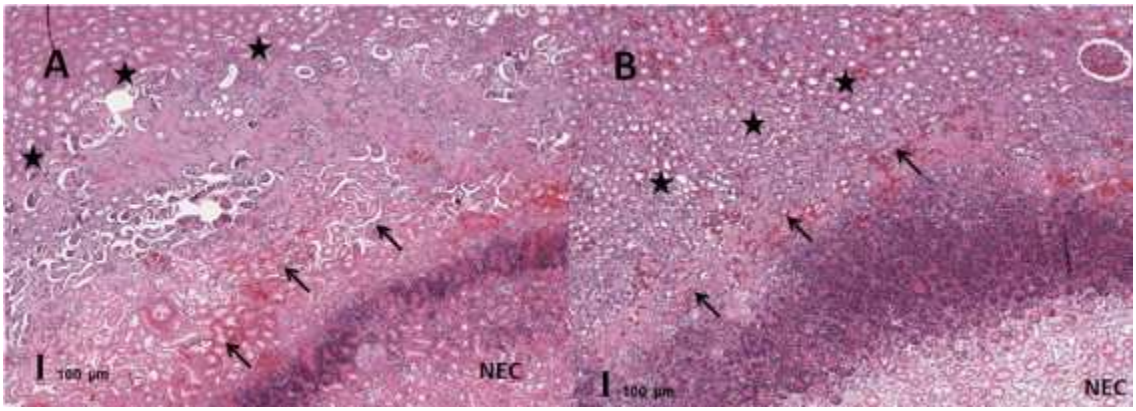

Figure 4.1. Microscopic findings: tips of arrows show the area corresponding to the beginning of the hemorrhagic rim and the end of the complete cell death zone. The stars mark the end of the thermal injury. The central necrotic area is demarked as Nec. The difference in the diameter of the zone of incomplete cell death (zone between the arrows and stars) is noticeably different between (A) RFA only and (B) RFA plus CYT-6091. Scale Bar as shown.

was defined as the area between the margins of these 2 zones. The measurements were performed using Aperio Image scope software (v. 9.0.19.1516). Tumor volumes were estimated with the equation of an ellipsoid volume = length × width × height × 0.52 [142]. The different thermal injury zone volumes were calculated for each 3-mm histologic slice cut from the tumor specimen. The volume for each zone for each 3-mm slice was then summed to achieve the total volume for that respective zone. Values are reported with 95% confidence intervals. Two-tailed Student's t-test was conducted to determine statistical significance between different groups; $P < .05$ was considered significant.

4.3. RESULTS

Assessment of the Ideal Tumor Size for RFA

The ideal tumor for testing the enhancement effect of CYT-6091 would be a firm, intact, solid mass contained within the renal capsule of the largest diameter possible, without gross evidence of necrosis or distant metastases. Between days 10-14 after implantation, the tumors reached 5-10 mm in diameter (average 7.4 ± 0.8 mm). After day 20 of tumor implantation, the tumor growth appeared exponential, eventually attaining diameters of 20-30 mm, frequently with peritoneal carcinomatosis and grossly visible tumor necrosis. Hence, the day 14 time point after implantation was chosen for administration of treatments in the various groups.

Macroscopic Findings

Four days after the treatments, the kidneys treated with RFA with or without CYT-6091 preadministration had ellipse-shaped ablation areas that on sectioning revealed concentric lesions extending from the capsule to the renal medulla. The following components could be identified on the gross cross section of the ablation area: (A) a large central pale-area surrounded by (B) a dark red rim, and (C) another pale-outer layer (**Figure 4.2**). No such lesions were evident in the sham or Nano-only groups. Nevertheless, tumor growth was altered by the administration of the nanoparticle. The average volume of the tumor mass in the sham group was 0.80 ± 0.14 cm^3, whereas the Nano-only group presented a tumor volume of 0.54 ± 0.37 cm^3 ($P = .038$) on necropsy 4 days after treatment.

Microscopic Findings

Distinct histologic regions of the thermal lesion were evident on H&E-stained sections of the RFA-treated kidneys. These regions occurred concentric to the location of the RFA probe tract and were similar in shape and size to the macroscopically observed discolored lesions. The region immediately adjacent to the probe tract was comprised mostly of cell debris with complete absence of viable tubular or tumor cells. Few scattered inflammatory cells were also present in this region. This zone was characteristic of coagulative necrosis and labeled the complete cell death zone. The volume of this zone in the RFA + Nano group was significantly greater than the RFA-only group (0.30 ± 0.07 vs 0.23 ± 0.03 cm^3, $P = .03$) (**Figure 4.3**). This corresponds to a 23.3% increase in volume of the complete cell death zone in the RFA + Nano group.

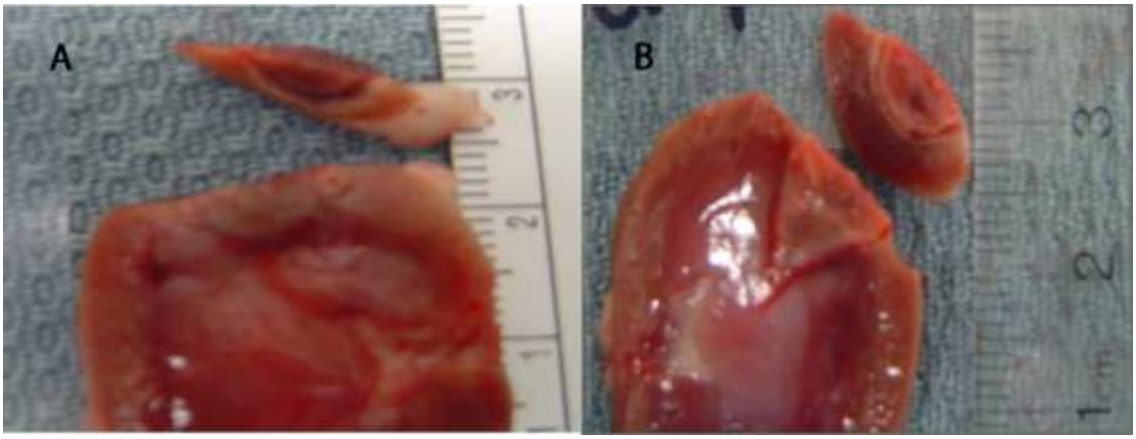

Figure 4.2. Macroscopic findings. (A) With RFA alone the hemorrhagic rim is embraced by a wide white external layer, both surrounding a central necrotic area. (B) With RFA plus CYT-6091 the external layers are narrower and more easily defined.

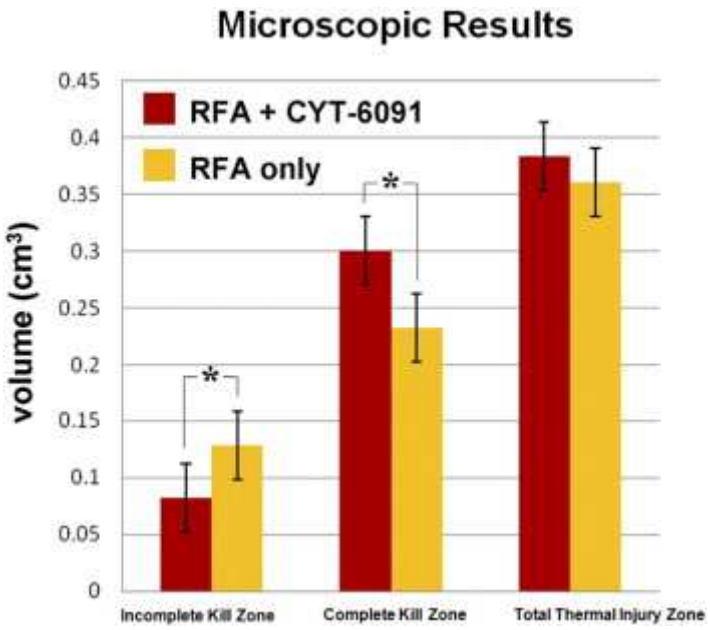

Figure 4.3. Volumes of different thermal injury zones in the RFA only versus RFA plus CYT-6091 based on microscopic measurements. Error bars represent 95% confidence intervals.

The dark red rim observed macroscopically corresponded with a band of vascular congestion and thrombosis, which coincided with the beginning of the incomplete cell death zone in all RFA-treated kidneys. The volume of the incomplete cell death zone in the RFA + Nano group was significantly smaller than the RFA-only group (0.08 ± 0.02 vs 0.13 ± 0.05 cm^3, P = .01), a decrease of 38.4%. Interestingly, there was no significant difference in the volumes of the total thermal injury zone between the RFA-only and the RFA + Nano groups (0.38 ± 0.07 vs 0.36 ± 0.08 cm^3, P = .98).

4.4. COMMENT

Compared with conventional surgical treatments of RCC, RFA offers many advantages. It can be delivered via a percutaneous technique that is relatively easy to learn and has few complications and low patient morbidity [143, 144]. However, there are limitations with this treatment that include difficulty treating tumors >4 cm in diameter, difficulty treating tumors that abut vital anatomic structures, and incomplete ablation rates of up to 9.1% [138]. Although resolution of all of these problems will likely require improvements in ablation device design and radiologic monitoring of ablation, the use of an adjuvant agent to enhance the thermal ablation is an appealing option. Previous authors have investigated a number of different means of achieving this goal. Initially mechanical means were used to occlude vascular flow into the kidney at the time of ablation. This unfortunately led to an unpredictable and uncontrollable ablation [145]. Further efforts were focused on pharmacologic manipulation. Arsenic trioxide, liposomal

doxorubicin, and sorafenib have all been studied as adjuvants to RFA in the kidney. These adjuvants are directly cytotoxic to tumor cells (doxorubicin) or tumor vasculature (sorafenib). In normal rabbit kidney tissue, Ahmed et al. found that injection of liposomal doxorubicin 30 minutes after RFA resulted in a significantly larger ablation (11 vs 7.9 mm, $P = .026$), but in contrast to our findings, the hemorrhagic rim expanded with the adjuvant as opposed to decreasing in size [146]. The authors speculated that RFA causes increased accumulation of liposomal doxorubicin in the tumor tissue and causes direct cytotoxicity of tumor cells. More recently, the same group investigated sorafenib in a murine RCC animal model. Here tumors were implanted subcutaneously on the abdominal wall. Again, the addition of an adjuvant increased the RFA size significantly from 6.7 to 11.1 mm ($P < .01$) [147]. However, sorafenib needed to be administered daily until a minor reduction in tumor size was observed before administering RFA therapy. Despite this promising in vivo work, these adjuvants are not yet commonly used clinically.

Here we propose a novel nanoparticle-based adjuvant, CYT-6091, for enhancing renal RFA. This nanoparticle has been previously well studied in vivo and in an early phase I clinical trial. Initially, TNF-α was studied as an adjuvant thermal ablation agent. However, resulting systemic effects were prohibitive. Thus, TNF-α was bonded to gold nanoparticles in the hopes of maximizing tumor delivery and minimizing systemic effects [74]. An initial phase I clinical trial has been done using CYT-6091 as a treatment (without ablation) for patients with solid organ tumors resistant to standard therapies.

Although this trial did not involve thermal ablation, it showed minimal to no systemic effects of CYT-6091 in 16 humans over a short course of treatment [69]. In regard to its thermal adjuvant properties, CYT-6091 has been tested in multiple animal tumor model systems. Visaria et al. demonstrated that pretreatment of both murine fibrosarcoma and murine mammary tumors with CYT-6091 before hyperthermia treatment lead to significant decreases in tumor volume relative to either CYT-6091 or hyperthermia alone [67, 68]. Interestingly, a similar effect can be seen with cryoablation as well. Goel and colleagues used a dorsal skin fold chamber to show that appropriate dosing of CYT-6091 increases the threshold temperature for necrosis in LNCaP prostate cancer tumors during cryoablation from −14 to −1.5°C [84]. In contrast to the adjuvants described earlier, we believe that a single intravenous administration of appropriately dosed CYT-6091 selectively presensitizes tumor vasculature to thermal cytotoxic effects thus enhancing the tumor destructive effects of RFA. As a corollary to our current study, we performed similar experiments using CYT-6091 with cryoablation as opposed to RFA. Due to difficulties with tumor regrowth into the ablation area it was not possible to confirm an enlarged ablation area, but we did see a marked change in metastasis rates with 8 out 10 animals in the cryoablation only arm versus only 1 out of 10 animals in the CYT-6091 plus cryoablation arm showing metastatic disease [109].

Our experimental model has a number of potential weaknesses. The clinical application of this technology is treatment of renal cell carcinoma, but no available animal model of renal cell carcinoma can support sufficient tumor growth within the

kidney to allow reproducible measurement of CYT-6091 induced changes in ablation volume. Thus, while CYT-6091 has shown effectiveness in a variety of tumors and both RFA and cryoablation, it is possible that its effects may differ with renal cell carcinoma. Finally, within this model we have not yet varied the administration timing or dosage of CYT-6091. Clearly, potential for changes in efficacy exist when moving to human trials.

4.5. CONCLUSIONS

In the current study we have demonstrated the efficacy of CYT-6091 in enhancing radiofrequency ablation in a translational kidney tumor model. While CYT-6091 administration alone had a significant effect on reducing tumor volume, the combination of radiofrequency ablation and CYT-6091 produced the most significant results by increasing the size of the complete cell death (central necrosis) zone and minimizing the incomplete cell death zone within the thermal lesion. The potential usage of CYT-6091 to improve radiofrequency ablation of renal cell carcinoma merits further study.

Chapter 5: Conclusions

This chapter summarizes all the data in the dissertation and proposes future avenues of investigation based on this work.

5.1. SUMMARY

The research presented in this dissertation was based on the global hypothesis that nanoparticle preconditioning is mediated by vascular and immunological events which include tumor associated phenomena such as vascular leak and thrombosis and leukocyte recruitment occurring within the tumor tissue. In essence, this research has demonstrated that a vascular destructive agent, TNF, (which is toxic in its native form at the high doses required for anti-cancer efficacy) when tagged on to a gold nanoparticle is safely and selectively delivered to tumor tissues to initiate a wide range of biological effects that are of importance in combinatorial cancer therapy. This work is summarized below under the specific aims that guided the experiments:

Specific Aim 1: *Demonstrate enhancement of thermal therapy (heat and cold) by NP preconditioning in the same tumor model (Chapters 2 & 4, Appendices C & D).*

- NP preconditioning was shown to enhance cryosurgery and high-temperature thermal therapy (HTT) in a preclinical prostate cancer model in both 2D DSFC and 3D hindlimb tumor models with no systemic toxicity.
- Thermal thresholds of injury were accentuated in both heat and cold thermal therapies by NP predconditioning.In the 2D DSFC model, NP preconditioning led to an 80% increase in the treated tumor volume by cryosurgery while a 61% increase was obtained with HTT. Conservative thermal threshold protocols (edge of tumor = iceball edge or 40^{o}C) were followed for hindlimb thermal therapy

which still yielded a significant therapeutic effect (tumor growth delay) due to NP preconditioning.

- NP preconditioning was shown to enhance radiofrequency ablation (RFA) in a translational rabbit kidney tumor model also with no systemic toxicity. NP preconditioning of RFA resulted in a larger zone of central necrosis with a smaller transition zone while the total size of the ablation remained unchanged.
- Cryosurgery in the translational rabbit kidney tumor model was marred by tumor regrowth into the lesion which confounded the histological measurements needed to show therapeutic benefit by NP preconditioning. However, a significant decrease in the rate of peritoneal metastases was observed with NP preconditioning of cryosurgery in the translational model.
- An immunocompetent preclinical model (TRAMP-C2) was tested although technical difficulties with DSFC implantation and maintenance and rapid tumor growth kinetics precluded continuation of that line of work.

Specific Aim 2: *Characterize NP preconditioning events (Chapter 3)*

- A model was proposed and tested to explain the potential preconditioning mechanisms taking place in the tumor tissue prior to a secondary tumor challenge such as thermal therapy.
- CYT-6091 was shown to localize in close proximity to the tumor endothelium 4 hrs after systemic administration.

- Tumor endothelial NFκB activation was not significantly higher than controls at 4 hrs after CYT-6091 administration and NFκB inhibition and VCAM-1 inhibition did not reduce NP preconditioning.
- A significant 80% drop in tumor perfusion was demonstrated 4 hrs after CYT-6091 injection that persisted up to at least 6 hrs. Doubling the dose of CYT-6091 injected did not decrease the perfusion further implying that the maximum perfusion drop achievable had been achieved.
- NP preconditioning was also associated with a rapid increase in tumor vascular permeability within 1-2 hrs of CYT-6091 injection. NP preconditioning also led to vasodilation and lumen areas of blood vessels were dilated by 14% at 4hrs after nanoparticle injection.

Specific Aim 3: *Assess role of leukocyte recruitment in NP preconditioning*

- To repeat, unlike topically delivered native TNF, NFκB and VCAM-1 inhibition did not reduce enhancement of cryosurgical injury. NFκB activation and VCAM-1 upregulation are important events in the cascade of leukocyte recruitment.
- NP preconditioning did not lead to increased leukocyte recruitment at 4 hrs after CYT-6091 administration.
- About 85-90% systemic neutrophil depletion was achieved using an RB6-8C5 antibody, however, this too did not reduce the enhancement of NP preconditioning.

- Lastly, the Day 3 cryosurgical lesion revealed an intense recruitment of leukocytes in tumors preconditioned with topical native TNF as compared to NP preconditioned tumors. However, both groups had enhanced cryosurgical injury.
- Overall, there is little evidence supporting an important role for neutrophils in NP preconditioning.

5.2. FUTURE DIRECTIONS

Several new avenues of investigation have opened up since this work was begun even though the concept of preconditioning thermal therapy using a molecular adjuvant has been established and investigated in our lab over the past several years:

1. The role of T cells and B cells in the host response to thermal injury cannot be discounted and development of an immunocompetent preclinical model is imperative for further development of the nanoparticle preconditioning concept.
2. The induction of vascular permeability during NP preconditioning opens the door to combinatorial therapy with chemotherapeutics which suffer due to rapid efflux from tumor tissue leading to decreased therapeutic efficacy. NP preconditioning mediated selective induction of vascular leak could potentially lead to the accumulation of higher concentrations of chemotherapeutics within tumors and increase therapeutic efficacy. A pilot experiment combining doxorubicin and

CYT-6091 could be conducted in a preclinical model to test if this approach warrants further study.

3. The vascular leak phenomenon could also be harnessed to increase delivery of nanoparticles into tumors. Indeed our biodistribution data shows that the presence of TNF on the gold nanoparticle increases its accumulation in tumor tissue. Experiments are currently being designed to quantify NP preconditioning mediated vascular leak using both small molecule and macromolecular dyes. The same approach can also be used to deliver a nanoparticle.
4. NP preconditioning mediated vascular effects – perfusion drop and vascular leak – offer the opportunity to monitor preconditioning using clinical imaging technology. Our lab is currently testing the use of contrast enhanced ultrasound (CEUS) to image perfusion drop in AT-1 tumors in rats. Similarly, vascular leak offers the opportunity for imaging using CT or MRI with a small molecule contrast agent. Selective accumulation of the contrast agent within the tumor will essentially cause the tumor to “light up” on a CT or MRI scan. This approach would allow patient-specific planning and administration of a secondary tumor challenge to maximize therapeutic efficacy
5. The present work demonstrated the impact (or lack thereof) of neutrophils in NP preconditioning. The next step would be to test the importance of circulating monocytes. Biodistribution data in our lab has shown that nanoparticles are taken up monocytes when they enter the systemic circulation. It would be interesting to

study the fate and activation status of monocytes that have taken up CYT-6091 particles and if there is any impact on the tumor.

6. Lastly, the present work strongly implicates that vascular mechanisms dominate NP preconditioning. Hence the coagulation pathway needs to be whetted thoroughly and the role of platelets in NP preconditiong also needs to be evaluated.
7. Both TNF and gold nanoparticles are known to independently affect vascular permeability and TNF is known to induce vascular permeability by activating p38 MAPK pathway. A set of in vitro experiments using molecular inhibitors to probe the p38 MAPK pathway is warranted to understand the mechanisms of CYT-6091 induced vascular hyperpermeability.

BIBLIOGRAPHY

1. Ferrari M: Cancer nanotechnology: opportunities and challenges. *Nat Rev Cancer* 5(3), 161-171 (2005).
2. Nie S, Xing Y, Kim GJ, Simons JW: Nanotechnology applications in cancer. *Annu Rev Biomed Eng* 9, 257-288 (2007).
3. Xie J, Lee S, Chen X: Nanoparticle-based theranostic agents. *Adv Drug Deliv Rev*, (2010).
4. Juzenas P, Chen W, Sun YP *et al.*: Quantum dots and nanoparticles for photodynamic and radiation therapies of cancer. *Adv Drug Deliv Rev* 60(15), 1600-1614 (2008).
5. Cancer Facts & Figures 2009. American Cancer Society, Atlanta. (2009).
6. Libutti SK, Paciotti GF, Byrnes AA *et al.*: Phase I and Pharmacokinetic Studies of CYT-6091, a Novel PEGylated Colloidal Gold-rhTNF Nanomedicine. *Clin Cancer Res*, (2010).
7. *Tumor Ablation: Principles and Practice*. VanSonnenberg E, McMullen W, Solbiati L (Ed.^(Eds). Springer, New York (2005).
8. Mulier S, Ni Y, Jamart J, Ruers T, Marchal G, Michel L: Local recurrence after hepatic radiofrequency coagulation: multivariate meta-analysis and review of contributing factors. *Ann Surg* 242(2), 158-171 (2005).
9. Jones JS, Rewcastle JC, Donnelly BJ, Lugnani FM, Pisters LL, Katz AE: Whole gland primary prostate cryoablation: initial results from the cryo on-line data registry. *J Urol* 180(2), 554-558 (2008).
10. Dewey WC: Arrhenius relationships from the molecule and cell to the clinic. *Int J Hyperthermia* 10(4), 457-483 (1994).
11. Gage AA, Baust JG: Cryosurgery for tumors. *J Am Coll Surg* 205(2), 342-356 (2007).
12. Day ES, Morton JG, West JL: Nanoparticles for thermal cancer therapy. *J Biomech Eng* 131(7), 074001 (2009).
13. Gilchrist RK, Medal R, Shorey WD, Hanselman RC, Parrott JC, Taylor CB: Selective inductive heating of lymph nodes. *Ann Surg* 146(4), 596-606 (1957).
14. Maier-Hauff K, Rothe R, Scholz R *et al.*: Intracranial thermotherapy using magnetic nanoparticles combined with external beam radiotherapy: results of a feasibility study on patients with glioblastoma multiforme. *J Neurooncol* 81(1), 53-60 (2007).
15. Johannsen M, Gneveckow U, Taymoorian K *et al.*: Morbidity and quality of life during thermotherapy using magnetic nanoparticles in locally recurrent prostate cancer: results of a prospective phase I trial. *Int J Hyperthermia* 23(3), 315-323 (2007).
16. Zharov VP, Galitovskaya EN, Johnson C, Kelly T: Synergistic enhancement of selective nanophotothermolysis with gold nanoclusters: potential for cancer therapy. *Lasers Surg Med* 37(3), 219-226 (2005).

17. Skrabalak SE, Chen J, Au L, Lu X, Li X, Xia Y: Gold Nanocages for Biomedical Applications. *Adv Mater Deerfield* 19(20), 3177-3184 (2007).
18. Huang X, El-Sayed IH, Qian W, El-Sayed MA: Cancer cell imaging and photothermal therapy in the near-infrared region by using gold nanorods. *J Am Chem Soc* 128(6), 2115-2120 (2006).
19. Huang N, Wang H, Zhao J, Lui H, Korbelik M, Zeng H: Single-wall carbon nanotubes assisted photothermal cancer therapy: Animal study with a murine model of squamous cell carcinoma. *Lasers Surg Med* 42(9), 638-648 (2010).
20. von Maltzahn G, Park JH, Agrawal A *et al.*: Computationally guided photothermal tumor therapy using long-circulating gold nanorod antennas. *Cancer Res* 69(9), 3892-3900 (2009).
21. Zhou M, Zhang R, Huang M *et al.*: A Chelator-Free Multifunctional [(64)Cu]CuS Nanoparticle Platform for Simultaneous Micro-PET/CT Imaging and Photothermal Ablation Therapy. *J Am Chem Soc* 132(43), 15351-15358 (2010).
22. Hirsch LR, Stafford RJ, Bankson JA *et al.*: Nanoshell-mediated near-infrared thermal therapy of tumors under magnetic resonance guidance. *Proc Natl Acad Sci U S A* 100(23), 13549-13554 (2003).
23. Curley SA, Cherukuri P, Briggs K *et al.*: Noninvasive radiofrequency field-induced hyperthermic cytotoxicity in human cancer cells using cetuximab-targeted gold nanoparticles. *J Exp Ther Oncol* 7(4), 313-326 (2008).
24. Byrne JD, Betancourt T, Brannon-Peppas L: Active targeting schemes for nanoparticle systems in cancer therapeutics. *Adv Drug Deliv Rev* 60(15), 1615-1626 (2008).
25. Issels RD: Hyperthermia adds to chemotherapy. *Eur J Cancer* 44(17), 2546-2554 (2008).
26. Griffin RJ, Ogawa A, Williams BW, Song CW: Hyperthermic enhancement of tumor radiosensitization strategies. *Immunological investigations* 34(3), 343-359 (2005).
27. Dudar TE, Jain RK: Differential response of normal and tumor microcirculation to hyperthermia. *Cancer Res* 44(2), 605-612 (1984).
28. Koning G, Eggermont A, Lindner L, ten Hagen T: Hyperthermia and Thermosensitive Liposomes for Improved Delivery of Chemotherapeutic Drugs to Solid Tumors. *Pharmaceutical Research* 27(8), 1750-1754 (2010).
29. Lin JC, Yuan PMK, Jung DT: Enhancement of anticancer drug delivery to the brain by microwave induced hyperthermia. *Bioelectrochemistry and Bioenergetics* 47(2), 259-264 (1998).
30. Franckena M, De Wit R, Ansink AC *et al.*: Weekly systemic cisplatin plus locoregional hyperthermia: an effective treatment for patients with recurrent cervical carcinoma in a previously irradiated area. *Int J Hyperthermia* 23(5), 443-450 (2007).
31. Sneed PK, Stauffer PR, McDermott MW *et al.*: Survival benefit of hyperthermia in a prospective randomized trial of brachytherapy boost +/- hyperthermia for glioblastoma multiforme. *Int J Radiat Oncol Biol Phys* 40(2), 287-295 (1998).

32. van der Zee J, Gonzalez, G.D., van Rhoon, G.C., van Dijk, J.D., van Putten, W.L., Hert, A.A.: Comparison of radiotherapy alone with radiotherapy plus hyeprthermia in locally advanced pelvic tumors: a prospective, randomized, multicentre trial. Dutch Deep Hyperthemic Group. *Lancet* 355(9210), 1119-1125 (2000).
33. Colombo R, Da Pozzo LF, Salonia A *et al.*: Multicentric study comparing intravesical chemotherapy alone and with local microwave hyperthermia for prophylaxis of recurrence of superficial transitional cell carcinoma. *J Clin Oncol* 21(23), 4270-4276 (2003).
34. Ponce AM, Vujaskovic Z, Yuan F, Needham D, Dewhirst MW: Hyperthermia mediated liposomal drug delivery. *Int J Hyperthermia* 22(3), 205-213 (2006).
35. Goldberg SN, Kamel IR, Kruskal JB *et al.*: Radiofrequency ablation of hepatic tumors: increased tumor destruction with adjuvant liposomal doxorubicin therapy. *AJR Am J Roentgenol* 179(1), 93-101 (2002).
36. Ahmed M, Lukyanov AN, Torchilin V, Tournier H, Schneider AN, Goldberg SN: Combined radiofrequency ablation and adjuvant liposomal chemotherapy: effect of chemotherapeutic agent, nanoparticle size, and circulation time. *J Vasc Interv Radiol* 16(10), 1365-1371 (2005).
37. Schwerdt A, Zintchenko A, Concia M *et al.*: Hyperthermia-induced targeting of thermosensitive gene carriers to tumors. *Hum Gene Ther* 19(11), 1283-1292 (2008).
38. Zhang W, Rong J, Wang Q, He X: The encapsulation and intracellular delivery of trehalose using a thermally responsive nanocapsule. *Nanotechnology* (27), 275101 (2009).
39. Hanna E, Quick J, Libutti SK: The tumour microenvironment: a novel target for cancer therapy. *Oral Dis* 15(1), 8-17 (2009).
40. Powell AC, Paciotti GF, Libutti SK: Colloidal gold: a novel nanoparticle for targeted cancer therapeutics. *Methods Mol Biol* 624, 375-384 (2010).
41. Thamm DH, Kurzman ID, Clark MA *et al.*: Preclinical investigation of PEGylated tumor necrosis factor alpha in dogs with spontaneous tumors: phase I evaluation. *Clin Cancer Res* 16(5), 1498-1508 (2010).
42. Siemann DW, Chaplin DJ, Horsman MR: Vascular-targeting therapies for treatment of malignant disease. *Cancer* 100(12), 2491-2499 (2004).
43. Horsman MR, Murata R: Combination of vascular targeting agents with thermal or radiation therapy. *Int J Radiat Oncol Biol Phys* 54(5), 1518-1523 (2002).
44. Murata R, Overgaard J, Horsman MR: Potentiation of the anti-tumour effect of hyperthermia by combining with the vascular targeting agent 5,6-dimethylxanthenone-4-acetic acid. *Int J Hyperthermia* 17(6), 508-519 (2001).
45. Hinnen P, Eskens FA: Vascular disrupting agents in clinical development. *Br J Cancer* 96(8), 1159-1165 (2007).
46. Hines-Peralta A, Sukhatme V, Regan M, Signoretti S, Liu ZJ, Goldberg SN: Improved tumor destruction with arsenic trioxide and radiofrequency ablation in three animal models. *Radiology* 240(1), 82-89 (2006).

47. Kumar V, Fausto N, Abbas A: Robbins & Cotran Pathologic Basis of Disease, Seventh Edition. (7). Saunders, (2004).
48. Adams R, Schachtrup C, Davalos D, Tsigelny I, Akassoglou K: Fibrinogen signal transduction as a mediator and therapeutic target in inflammation: lessons from multiple sclerosis. *Current Medicinal Chemistry* 14(27), 2925-2936 (2007).
49. Pallavicini MG, Hill RP: Effect of tumor blood flow manipulations on radiation response. *Int J Radiat Oncol Biol Phys* 9(9), 1321-1325 (1983).
50. Kano MR, Bae Y, Iwata C *et al.*: Improvement of cancer-targeting therapy, using nanocarriers for intractable solid tumors by inhibition of TGF-beta signaling. *Proc Natl Acad Sci U S A* 104(9), 3460-3465 (2007).
51. Garay RP, Viens P, Bauer J *et al.*: Cancer relapse under chemotherapy: why TLR2/4 receptor agonists can help. *Eur J Pharmacol* 563(1-3), 1-17 (2007).
52. Moschella F, Proietti E, Capone I, Belardelli F: Combination strategies for enhancing the efficacy of immunotherapy in cancer patients. *Ann N Y Acad Sci* 1194, 169-178 (2010).
53. Bouwhuis MG, Suciu S, Testori A *et al.*: Phase III trial comparing adjuvant treatment with pegylated interferon Alfa-2b versus observation: prognostic significance of autoantibodies--EORTC 18991. *J Clin Oncol* 28(14), 2460-2466
54. Agarwala SS, Glaspy J, O'Day SJ *et al.*: Results from a randomized phase III study comparing combined treatment with histamine dihydrochloride plus interleukin-2 versus interleukin-2 alone in patients with metastatic melanoma. *J Clin Oncol* 20(1), 125-133 (2002).
55. Yang JC, Topalian SL, Schwartzentruber DJ *et al.*: The use of polyethylene glycol-modified interleukin-2 (PEG-IL-2) in the treatment of patients with metastatic renal cell carcinoma and melanoma. A phase I study and a randomized prospective study comparing IL-2 alone versus IL-2 combined with PEG-IL-2. *Cancer* 76(4), 687-694 (1995).
56. Cocco C, Pistoia V, Airoldi I: New perspectives for melanoma immunotherapy: role of IL-12. *Curr Mol Med* 9(4), 459-469 (2009).
57. Lei C, Liu P, Chen B *et al.*: Local release of highly loaded antibodies from functionalized nanoporous support for cancer immunotherapy. *J Am Chem Soc* 132(20), 6906-6907 (2010).
58. Flavell RA, Sanjabi S, Wrzesinski SH, Licona-Limon P: The polarization of immune cells in the tumour environment by TGFbeta. *Nat Rev Immunol* 10(8), 554-567 (2010).
59. Hennessy EJ, Parker AE, O'Neill LA: Targeting Toll-like receptors: emerging therapeutics? *Nat Rev Drug Discov* 9(4), 293-307 (2010).
60. Redondo P, del Olmo J, Lopez-Diaz de Cerio A *et al.*: Imiquimod enhances the systemic immunity attained by local cryosurgery destruction of melanoma lesions. *J Invest Dermatol* 127(7), 1673-1680 (2007).
61. den Brok MH, Sutmuller RP, Nierkens S *et al.*: Synergy between in situ cryoablation and TLR9 stimulation results in a highly effective in vivo dendritic cell vaccine. *Cancer Res* 66(14), 7285-7292 (2006).

62. Udagawa M, Kudo-Saito C, Hasegawa G *et al.*: Enhancement of immunologic tumor regression by intratumoral administration of dendritic cells in combination with cryoablative tumor pretreatment and Bacillus Calmette-Guerin cell wall skeleton stimulation. *Clin Cancer Res* 12(24), 7465-7475 (2006).
63. Yamanaka R, Homma J, Yajima N *et al.*: Clinical evaluation of dendritic cell vaccination for patients with recurrent glioma: results of a clinical phase I/II trial. *Clin Cancer Res* 11(11), 4160-4167 (2005).
64. Cubillos-Ruiz JR, Engle X, Scarlett UK *et al.*: Polyethylenimine-based siRNA nanocomplexes reprogram tumor-associated dendritic cells via TLR5 to elicit therapeutic antitumor immunity. *J Clin Invest* 119(8), 2231-2244 (2009).
65. Dominguez AL, Lustgarten J: Targeting the tumor microenvironment with anti-neu/anti-CD40 conjugated nanoparticles for the induction of antitumor immune responses. *Vaccine* 28(5), 1383-1390 (2010).
66. Jiang J, Goel R, Iftekhar MA *et al.*: Tumor necrosis factor-{alpha}-induced accentuation in cryoinjury: mechanisms in vitro and in vivo. *Mol Cancer Ther* 7(8), 2547-2555 (2008).
67. Visaria R, Bischof JC, Loren M *et al.*: Nanotherapeutics for enhancing thermal therapy of cancer. *Int J Hyperthermia* 23(6), 501-511 (2007).
68. Visaria RK, Griffin RJ, Williams BW *et al.*: Enhancement of tumor thermal therapy using gold nanoparticle-assisted tumor necrosis factor-{alpha} delivery. *Mol Cancer Ther* 5(4), 1014-1020 (2006).
69. Libutti SK, Paciotti GF, Myer L *et al.*: Results of a completed phase I clinical trial of CYT-6091: A pegylated colloidal gold-TNF nanomedicine. *J Clin Oncol (Meeting Abstracts)* 27(15S), 3586- (2009).
70. van Horssen R, Ten Hagen TL, Eggermont AM: TNF-alpha in cancer treatment: molecular insights, antitumor effects, and clinical utility. *Oncologist* 11(4), 397-408 (2006).
71. Lin JC, Park HJ, Song CW: Combined treatment of IL-1 alpha and TNF-alpha potentiates the antitumour effect of hyperthermia. *Int J Hyperthermia* 12(3), 335-344 (1996).
72. Sun Z, Yan J, Rao W, Liu J: Particularities of tissue types in treatment planning of nano cryosurgery. In: 2008.
73. Shalkevich N, Escher W, Bu rgi T, Michel B, Si-Ahmed L, Poulikakos D: On the Thermal Conductivity of Gold Nanoparticle Colloids. *Langmuir* 26(2), 663-670 (2009).
74. Goel R, Shah N, Visaria R, Paciotti GF, Bischof JC: Biodistribution of TNF-alpha-coated gold nanoparticles in an in vivo model system. *Nanomed* 4(4), 401-410 (2009).
75. Perrault SD, Walkey C, Jennings T, Fischer HC, Chan WC: Mediating tumor targeting efficiency of nanoparticles through design. *Nano Lett* 9(5), 1909-1915 (2009).
76. De Jong WH, Hagens WI, Krystek P, Burger MC, Sips AJ, Geertsma RE: Particle size-dependent organ distribution of gold nanoparticles after intravenous administration. *Biomaterials* 29(12), 1912-1919 (2008).

77. James W, Hirsch L, West J, O'Neal P, Payne J: Application of INAA to the build-up and clearance of gold nanoshells in clinical studies in mice. *Journal of Radioanalytical and Nuclear Chemistry* 271(2), 455-459 (2007).
78. Petros RA, DeSimone JM: Strategies in the design of nanoparticles for therapeutic applications. *Nat Rev Drug Discov* 9(8), 615-627 (2010).
79. Paciotti GF, Myer L, Weinreich D *et al.*: Colloidal gold: a novel nanoparticle vector for tumor directed drug delivery. *Drug Deliv* 11(3), 169-183 (2004).
80. Shah NB, Dong J, Bischof JC: Cellular uptake and nanoscale localization of gold nanoparticles in cancer using label free Confocal Raman Microscopy. *Mol Pharm*, (2010).
81. Pober JS, Sessa WC: Evolving functions of endothelial cells in inflammation. *Nat Rev Immunol* 7(10), 803-815 (2007).
82. ten Hagen TL, Seynhaeve AL, Eggermont AM: Tumor necrosis factor-mediated interactions between inflammatory response and tumor vascular bed. *Immunol Rev* 222, 299-315 (2008).
83. Farma JM, Puhlmann M, Soriano PA *et al.*: Direct evidence for rapid and selective induction of tumor neovascular permeability by tumor necrosis factor and a novel derivative, colloidal gold bound tumor necrosis factor. *Int J Cancer* 120(11), 2474-2480 (2007).
84. Goel R, Swanlund D, Coad J, Paciotti GF, Bischof JC: TNF-{alpha}-based accentuation in cryoinjury--dose, delivery, and response. *Mol Cancer Ther* 6(7), 2039-2047 (2007).
85. Jiang J, Bischof J: Effect of timing, dose and interstitial versus nanoparticle delivery of tumor necrosis factor alpha in combinatorial adjuvant cryosurgery treatment of ELT-3 uterine fibroid tumor. *Cryo Letters* 31(1), 50-62 (2010).
86. Griffin RJ, Lee SH, Rood KL *et al.*: Use of arsenic trioxide as an antivascular and thermosensitizing agent in solid tumors. *Neoplasia* 2(6), 555-560 (2000).
87. Griffin RJ, Monzen H, Williams BW, Park H, Lee SH, Song CW: Arsenic trioxide induces selective tumour vascular damage via oxidative stress and increases thermosensitivity of tumours. *Int J Hyperthermia* 19(6), 575-589 (2003).
88. Griffin RJ, Williams BW, Bischof JC, Olin M, Johnson GL, Lee BW: Use of a fluorescently labeled poly-caspase inhibitor for in vivo detection of apoptosis related to vascular-targeting agent arsenic trioxide for cancer therapy. *Technol Cancer Res Treat* 6(6), 651-654 (2007).
89. Siemann DW: The unique characteristics of tumor vasculature and preclinical evidence for its selective disruption by Tumor-Vascular Disrupting Agents. *Cancer Treatment Reviews* In Press, Corrected Proof, (2010).
90. Shalaby MR, Palladino MA, Jr., Hirabayashi SE *et al.*: Receptor binding and activation of polymorphonuclear neutrophils by tumor necrosis factor-alpha. *J Leukoc Biol* 41(3), 196-204 (1987).
91. Jiang J, Goel R, Schmechel S, Vercellotti G, Forster C, Bischof J: Pre-Conditioning Cryosurgery: Cellular and Molecular Mechanisms and Dynamics of

TNF-alpha Enhanced Cryotherapy in an in vivo Prostate Cancer Model System. *Cryobiology*, (2010).
92. Di Carlo E, Forni G, Lollini P, Colombo MP, Modesti A, Musiani P: The intriguing role of polymorphonuclear neutrophils in antitumor reactions. *Blood* 97(2), 339-345 (2001).
93. Allavena P, Sica A, Garlanda C, Mantovani A: The Yin-Yang of tumor-associated macrophages in neoplastic progression and immune surveillance. *Immunol Rev* 222, 155-161 (2008).
94. Boon T, Coulie PG, Van den Eynde BJ, van der Bruggen P: Human T cell responses against melanoma. *Annu Rev Immunol* 24, 175-208 (2006).
95. Balza E, Mortara L, Sassi F *et al.*: Targeted delivery of tumor necrosis factor-alpha to tumor vessels induces a therapeutic T cell-mediated immune response that protects the host against syngeneic tumors of different histologic origin. *Clin Cancer Res* 12(8), 2575-2582 (2006).
96. Yang JC, Hughes M, Kammula U *et al.*: Ipilimumab (anti-CTLA4 antibody) causes regression of metastatic renal cell cancer associated with enteritis and hypophysitis. *J Immunother* 30(8), 825-830 (2007).
97. Hoffmann NE, Bischof JC: The cryobiology of cryosurgical injury. *Urology* 60(2 Suppl 1), 40-49 (2002).
98. Nikfarjam M, Muralidharan V, Christophi C: Mechanisms of focal heat destruction of liver tumors. *Journal of Surgical Research* 127(2), 208-223 (2005).
99. Gage AA, Baust JM, Baust JG: Experimental cryosurgery investigations in vivo. *Cryobiology* 59(3), 229-243 (2009).
100. Lepock J: Cellular effects of hyperthermia: relevance to the minimum dose for thermal damage. *International Journal of Hyperthermia* 19(3), 252-266 (2003).
101. Coad JE, Kosari K, Humar A, Sielaff TD: Radiofrequency ablation causes 'thermal fixation' of hepatocellular carcinoma: a post-liver transplant histopathologic study. *Clinical Transplantation* 17(4), 377-384 (2003).
102. Gazzaniga S, Bravo A, Goldszmid S *et al.*: Inflammatory changes after cryosurgery-induced necrosis in human melanoma xenografted in nude mice. *Journal of Investigative Dermatology* 116(5), 664-671 (2001).
103. Esmon C: The interactions between inflammation and coagulation. *British journal of haematology* 131(4), 417-430 (2005).
104. Sabel MS: Cryo-immunology: a review of the literature and proposed mechanisms for stimulatory versus suppressive immune responses. *Cryobiology* 58(1), 1-11 (2009).
105. Skitzki JJ, Repasky EA, Evans SS: Hyperthermia as an immunotherapy strategy for cancer. *Curr Opin Investig Drugs* 10(6), 550-558 (2009).
106. Gallucci S, Lolkema M, Matzinger P: Natural adjuvants: endogenous activators of dendritic cells. *Nat Med* 5(11), 1249-1255 (1999).
107. Goel R, Paciotti GF, Bischof JC: Tumor necrosis factor-alpha induced enhancement of cryosurgery. In: *Proceedings of SPIE*. 2008.

108. Pedro RN, Thekke-Adiyat T, Goel R *et al.*: Use of Tumor Necrosis Factor-alpha-coated Gold Nanoparticles to Enhance Radiofrequency Ablation in a Translational Model of Renal Tumors. *Urology* 76(2), 494-498
109. Shenoi MM, Anderson JK, Bischof JC: Nanoparticle enhanced thermal therapies. In: *Engineering in Medicine and Biology Society, 2009. EMBC 2009. Annual International Conference of the IEEE*. 3-6 Sept 2009.
110. Seshadri M, Toth K: Acute vascular disruption by 5,6-dimethylxanthenone-4-acetic Acid in an orthotopic model of human head and neck cancer. *Transl Oncol* 2(3), 121-127 (2009).
111. Salmon BA, Salmon HW, Siemann DW: Monitoring the treatment efficacy of the vascular disrupting agent CA4P. *Eur J Cancer* 43(10), 1622-1629 (2007).
112. Gross S, Gammon ST, Moss BL *et al.*: Bioluminescence imaging of myeloperoxidase activity in vivo. *Nat Med* 15(4), 455-461 (2009).
113. Rodriguez E, Nilges M, Weissleder R, Chen JW: Activatable magnetic resonance imaging agents for myeloperoxidase sensing: mechanism of activation, stability, and toxicity. *J Am Chem Soc* 132(1), 168-177
114. Rubinsky B: Cryosurgery. *Annu Rev Biomed Eng* 2, 157-187 (2000).
115. Gage AA, Baust J: Mechanisms of tissue injury in cryosurgery. *Cryobiology* 37(3), 171-186 (1998).
116. Baust JG, Gage AA, Klossner D *et al.*: Issues critical to the successful application of cryosurgical ablation of the prostate. *Technol Cancer Res Treat* 6(2), 97-109 (2007).
117. Rewcastle JC, Sandison GA, Hahn LJ, Saliken JC, McKinnon JG, Donnelly BJ: A model for the time-dependent thermal distribution within an iceball surrounding a cryoprobe. *Phys Med Biol* 43(12), 3519-3534 (1998).
118. Chao BH, He X, Bischof JC: Pre-treatment inflammation induced by TNF-alpha augments cryosurgical injury on human prostate cancer. *Cryobiology* 49(1), 10-27 (2004).
119. Jemal A, Siegel R, Ward E, Murray T, Xu J, Thun MJ: Cancer statistics, 2007. *CA Cancer J Clin* 57(1), 43-66 (2007).
120. Guess HA: Benign prostatic hyperplasia and prostate cancer. *Epidemiol Rev* 23(1), 152-158 (2001).
121. Chang SS: Management of high risk metastatic prostate cancer: defining risk at the time of initial treatment failure. *J Urol* 176(6 Pt 2), S57-60; discussion S55-56 (2006).
122. D'Amico A: Global update on defining and treating high-risk localized prostate cancer with leuprorelin: a USA perspective--identifying men at diagnosis who are at high risk of prostate cancer death after surgery or radiation therapy. *BJU Int* 99 Suppl 1, 13-16; discussion 17-18 (2007).
123. Horsman MR, Bohn AB, Busk M: Vascular targeting therapy: potential benefit depends on tumor and host related effects. *Exp Oncol* 32(3), 143-148 (2010).
124. Balkwill F: Tumour necrosis factor and cancer. *Nat Rev Cancer* 9(5), 361-371 (2009).

125. R Development Core Team. R: A language and environment for statistical computing. R Foundation for Statistical Computing, Vienna, Austria. ISBN 3-900051-07-0, URL http://www.R-project.org/. (2011).
126. Bhowmick S, Hoffmann NE, Bischof JC: Thermal therapy of prostate tumor tissue in the dorsal skin flap chamber. *Microvasc Res* 64(1), 170-173 (2002).
127. Bhowmick S, Swanlund DJ, Coad JE, Lulloff L, Hoey MF, Bischof JC: Evaluation of thermal therapy in a prostate cancer model using a wet electrode radiofrequency probe. *J Endourol* 15(6), 629-640 (2001).
128. He X, McGee S, Coad JE *et al.*: Investigation of the thermal and tissue injury behaviour in microwave thermal therapy using a porcine kidney model. *Int J Hyperthermia* 20(6), 567-593 (2004).
129. Robaye B, Mosselmans R, Fiers W, Dumont JE, Galand P: Tumor necrosis factor induces apoptosis (programmed cell death) in normal endothelial cells in vitro. *Am J Pathol* 138(2), 447-453 (1991).
130. Hezi-Yamit A, Wong PW, Bien-Ly N *et al.*: Synergistic induction of tissue factor by coagulation factor Xa and TNF: evidence for involvement of negative regulatory signaling cascades. *Proc Natl Acad Sci U S A* 102(34), 12077-12082 (2005).
131. Walmsley SR, Cowburn AS, Sobolewski A *et al.*: Characterization of the survival effect of tumour necrosis factor-alpha in human neutrophils. *Biochem Soc Trans* 32(Pt3), 456-460 (2004).
132. Belcher JD, Mahaseth H, Welch TE *et al.*: Critical role of endothelial cell activation in hypoxia-induced vasoocclusion in transgenic sickle mice. *Am J Physiol Heart Circ Physiol* 288(6), H2715-2725 (2005).
133. Breitbach CJ, De Silva NS, Falls TJ *et al.*: Targeting tumor vasculature with an oncolytic virus. *Mol Ther* 19(5), 886-894 (2011).
134. Ferrero E, Zocchi MR, Magni E *et al.*: Roles of tumor necrosis factor p55 and p75 receptors in TNF-alpha-induced vascular permeability. *Am J Physiol Cell Physiol* 281(4), C1173-1179 (2001).
135. Bonizzi G, Karin M: The two NF-kappaB activation pathways and their role in innate and adaptive immunity. *Trends Immunol* 25(6), 280-288 (2004).
136. Mileski WJ, Raymond JF, Winn RK, Harlan JM, Rice CL: Inhibition of leukocyte adherence and aggregation for treatment of severe cold injury in rabbits. *J Appl Physiol* 74(3), 1432-1436 (1993).
137. Berger A, Crouzet S, Canes D, Haber GP, Gill IS: Minimally invasive nephron-sparing surgery. *Curr Opin Urol* 18(5), 462-466 (2008).
138. Levinson AW, Su LM, Agarwal D *et al.*: Long-term oncological and overall outcomes of percutaneous radio frequency ablation in high risk surgical patients with a solitary small renal mass. *J Urol* 180(2), 499-504; discussion 504 (2008).
139. Margulis V, Matsumoto ED, Lindberg G *et al.*: Acute histologic effects of temperature-based radiofrequency ablation on renal tumor pathologic interpretation. *Urology* 64(4), 660-663 (2004).
140. Rehman J, Landman J, Lee D *et al.*: Needle-based ablation of renal parenchyma using microwave, cryoablation, impedance- and temperature-based monopolar

and bipolar radiofrequency, and liquid and gel chemoablation: laboratory studies and review of the literature. *J Endourol* 18(1), 83-104 (2004).
141. Ahmed M, Goldberg SN: Combination radiofrequency thermal ablation and adjuvant IV liposomal doxorubicin increases tissue coagulation and intratumoural drug accumulation. *Int J Hyperthermia* 20(7), 781-802 (2004).
142. Boehm T, Folkman J, Browder T, O'Reilly MS: Antiangiogenic therapy of experimental cancer does not induce acquired drug resistance. *Nature* 390(6658), 404-407 (1997).
143. Carraway WA, Raman JD, Cadeddu JA: Current status of renal radiofrequency ablation. *Curr Opin Urol* 19(2), 143-147 (2009).
144. Anderson JK, Cadeddu JA: Radiofrequency ablation: the preferred minimally invasive treatment. *J Endourol* 22(9), 1913-1915; discussion 1927 (2008).
145. Corwin TS, Lindberg G, Traxer O *et al.*: Laparoscopic radiofrequency thermal ablation of renal tissue with and without hilar occlusion. *J Urol* 166(1), 281-284 (2001).
146. Ahmed M, Liu Z, Lukyanov AN *et al.*: Combination radiofrequency ablation with intratumoral liposomal doxorubicin: effect on drug accumulation and coagulation in multiple tissues and tumor types in animals. *Radiology* 235(2), 469-477 (2005).
147. Hakime A, Hines-Peralta A, Peddi H *et al.*: Combination of radiofrequency ablation with antiangiogenic therapy for tumor ablation efficacy: study in mice. *Radiology* 244(2), 464-470 (2007).

Appendix A

In Vivo Comparison of Simultaneous v Sequential Injection Technique for Thermochemical Ablation in a Porcine Model

This chapter describes the first set of experiments demonstrating the capability of a new ablation method, thermochemical ablation, to produce in vivo lesions in a porcine liver model for the treatment of hepatocellular carcinoma. The results from this chapter have been submitted as the following citation that is in review at the time of this dissertation submission:

- Cressman ENK, Shenoi MM, Edelman TL, Geeslin MG, Hennings LJ, Zhang Y, Iaizzo PA, Bischof JC. In vivo comparison of simultaneous v sequential injection technique for thermochemical ablation in a porcine model. Int J Hyperthermia (accepted).

A.1. INTRODUCTION

Treatment of solid tumors such as hepatocellular carcinoma (HCC) that respond poorly to IV chemotherapy or newer targeted agents is an ongoing challenge [1-3]. Surgery is often held to be the gold standard, but the majority of patients are disqualified due to tumor location, degree of underlying liver disease, multiple or infiltrative tumors, or comorbidities. In response, alternative therapies have been developed for ablation or embolization. While interest in these methods continues to grow, chemical ablation would seem to have been relegated to historical interest. Nevertheless, it does offer benefits worthy of further consideration and study [4-6].

The two chemical ablation agents receiving the most attention in the literature are ethanol and 50% acetic acid [7-10]. Delivery is usually via instillation through a multiple side-hole needle under ultrasound or CT guidance. Systemic toxicity limits the amount that can be safely delivered [11-14]. This results in smaller doses and multiple treatment sessions and is one of the major criticisms of this technique. The other major criticism is that hydrostatic pressure from intraparenchymal injection forces the agent to follow the path of least resistance. This can cause unpredictable distribution of the agent and may result in inadequate treatment, damage to nontarget tissues, and/or systemic exposure. With the advent of multitined needle devices and premedication protocols, these criticisms can be addressed to some extent [15-18]. This approach, however, does not appear to have been widely adopted.

An alternative to conventional chemical ablation would be to address the dose limiting toxicity problem through a strategy designed to create local conditions that preserve local toxicity but decrease the systemic toxicity. If hyperthermia and hyperosmolarity were intrinsic components of a chemical method, thermal conductive effects and concentration effects in tissue might lead to a more predictable zone of coagulation. If successful, such an approach could potentially allow safe, predictable treatment of large tumor volumes in a single session, thereby addressing both of the major criticisms of chemical ablation.

Thermochemical ablation is a concept in which exothermic reactions are used as a heat source. One such reaction is neutralization of an acid by a base, which could be done with either simultaneous or sequential administration of the reagents. The purpose of this study is to investigate these two injection methods in a porcine model, and compare them to sham as a negative control and acid-only ablation as a positive control. The porcine model was chosen to allow for adequate size for prototype device placement and monitoring. No porcine tumor models are readily available and there is an extensive body of ablation literature in pigs [19]. Thus healthy swine were utilized for these experiments. Temperatures, coagulation volumes, sphericities, and histopathology were analyzed. Our hypothesis is that combined injection would improve on acid ablation by increasing coagulum volume and be as well or better tolerated than acid alone.

A.2. MATERIALS AND METHODS

Animal handling

Animals were treated in accordance with protocols reviewed and approved by the institutional animal care and use committee and cared for as recommended in the Guide for the Care and Use of Laboratory Animals. Eleven swine 60-75 kg were acclimated perinstitutional guidelines. After induction of anesthesia (tiletamine/zolazepam/xylazine 0.4 mL/kg IM then 2-5% isoflurane) and surgical exposure intraoperative ultrasound allowed device placement into the liver at least 10 mm away from major vessels (10 MHz Z.one Ultra System, Zonare Medical Systems, Inc., Mountain View, CA). Euthanasia was accomplished with pentobarbital/phenytoin 0.2 mg/kg IV. Blood pressure, heart rate, and oxygenation were recorded at 30-second intervals.

Reagents and device preparation

Acetic acid and sodium hydroxide (Sigma-Aldrich Corp., St. Louis, MO, USA) were diluted to 10 mol/L. Iodinated contrast (iodixanol, GE Healthcare) was used at 5% v/v in acid for all injections and saline sham to aid in visualization at CT. A 17G device was assembled as reported by Farnam et al with slight modifications: the trocar tip was cut free then soldered to the outer cannula and side holes were created near the tip of the cannula [20].

Temperature measurements

A 23G thermocouple (Physitemp type T MT_23/3, Physitemp Instruments, Clifton, NJ, USA) was inserted parallel at 5 mm to the same depth. Temperature data were monitored continuously and recorded every 5 seconds with a T-type thermocouple (Digi-Sense, Cole-Palmer Instrument Co., Vernon Hills, IL, USA).

Ablation (injection) experiments

Reagent concentrations were 10 mol/L prewarmed to 40°C. Four different injections were carried out in each liver in the same sequence for all 11 animals: sham, simultaneous, sequential, and acid-only for a total of 44 injections. The device was assembled, connected to the syringes by extension tubing, and primed prior to insertion into the liver. Separate lobes were used for each injection to avoid cross-contamination issues. A syringe pump (Standard Infusion Only Harvard Pump 11 Plus Dual Syringe Pump, Harvard Apparatus, Holliston, Massachusetts) delivered a combined 4 mL/min from two syringes with 2 mL volumes of reagent in each. In the saline sham and acid-only injections where a single syringe was used, the rate was also 4 mL/min. Volume in these cases was kept constant at 2 mL. Acid was injected first in all sequential injections. Hemostasis at the conclusion of each injection was obtained by inserting a piece of spaghetti into the tract [21]. Temperature was recorded for 5-10 minutes after each injection. Livers were fixed in 10% neutral buffered formalin for sectioning.

Gross pathology

Gross images of 2mm thick specimens were obtained and analyzed in ImageJ (NIH).

Two independent, unblinded observers (MG and MS) obtained tracings of the coagulated regions to allow measurement of the perimeter and area of each slice. Outer margins were used for measurement, but demarcations were generally very narrow (<2mm) and clearly demarcated between affected and unaffected tissues. Area and perimeter were then used with slice thickness to calculate slice volumes, total volume, 3-D surface area, and sphericity for each treatment. Data are reported in accordance with Society of Interventional Radiology Reporting Standards [22, 23].

Sphericity calculations

The sphericity corresponds to mathematical convention in which the surface area/volume ratio of a sphere is represented by a value of 1. Sphericity was calculated using the following formula:

$\Psi = (\pi^{1/3}(6V_p)^{2/3})/A_p$ where V_p = Volume and A_p = surface area

Values less than 1 correlate with the degree of deviation away from an ideal sphere.

Histology

After gross pathology analysis, the formalin-fixed specimens 2mm thick were processed and embedded into paraffin, sectioned at 5 microns and stained with hematoxylin and eosin. Approximately 1.5 cm x 1cm sections were taken from central and margin zones of each sample. Hemorrhage was graded by one unblinded observer, (LH) on a scale of 0

(no hemorrhage present) to 4 (severe hemorrhage affecting greater than 30% of the section). Degree of ablation was assessed microscopically.

Imaging

CT imaging of explanted livers to interrogate the relationship of contrast distribution from the injections and the zones of coagulation was performed on a Siemens Sensation 64 scanner (Erlangen, Germany) with the following parameters: mAs 400, 120 kVp, 1mm slice width, 0.6 mm collimation, pitch 0.7, and rotation time of 0.5 sec. Multiplanar reconstructions were created and archived for further review.

Statistical analysis

Outcomes including ablation volume, sphericity, and temperature, (except sham as no detectable changes were noted) were measured. General linear models for random block design were used to determine the effects of injection types (simultaneous, sequential, and acid alone) on ablation volume and sphericity, temperature, and change in heart rate. The variance-covariance structure was compound symmetry. P values were adjusted by Tukey's method. Inter-observer agreement on ablation volume and sphericity by two observers was evaluated using intraclass correlation coefficients (ICC) from general linear models for split-plot design, with lesions from the same animal as the whole-plot experiment units and observer as the split-plot factor. All analyses were conducted in SAS 9.2 (SAS Institute Inc., Cary, NC, USA). A p-value of less than 0.05 indicated significance.

A.3. RESULTS

Temperatures in vivo

Average peak temperatures for each injection method are shown in **Figure A.1**. There were significant differences in mean temperature among the three treatment groups ($p<0.0001$). No temperature change was detected in the sham injections. The sequential injection mean temperature was intermediate (47.7°C), and simultaneous injection produced the highest mean temperature (61.1°C). Multiple pairwise comparisons all were significant: acid v sequential (adjusted $p=0.0397$), acid v simultaneous (adjusted $p<0.0001$), and sequential v simultaneous (adjusted $p=0.0009$). Maximum peak temperature was also considerably lower in the sequential v simultaneous injection (57°C v 81°C). It is noteworthy that the highest temperature measured in sequential injection was lower than the average temperature obtained with simultaneous injection. In addition heart rate changes were minimal in controls and simultaneous instillation but one pig arrested after sequential injection and had to be revived with epinephrine and a fluid bolus.

Histopathology and Imaging

Ablated regions exhibited coagulative to lytic necrosis (**Figure A.2**). Cells in these regions were shrunken with nuclear pyknosis to lysis and loss of cytoplasmic and membrane definition. The demarcation zone between ablated and unablated tissue was

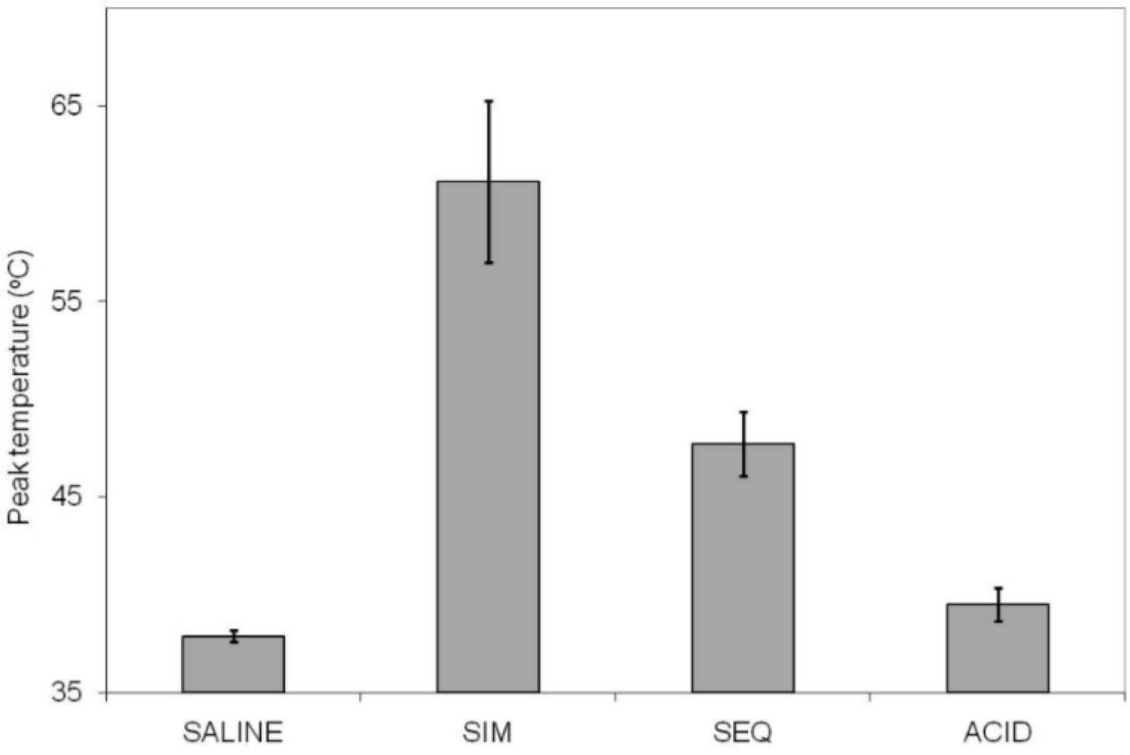

Figure A.1. Bar graph depiction of peak temperatures measured at thermocouple for (L to R) saline sham, simultaneous injection, sequential injection, and acid-only injection. All solutions had been warmed to 39-40°C (pig body temperature) prior to placing into a syringe pump with extension tubing to the device. SIM = simultaneous injection; SEQ = sequential injection.

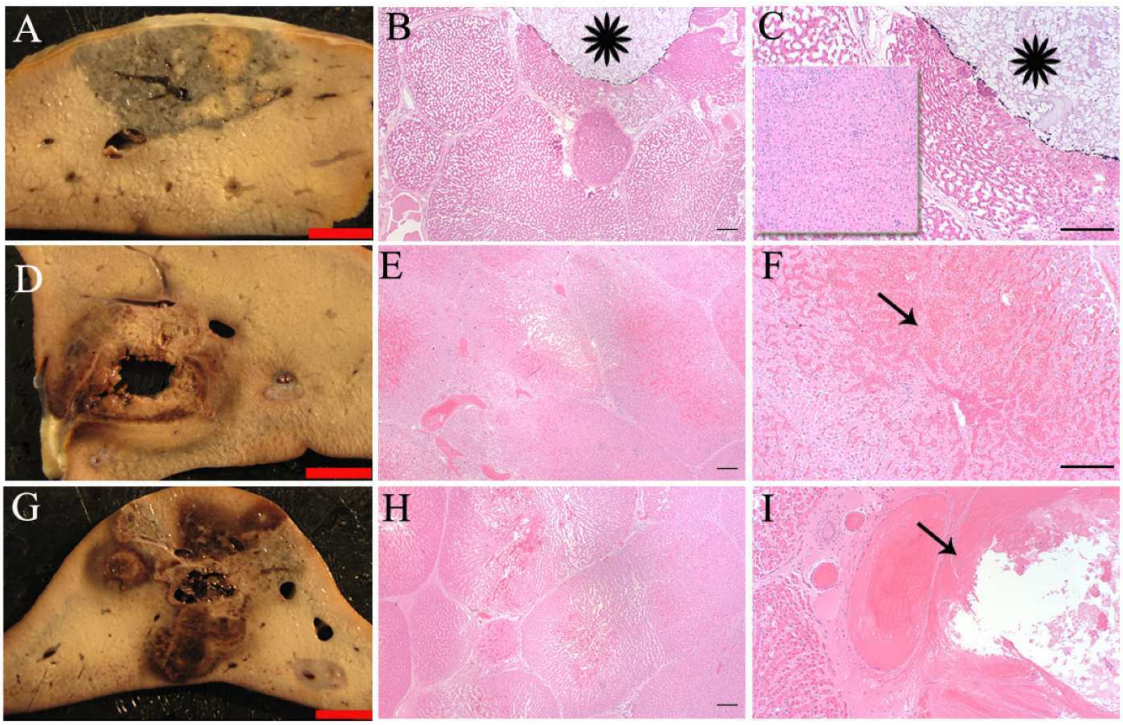

Figure A.2. Histology: Gross and corresponding histologic sections after acid (A,B,C), simultaneous (D,E,F) or sequential (G, H, I) injection. Cells in ablated regions exhibit coagulative necrosis and are shrunken with pale cytoplasm and indistinct nuclei compared to unablated tissue (inset, C). Hemorrhage is obvious in simultaneous and sequential sections (E,F, arrows). Imaging marker (spaghetti) is visible in histologic sections (B,C, stars). A,D,G: Bar equals 1cm. ,B,E,H: H&E, 40x magnification, bars equal 100um. C,F,I: H&E, 100x magnification, bars equal 100um.

most clearly delineated for sequential and simultaneous injection, largely due to congestion of sinusoids and hemorrhage at the margins of the lesion. Hemorrhage was visible in gross sections as red to black areas (**Figure A.2, D,G**). Mild hemorrhage was rarely noted in sections treated with acid only. Both sequential and simultaneous treatments exhibited increased hemorrhage compared to acid only (**Figure A.2, B,E,H**). In both of these treatment groups, necrosis of large vessels occurred, and vessel damage, as indicated by margination of neutrophils and fibrin deposition to frank vascular necrosis, was evident in some vessels outside the central ablation zone (**Figure A.3**).

Correlation of pathology with CT imaging was uneven. The most consistent results were observed with acid-only injection (**Figure A.4**, first series).

Volumes and Lesion shapes

Volumes of the coagulated tissues for each method of injection are shown as bar graphs in **Figure A.5**. There were significant differences in mean ablation volumes for both observers among the three injection methods ($p=0.0006$ for observer 1, $p=0.0002$ for observer 2). Acid alone had the lowest least squares mean ablation volume (4.3 cc by observer 1 and 4.5 cc by observer 2). Simultaneous injection was intermediate (11.9 cc by observer 1 and 9.8 cc by observer 2), and sequential injection produced the highest least squares mean ablation volume (18.9 cc by observer 1 and 19.3 cc by observer 2).

Sphericity for each injection type is plotted in **Figure A.6**. The least squares means

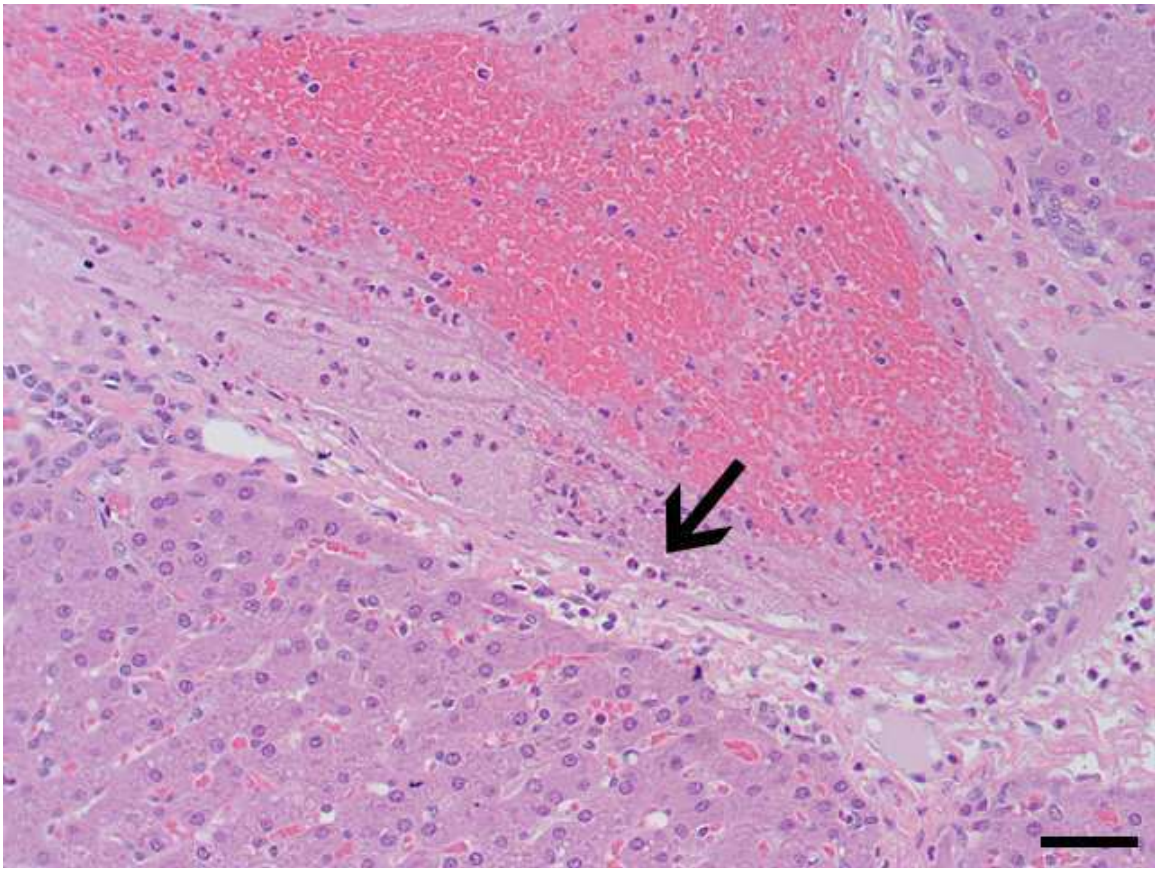

Figure A.3. Vascular damage adjacent to ablated region. Fibrin and neutrophils (arrow) adhere to vascular endothelium in vessel adjacent to viable hepatocytes. H&E, 200x magnification. Bar equals 50um.

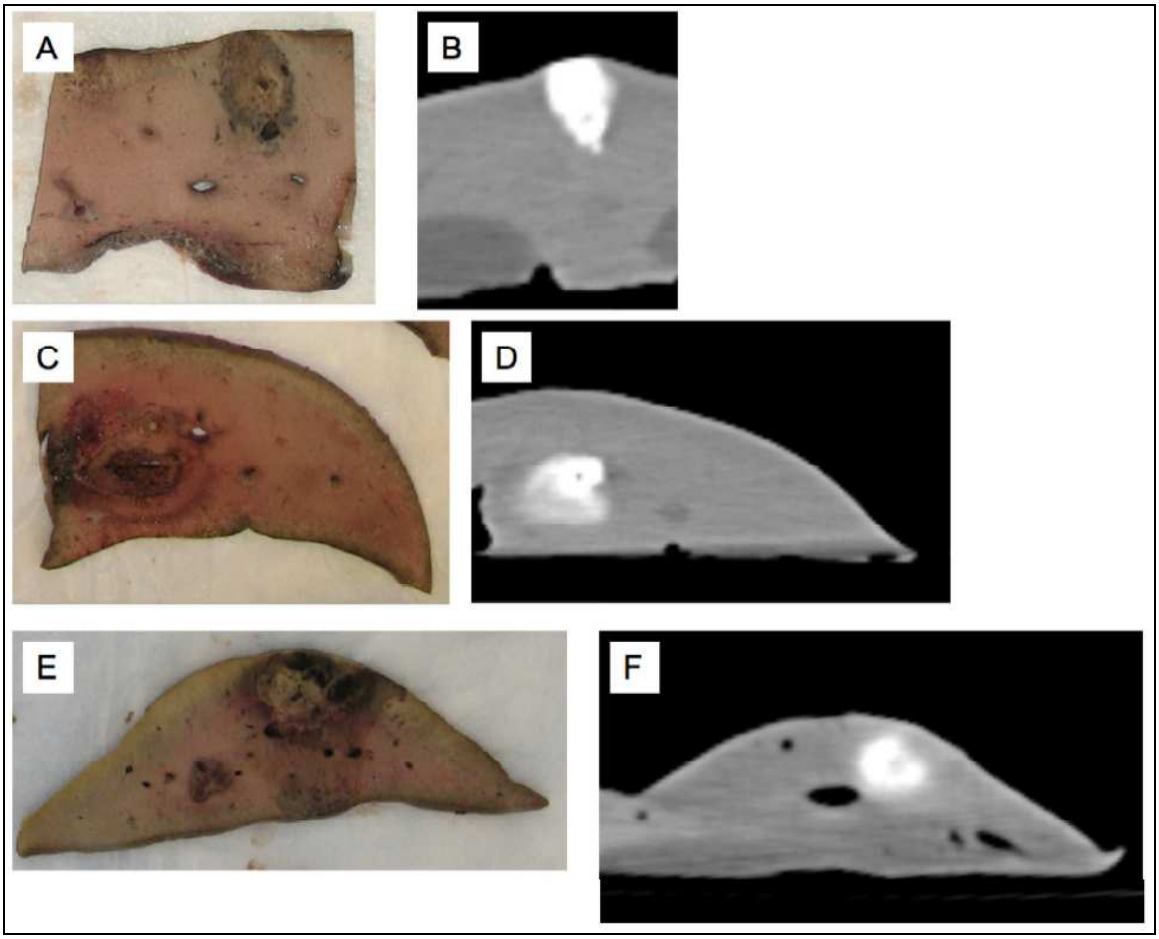

Figure A.4. Gross pathology correlations with adjacent CT rendering corresponding in each case. Acetic acid alone (A, B), simultaneous injection (C,D), sequential injection (E,F). Note that although acid alone correlates fairly well, with either of the two other methods there is inconsistent density and/or shape compared to CT.

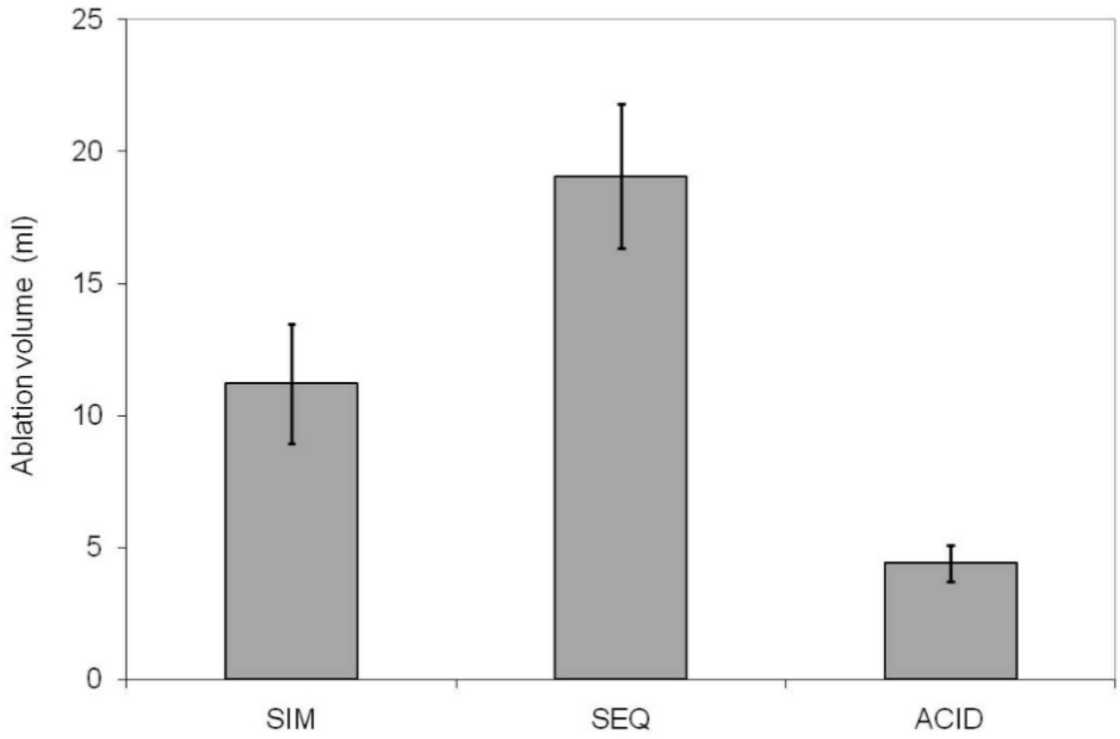

Figure A.5. Bar graph illustrating average summation volumes of zones of coagulation for simultaneous injection (SIM), sequential injection (SEQ), and acid alone. Saline sham is not listed as no detectable lesion was identified in that case.

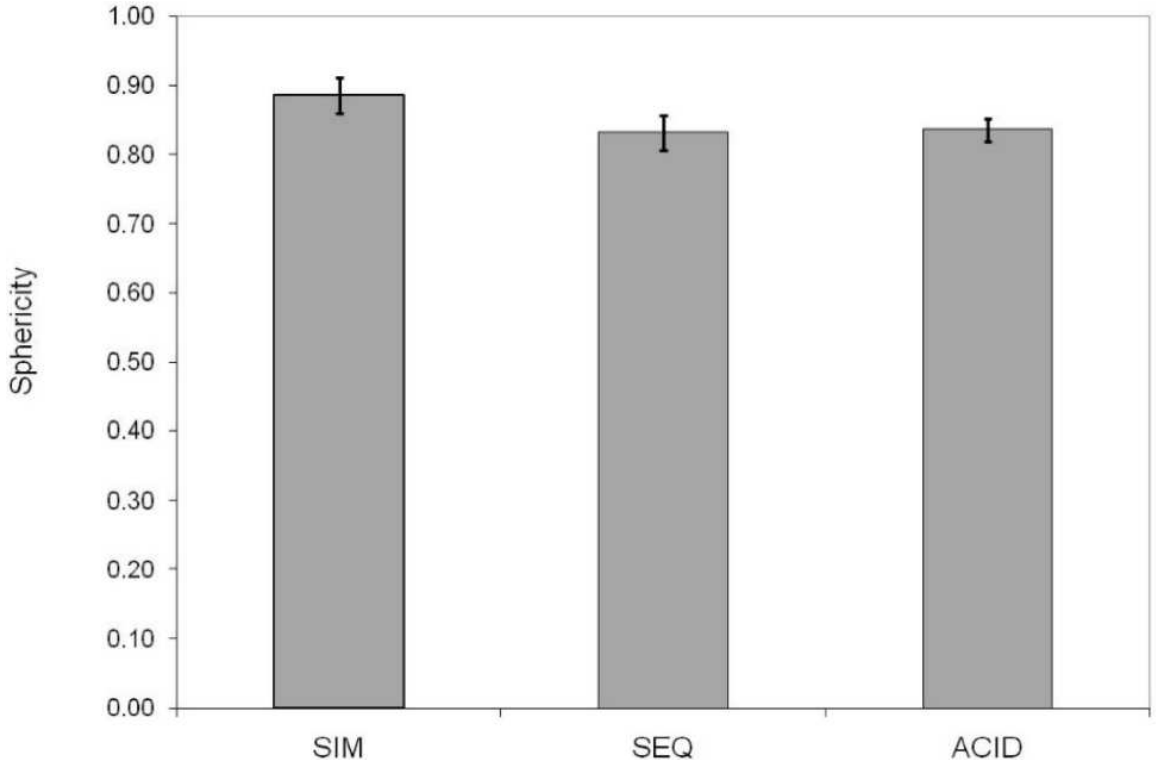

Figure A.6. Bar graph depiction of sphericity coefficients for simultaneous (SIM), sequential (SEQ), and acid-only injection. Saline sham is not listed as no detectable lesion was identified in that case.

of sphericity in acid injection, simultaneous and sequential methods were 0.87, 0.89 and 0.84, respectively for observer 1 and 0.80, 0.82 and 0.87 for observer 2. There were no significant differences in mean sphericity by either observer among three injection methods ($p=0.3920$ for observer 1, $p=0.1223$ for observer 2).

The ICC for volume was 0.8597 and that for sphericity was 0.7562, indicating strong agreement between the two observers for both outcomes.

A.4. DISCUSSION

Recently, exothermic acid-base neutralization chemistry has been shown in phantom and ex vivo studies to have potential for tissue ablation based on the amount of energy released as water is formed [20, 24-26]. Oxidation-reduction chemistry has also been studied and can be more energetic but may have greater limitations regarding toxicity [27]. With respect to acids and bases, salts are formed as a result of neutralization and in tissues can be present at concentrations many times higher than the physiologic range. With simultaneous injection the acid and base would be consumed in the formation of the salts. Therefore the deviation from neutral pH should be minimal if reaction occurred to completion. Under these circumstances, exposure to either an acid or base load that would alter the systemic pH should be effectively eliminated. These salts may also have local hyperosmolar effects leading to cell destruction as described in more detail below. Sequential injection on the other hand would still allow for some degree of mixing

directly in the tissues but by its nature would entail direct injection of unreacted, highly concentrated substances that could lead to systemic exposure and its consequences.

Reagent selection and conditions

Reagent choice for acid was based on existing clinical experience with acetic acid. Most clinical use of acetic acid is with 50% concentration which is approximately 8.5 molar. The use of 10 molar acid was based on anticipation of future studies using various concentrations and a desire to maintain a consistent body of data. Use of NaOH was based on the requirements for a strong base that would produce a salt, sodium acetate (NaOAc) composed of ions already present in the body. Furthermore, acetate is quickly converted to bicarbonate and thus whatever portion reached the systemic circulation should be readily metabolized [28]. Both the volume and the concentration of acid were kept constant in all injections because our purpose was to compare the other methods against it. Order of injections was likewise kept constant to minimize the number of variables.

Although the acid alone seemed to correlate fairly well with contrast distribution, the results from CT correlated poorly with the gross pathology as shown in **Figure A.4** [29]. We speculate that the solutions behave much as they would in column chromatography. That is to say that the different components would interact with and partition differently into the medium and thus migrate relative to the solvent front at different rates.

Temperatures in vivo

Volume data suggest that temperature may not be the dominant factor in determining the outcome of the ablation. A modest exotherm was observed with sequential injection but peak temperatures were recorded with simultaneous injection. One possible reason is that less mixing occurred with sequential injection.

Histopathology

Regions identified on gross examination as ablated exhibited complete necrosis, although we cannot rule out the presence of small foci of viable tissue within ablated regions in this small, acute study. Hemorrhage was most common after sequential and simultaneous treatment, suggesting a greater degree of vascular damage and possible intravascular administration or leakage of reagents or products (i.e. hyperosmolar sodium acetate).

Volume and Shape relationships

Agreement between observers on volume measurements was reasonably strong. Comparison of sphericity revealed no statistically significant differences among techniques or observers. The average coagulation volumes are illustrated in **Figure 5**. Conventional practice for acid ablation is to use an amount of acid that is 1/3 of the volume of the desired treatment volume. Therefore, given 2 cc of acid used, the predicted final coagulation volume would be in the range of 6 cc (i.e. a factor of 3). In this model however, we observed a slightly lower value, just over twice the injected volume for

coagulation. This could be due to the acute setting and in normal liver.

Comparison of the volumes from the different methods results in some interesting observations. There is a nearly 2.5-fold increase in coagulation volume over that seen with acid alone with simultaneous injection that was well tolerated. Sequential injection showed even larger volumes but this came at a price of less control and higher risk. In fact, one animal required resuscitation after cardiovascular collapse following a sequential injection, a situation not encountered with simultaneous injection. We believe this is due to the neutralization that occurred with simultaneous injection that may not have occurred with the sequential method but direct proof is lacking. The total injection time was only 1 minute and the amount of tissue ablated per minute would appear, at least initially, to be competitive with RF energy-based devices.

The sphericity coefficient ranged from 0.80-0.89, which was reasonably high. The injection rate in this model (4cc/min) was an order of magnitude faster than recommended with ethanol by Tapani et al for maintaining some control over shape and the injection volumes were considerably larger. Despite these differences, sphericity remained fairly high and within a narrow range [30]. We propose that this may be due to three factors: the effect of the thermal component, differences in viscosity compared to ethanol, and the in vivo nature of the experiment.

Mechanism of action

How thermochemical ablation (i.e. the simultaneous injection method) coagulates tissue is not yet known but at least two mechanisms, heat and hyperosmolarity, seem likely. We hypothesize that heat and hyperosmolarity act together additively or possibly synergistically, recognizing that the duration of temperature excursion is actually quite brief in comparison to conventional methods. Since the exotherm is so brief but the salt exposure is much longer in duration, the relative contributions of heat and hyperosmolarity must be studied in more detail to understand and assign their relative importance using this method. Presuming that the reaction occurred to completion in the simultaneous injection experiments, the salt was produced at a concentration of 5 mol/L. Due to the binary nature of the salt (two particles in solution) this was effectively 10 osmolar. Most physiologic settings are in the range of 270-300 mOsm. This means at the device tip, the salt concentration is 1 to 2 orders of magnitude higher than physiologic conditions. Furthermore the change in osmotic pressure occurred abruptly. Centrally where the temperature and osmotic pressure would already be extremely high this should not be an issue. However, at the margins, this still allowed essentially no time for cellular adaptation. The lytic necrosis observed histologically supports this idea.

The study had several important limitations. First, only one thermocouple was used. Multiple thermocouples could be incorporated or magnetic resonance thermography (MRT) could be considered to address this and evaluate the volume and time distribution of the temperature excursion. No direct comparison was made to a thermal therapy such as RF ablation. Lack of either tumor or cirrhosis as noted earlier, and the acute nature of

the experiments could affect the results with regard to distribution of the reagents in tissues and long-term effects. It will be of interest to further explore the relationship of volume injected and concentration to the coagulum volume. More detailed temperature studies such as MR thermography would further define the effects in real time and subacute studies would be useful for understanding the evolution of lesions. As the area is developed, transition to a tumor model will allow more rigorous evaluation of the method.

A.5. CONCLUSION

Thermochemical ablation produced substantial volumes of coagulated tissues relative to the amounts of reagents injected, considerably greater than acid alone in either technique employed. The largest volumes were obtained with sequential injection yet this came at a price in one case of cardiac arrest. Simultaneous injection yielded the highest recorded temperatures and may be tolerated as well as or better than acid injection alone. Although this pilot study did not show a clear advantage for either sequential or simultaneous methods, the results indicate that thermochemical ablation is attractive for further investigation with regard to both safety and efficacy.

A.6. ACKNOWLEDGEMENTS

University of Minnesota Department of Radiology

SIR Foundation Ernest J. Ring Faculty Development Award

This work was supported in part by NIH P30 CA77598 utilizing the following Masonic Cancer Center, University of Minnesota shared resource: Biostatistics and Bioinformatics Core.

A.7. REFERENCES

1. Kuo YH, Lu SN, Chen CL, Cheng YF, Lin CY, Hung CH, et al. Hepatocellular carcinoma surveillance and appropriate treatment options improve survival for patients with liver cirrhosis. Eur J Cancer 2010 Mar;46(4):744-751.
2. Schumacher PA, Powell JJ, MacNeill AJ, Buczkowski AK, Erb SR, Ho SG, et al. Multimodal therapy for hepatocellular carcinoma: a complementary approach to liver transplantation. Ann Hepatol 2010 Jan-Mar;9(1):23-32.
3. Cabibbo G, Enea M, Attanasio M, Bruix J, Craxi A, Camma C. A meta-analysis of survival rates of untreated patients in randomized clinical trials of hepatocellular carcinoma. Hepatology 2010 Apr;51(4):1274-1283.
4. Germani G, Pleguezuelo M, Gurusamy K, Meyer T, Isgro G, Burroughs AK. Clinical outcomes of radiofrequency ablation, percutaneous alcohol and acetic acid injection for hepatocelullar carcinoma: a meta-analysis. J Hepatol 2010 Mar;52(3):380-388.
5. Clark TW. Chemical ablation of liver cancer. Tech Vasc Interv Radiol 2007 Mar;10(1):58-63.
6. Clark TW, Soulen MC. Chemical ablation of hepatocellular carcinoma. J Vasc Interv Radiol 2002 Sep;13(9 Pt 2):S245-52.
7. Cho YB, Lee KU, Suh KS, Kim YJ, Yoon JH, Lee HS, et al. Hepatic resection compared to percutaneous ethanol injection for small hepatocellular carcinoma using propensity score matching. J Gastroenterol Hepatol 2007 Oct;22(10):1643-1649.
8. Fartoux L, Arrive L, Andreani T, Serfaty L, Chazouilleres O, Tubiana JM, et al. Treatment of small hepatocellular carcinoma with acetic acid percutaneous injection. Gastroenterol Clin Biol 2005 Dec;29(12):1213-1219.
9. Tsai WL, Cheng JS, Lai KH, Lin CP, Lo GH, Hsu PI, et al. Clinical trial: percutaneous acetic acid injection vs. percutaneous ethanol injection for small hepatocellular carcinoma--a long-term follow-up study. Aliment Pharmacol Ther 2008 Aug 1;28(3):304-311.
10. Schoppmeyer K, Weis S, Mossner J, Fleig WE. Percutaneous ethanol injection or percutaneous acetic acid injection for early hepatocellular carcinoma. Cochrane

Database Syst Rev 2009 Jul 8;(3)(3):CD006745.

11. Arnulf F, Monika S, Herwig S, Monika H, Johannes PD, Gregor U, et al. Atropine for prevention of cardiac dysrhythmias in patients with hepatocellular carcinoma undergoing percutaneous ethanol instillation: a randomized, placebo-controlled, doubleblind trial. Liver Int 2009 May;29(5):715-720.
12. Burton KR, O'Dwyer H, Scudamore C. Percutaneous ethanol ablation of hepatocellular carcinoma: periprocedural onset alcohol toxicity and pancreatitis following conventional percutaneous ethanol ablation treatment. Can J Gastroenterol 2009 Aug;23(8):554-556.
13. Sidi A, Naik B, Urdaneta F, Muehlschlegel JD, Kirby DS, Lobato EB. Treatment of ethanol-induced acute pulmonary hypertension and right ventricular dysfunction in pigs, by sildenafil analogue (UK343-664) or nitroglycerin. Ann Card Anaesth 2008 Jul- Dec;11(2):97-104.
14. Sidi A, Naik B, Muehlschlegel JD, Kirby DS, Lobato EB. Ethanol-induced acute pulmonary hypertension and right ventricular dysfunction in pigs. Br J Anaesth 2008 Apr;100(4):568-569.
15. Da Ines D, Buc E, Petitcolin V, Flamein R, Lannareix V, Achim A, et al. Massive hepatic necrosis with gastric, splenic, and pancreatic infarctions after ethanol ablation for hepatocellular carcinoma. J Vasc Interv Radiol 2010 Aug;21(8):1301-1305.
16. Lencioni R, Crocetti L, Cioni D, Pina CD, Oliveri F, De Simone P, et al. Singlesession percutaneous ethanol ablation of early-stage hepatocellular carcinoma with a multipronged injection needle: results of a pilot clinical study. J Vasc Interv Radiol 2010 Oct;21(10):1533-1538.
17. Kuang M, Lu MD, Xie XY, Xu HX, Xu ZF, Liu GJ, et al. Ethanol Ablation of Hepatocellular Carcinoma Up to 5.0 cm by Using a Multipronged Injection Needle with High-Dose Strategy. Radiology 2009 Aug 25.
18. Ho CS, Kachura JR, Gallinger S, Grant D, Greig P, McGilvray I, et al. Percutaneous ethanol injection of unresectable medium-to-large-sized hepatomas using a multipronged needle: efficacy and safety. Cardiovasc Intervent Radiol 2007 Mar-Apr;30(2):241-247.
19. Aravalli RN, Golzarian J, Cressman EN. Animal models of cancer in interventional radiology. Eur Radiol 2009 May;19(5):1049-1053.
20. Farnam JL, Smith BC, Johnson BR, Estrada R, Edelman TL, Farah R, et al. Thermochemical ablation in an ex-vivo porcine liver model using acetic acid and sodium hydroxide: proof of concept. J Vasc Interv Radiol 2010 Oct;21(10):1573-1578.
21. Okuda S, Kuroda K, Oshio K, Mulkern RV, Colucci V, Morrison PR, et al. MRbased temperature monitoring for hot saline injection therapy. J Magn Reson

Imaging 2000 Aug;12(2):330-338.
22. Goldberg SN, Grassi CJ, Cardella JF, Charboneau JW, Dodd GD,3rd, Dupuy DE, et al. Image-guided tumor ablation: standardization of terminology and reporting criteria. J Vasc Interv Radiol 2009 Jul;20(7 Suppl):S377-90.
23. Mulier S, Ni Y, Frich L, Burdio F, Denys AL, De Wispelaere JF, et al. Experimental and clinical radiofrequency ablation: proposal for standardized description of coagulation size and geometry. Ann Surg Oncol 2007 Apr;14(4):1381-1396.
24. Freeman LA, Anwer B, Brady RP, Smith BC, Edelman TL, Misselt AJ, et al. In vitro thermal profile suitability assessment of acids and bases for thermochemical ablation: underlying principles. J Vasc Interv Radiol 2010 Mar;21(3):381-385.
25. Misselt AJ, Edelman TL, Choi JH, Bischof JC, Cressman EN. A hydrophobic gel phantom for study of thermochemical ablation: initial results using a weak acid and weak base. J Vasc Interv Radiol 2009 Oct;20(10):1352-1358.
26. Deng ZS, Liu J. Minimally invasive thermotherapy method for tumor treatment based on an exothermic chemical reaction. Minim Invasive Ther Allied Technol 2007;16(6):341-346.
27. Cressman EN, Tseng HJ, Talaie R, Henderson BM. A new heat source for thermochemical ablation based on redox chemistry: Initial studies using permanganate. Int J Hyperthermia 2010 Mar 26.
28. Tsai IC, Huang JW, Chu TS, Wu KD, Tsai TJ. Factors associated with metabolic acidosis in patients receiving parenteral nutrition. Nephrology (Carlton) 2007 Feb;12(1):3-7.
29. Arrive L, Rosmorduc O, Dahan H, Fartoux L, Monnier-Cholley L, Lewin M, et al. Percutaneous acetic acid injection for hepatocellular carcinoma: using CT fluoroscopy to evaluate distribution of acetic acid mixed with an iodinated contrast agent. AJR Am J Roentgenol 2003 Jan;180(1):159-162.
30. Tapani E, Vehmas T, Voutilainen P. Effect of injection speed on the spread of ethanol during experimental liver ethanol injections. Acad Radiol 1996;3(12):1025-1029.

Appendix B

Concentration and Volume Effects in Thermochemical Ablation in vivo: results in a porcine model

This chapter describes experiments to explore the effects of volume and concentration in thermochemical ablation on temperature and volume of coagulated tissues obtained using an in vivo porcine model. The results from this chapter have been submitted as the following citation that is in review at the time of this dissertation submission:

- Cressman ENK, Geeslin MG, Shenoi MM, Hennings LJ, Zhang Y, Iaizzo PA, Bischof JC. Concentration and volume effects in thermochemical ablation in vivo: results in a porcine model. Int J Hyperthermia (accepted).

B.1. INTRODUCTION

Worldwide, primary cancer of the liver continues to draw attention for developing new therapies due to many reasons. Most patients are not candidates for surgical resection or transplant due to the location of the disease, multiplicity of tumors, severity of underlying liver disease, or some combination of the above factors [1-3]. The long history of clinical trials with poor outcomes for HCC from chemotherapy alone has finally changed in the right direction with the advent of targeted agents such as sorafenib [4,5]. It is unclear, however, how many patients will actually see a survival benefit, and for those who do see a benefit, how great that benefit is. For instance, there are numerous reports of patient intolerance to the full therapeutic dose and as yet no data supporting a benefit from less than the full dose [6].

The lack of suitable surgical and chemotherapeutic options has led to development of a wide array of minimally invasive therapies. Chemoembolization, radioembolization, chemical ablation, and thermal ablation all play a role for nonsurgical patients [7-14]. Percutaneous ethanol injection and acetic acid have both been used historically in chemical ablation although ethanol ablation under ultrasound guidance is by far the more widely employed of the two methods [15-18]. Opinion remains divided on the superiority of RF ablation over ethanol ablation for small HCCs but evidence in the literature is accumulating for lower rates of local recurrence with RF ablation than with ethanol [19-21].

Limitations to ethanol ablation include the need for multiple sessions, poor penetration of tumor septae, and tracking along pathways of least resistance. All the same, availability of ethanol worldwide is far greater than for other modalities due to the simplicity of the equipment required. Encouraging results have recently been reported using a multitined needle as a delivery system for larger volumes and more even distribution of ethanol [22-24]. Toxicity remains a limiting factor, however, resulting in an opportunity for devising a better therapy [25-28]. In order to improve the local tumor cytotoxicity while reducing systemic toxicity new approaches to local injection are needed.

Thermochemical ablation is a new concept in which two reactive solutions, such as an acid and a base, give off heat as they are brought together to react prior to entering the tissue as a hot salt solution. The combination of heat and high concentration of products is thought to create a locally cytotoxic environment that has been shown ex vivo to have potential to ablate tissue [29]. The salt that is produced may actually be one that is already present in the human body and thus easily excreted with little systemic toxicity. Furthermore, if chosen carefully, the reaction products would be close to physiologic pH values further mitigating against systemic toxicity. Therefore we hypothesized that it might eventually be possible with this method to treat large volumes rapidly, simply, safely, and at low cost. The purpose of the present study is to explore the relative contributions of volume and concentration of injected reagents to the temperatures and

volumes of coagulated tissue obtained. Pig physiology is reasonably close to human, and the scale is comparable, but no tumor model is readily available. Taking these factors into account, we used an in vivo in a porcine model with acetic acid and sodium hydroxide as the reagents for this study.

B.2. MATERIALS AND METHODS

Reagents and Device preparation

Acetic acid and sodium hydroxide (Sigma-Aldrich Corp., St. Louis, MO, USA) were diluted to necessary concentrations and were used at room temperature. The 17G prototype device was assembled in the same manner as reported by Farnam et al shown in **Figure B.1A** with the following modifications: the trocar shaft was removed so that the tip could be soldered to the outer cannula [29]. Sideholes were then created at the tip of the cannula for solutions to exit into the tissues.

Animal handling

Animals were treated in accordance with protocols reviewed and approved by the institutional animal care and use committee. Animals were cared for as recommended in the Guide for the Care and Use of Laboratory Animals. Twelve outbred swine weighing 60-75 kg were used and acclimated per institutional guidelines prior to procedures. After induction of general anesthesia using tiletamine/zolazepam/xylazine 0.4 mL/kg IM then 2-5% isoflurane, establishing an arterial line in the groin for blood pressure monitoring,

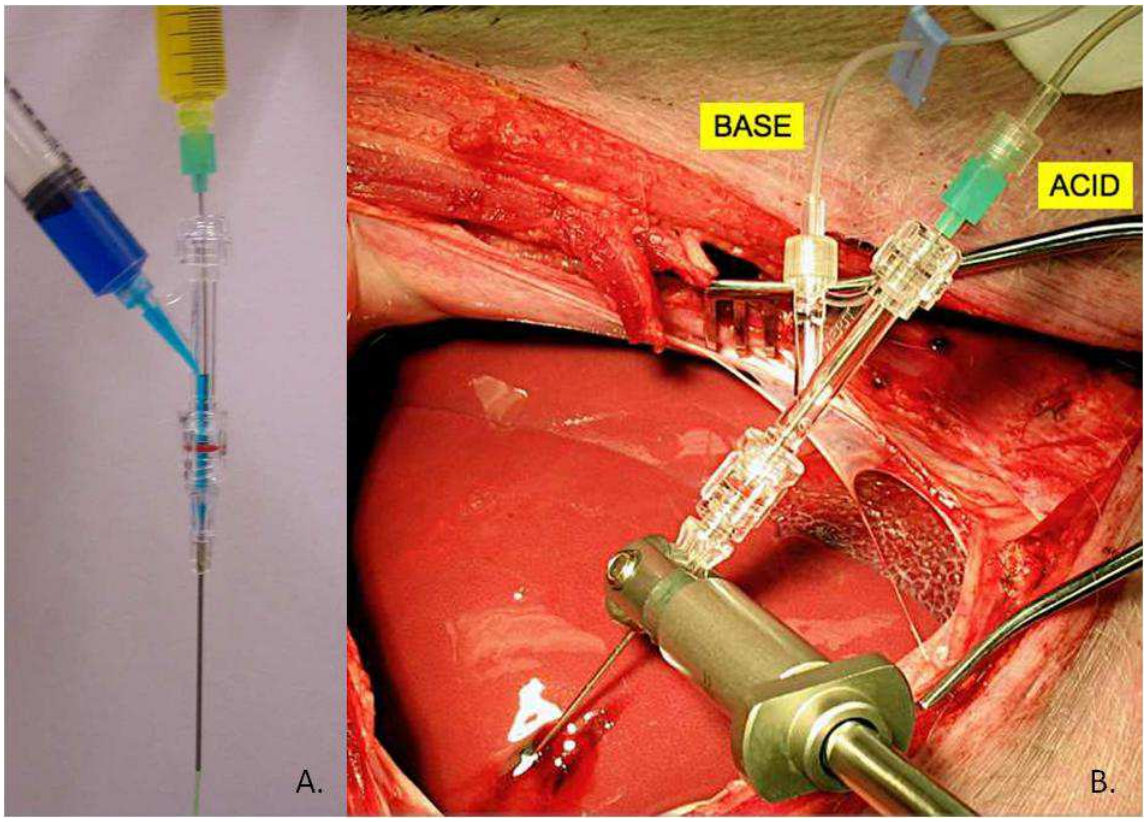

Figure B.1. Device in vitro and in vivo: A) Device with blue (side port) and yellow (coaxial port) colored water in channels demonstrating concept in which the two solutions mix near the tip and the resulting green solution exits the tip of the device. This earlier prototype is a simple endhole design, whereas the device used in this study (next image) had a solid tip with three sideholes created near it for egress of the heated salt solutions. B) Experimental setup showing liver surgically exposed, the device ready for use with base entering via sidearm of rotary hemostatic valve and acid entering via coaxial green hub needle. During simultaneous injection, the reagents mix near the tip and exit as a hot, hyperosmolar salt solution. Thermocouple is not yet positioned.

and surgical exposure of the liver via midline laparotomy as shown in **Figure B.1B**, intraoperative ultrasound was used to guide device placement into the liver at least 1 cm away from major vessels. Ultrasound imaging at 10 MHz was performed using a Z.one Ultra System (Zonare Medical Systems, Inc., Mountain View, CA). Euthanasia was accomplished with pentobarbital/phenytoin 0.2 mg/kg IV.

Temperature measurement

A 23G thermocouple (Physitemp type T MT_23/3, Physitemp Instruments, Clifton, NJ, USA) was inserted parallel to the injection device under ultrasound guidance at a distance of approximately 5 mm prior to injections to the same depth. Temperature data were recorded with a T-type thermocouple (Digi-Sense, Cole-Palmer Instrument Co., Vernon Hills, IL, USA).

Ablation experiments

Injections were maintained at a constant rate via syringe pump (Standard Infusion Only Harvard Pump 11 Plus Dual Syringe Pump, Harvard Apparatus, Holliston, Massachusetts), and performed at combined total infusion rates of 4 ml/min. One injection was performed per lobe of liver thus avoiding cross contamination issues. Volumes of reagents were equal with 0.5, 1.0, and 2.0 mL of each for combined totals of 1.0, 2.0, and 4.0 mL. Concentrations used were 5, 10, and 15 mol/L according to the array shown in **Table B.1**. In each of the 12 animals, all four injections were identical (i.e. one animal per position on the 3x3 matrix with 3 additional animals in the center

15 M	1	1	1
10 M	1	1+3	1
5 M	1	1	1
Molarity			
Total Volume	**1 mL (0.5/0.5)**	**2 mL (1/1)**	**4 mL (2/2)**

Table B.1. 3x3 element matrix of overall experimental design and conditions with number of animals indicated per condition. Three additional animals at the center of the grid were included for statistical comparisons across all positions for a total of 12 animals. Concentration of reagents is expressed in moles/liter and combined total volumes injected are shown with component breakdown in parentheses. Thus for 1 mL volumes as an example, 0.5 mL each of acid and base were used.

location) resulting in a total of 48 injections. Hemostasis at the conclusion of each injection after device removal was obtained by inserting a piece of spaghetti into the tract. This also served a secondary purpose as a tract marker(30). Heart rate was monitored continuously and recorded at 30-second intervals for 5-10 minutes for each injection. At sacrifice livers were harvested followed by fixation in 10% neutral buffered formalin and sectioning.

Gross pathology

Gross images of 2mm thick sectioned specimens capturing the entirety of a single ablation along with a ruler were obtained. These images were magnified in ImageJ (NIH) and the line tool was used for a 1cm calibration for conversion to pixel distances. Two independent observers (MGG and MMS) obtained tracings of the coagulated regions to allow measurement of the perimeter and area of each slice of the total ablation. Outer margins were used for measurement, but transition zones were generally very narrow (<2mm) and clearly demarcated between affected and unaffected tissues. The area and perimeter were then used with slice thickness to calculate the volume for each slice, the summation for the total lesion volume, the 3-D surface area, and sphericity for each treatment. Data are reported in accordance with the Society of Interventional Radiology Reporting Standards [31,32].

Sphericity calculations

Sphericity was calculated using the following formula:

$\Psi = (\pi^{1/3}(6V_p)^{2/3})/A_p$ where V_p = Volume and A_p = surface area

Values less than 1 correlate with the degree of deviation away from an ideal sphere.

Histology

Formalin-fixed specimens were processed and embedded into paraffin, sectioned at 5 microns and stained with hematoxylin and eosin. Light microscopy was used to assess the effects of the various treatments. Approximately 1.5 cm x 1cm sections were taken from central and margin zones of each sample.

Statistical Analysis

Outcomes including ablation volume, sphericity, and temperature, were measured. The variance-covariance structure was compound symmetry. P values were adjusted by Tukey's method. Inter-observer agreement on ablation volume and sphericity by two observers was evaluated using intraclass correlation coefficients (ICC) from general linear models for split-plot design, with lesions from the same animal as the whole-plot experiment units and observer as the split-plot factor. All analyses were conducted in SAS 9.2 (SAS Institute Inc., Cary, NC, USA). A p-value of less than 0.05 indicated significance.

B.3. RESULTS

Temperatures in vivo

Average peak temperatures shown in **Table B.2** arrayed according to the matrix in **Table B.1** for ease of comparison. The peak temperature observed was 105°C using 15 mol/L reagents. The highest average temperature was likewise seen with this concentration, at 91°C. At 5 mol/L the temperature increase was relatively low, averaging less than 10°C above body temperature with minimal range in the observed values. The intermediate concentration, 10 mol/L, showed an increase of approximately 15-16°C. In one 10 mol/L trial at just 0.5 mL the peak recorded temperature was 74.7°C. Average temperatures in general changed little by increasing the volume.

Histopathology

Figure B.2 shows the results from a single experiment using 0.5 mL of each reagent for a combined total volume of 1 mL injected. In this instance the middle concentration was employed (10 mol/L). **Figure B.3** is a representative section of the histology showing the pattern of damage and the distribution. At all concentrations, ablated regions consisted of coagulative necrosis and central lytic necrosis. Tissue architecture and cellular outlines were preserved in regions of coagulative necrosis, with loss of cytoplasmic and nuclear detail. Lytic necrosis, defined as loss of tissue architecture and cellular structure extending in some cases to gross cavitation, varied by treatment, but was most prominent in 10 mol/L and 15 mol/L groups. Ablated regions were generally surrounded by congestion and hemorrhage. This was mild to moderate at the ablated margin, and did not extend more than 2-4 mm into surrounding tissue.

15 M	55.6 ± 6.5 (71.3)	91.0 ± 6.5 (105.0)	82.1 ± 3.2 (90.8)
10 M	61.0 ± 6.6 (74.7)	53.6 ± 2.6 (72.3)	55.0 ± 5.0 (66.7)
5 M	43.5 ± 2.6 (48.7)	48.7 ± 1.9 (53.8)	49.7 ± 2.5 (56.6)
Molarity/Volume	**1 mL**	**2 mL**	**4 mL**

Table B.2. Average peak temperatures in ^{o}C ± SD with peak temperatures in parentheses (n=4 for all but 10M/2mL condition where n=16). Table corresponds to array in Table I for ease of comparison.

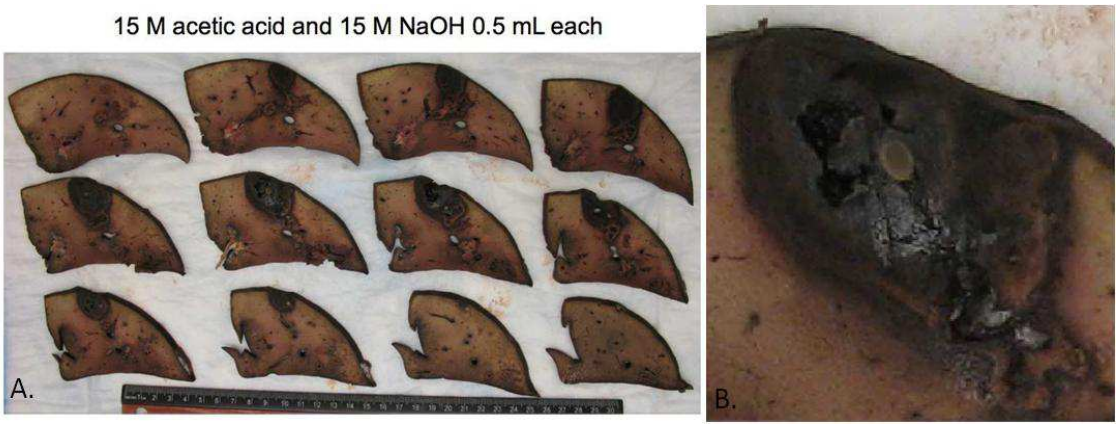

Figure B.2. Gross specimen of thermochemical ablation using 0.5 mL each of acetic acid and sodium hydroxide at 15 mol/L: A) formalin-fixed sections laid out adjacent with ruler, B) Magnified view of gross specimen, middle row, second from left. Pale ovoid central structure is a piece of spaghetti used to mark the tract and assist with hemostasis during the experiment. A charred appearance with some cavitation is evident.

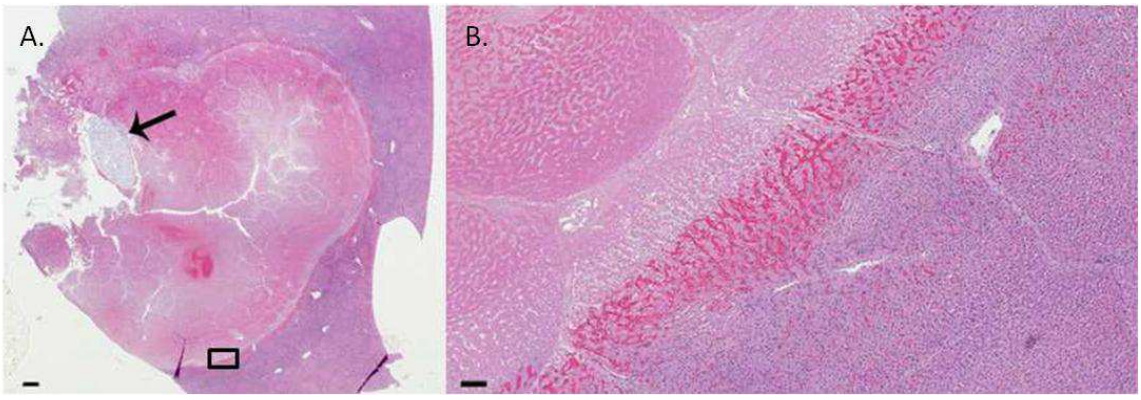

Figure B.3. Histopathology of a thermochemical lesion: A) Low magnification of representative ablation using 10 mol/L concentration of acid and base at 1 ml each. Lytic necrosis and cavitation are present immediately adjacent to the injection tract indicated by spaghetti (arrow) within a larger area of coagulative necrosis. B) Magnification of box (a) demonstrates coagulative necrosis (upper left), a well-demarcated hemorrhagic margin transitioning to congestion, and unablated tissue (lower right). H&E stain. A: 0.3x magnification, bar equals 1 mm. B: 5x magnification, bar equals 100 μm.

Volume and Shape Relationships

Table B.3 shows the sphericity values obtained under each condition. **Table B.4** delineates the coagulation volumes that were obtained according to concentration and volume. Data in each case are presented with standard deviations. Note that the central position of the matrix shown in **Table B.1**, with 4 animals and factoring in 4 injections per animal, accounts for 16 observations at this condition (10 mol/L and 2 mL total injection volume).

Physiology

Heart rate data are listed in **Table B.5**, reported as the maximum observed changes with standard deviations from the start of each injection. In two injections out of the total of 48 (one at 10 M/4mL and one at 15 M/1mL) bradycardia with brief transient hypotension was observed. These both spontaneously resolved within 60 seconds and no treatment was administered in response (data not shown). Overall, there was no clear relationship between either volume or concentration and changes in heart rate.

B.4. DISCUSSION

Reagents chosen were based on prior reports and ex vivo experience [29]. In addition, sodium acetate, which is the salt produced in this reaction, is readily converted to CO_2 [33]. Volumes employed were a conservative estimate since the physiologic tolerance to the technique was unknown. The thermocouple used served as a monitoring device but a

15 M	0.87 ± 0.07	0.85 ± 0.04	0.85 ± 0.02
10 M	0.93 ± 0.01	0.85 ± 0.02	0.91 ± 0.04
5 M	0.88 ± 0.01	0.91 ± 0.02	0.83 ± 0.02
Molarity/Volume	**1 mL**	**2 mL**	**4 mL**

Table B.3. Sphericity coefficients ± SD across conditions (n=4 for all but 10M/2mL condition where n=16). Table corresponds to array in Table I for ease of comparison.

15 M	8.92 ± 2.08	9.06 ± 1.12	10.68 ± 2.09
10 M	3.16 ± 0.21	8.55 ± 0.84	14.72 ± 1.42
5 M	2.95 ± 0.29	2.18 ± 0.08	4.11 ± 1.38
Molarity/Volume	**1 mL**	**2 mL**	**4 mL**

Table B.4. Volumes of coagulation ± SD obtained across conditions (n=4 for all but 10M/2mL condition where n=16). Table corresponds to array in Table 1 for ease of comparison.

15 M	8.8 ± 9.9	10.0 ± 3.5	-0.8 ± 2.2
10 M	10.5 ± 6.5	15.2 ± 5.7	11.3 ± 26.3
5 M	-0.3 ± 2.1	-0.5 ± 0.5	3.5 ± 5.3
Molarity/Volume	**1 mL**	**2 mL**	**4 mL**

Table B.5. Average maximum observed change in heart rate (from start of each ablation) ± SD observed across conditions (n=4 for all but 10M/2mL condition where n=16). Table corresponds to array in Table I for ease of comparison.

more comprehensive picture would be provided by thermography. Bearing this in mind, higher temperatures were generally obtained at a constant volume as concentration was increased. Both the highest peak and average temperatures were obtained with the highest concentration used. This is consistent with data reported in a gel phantom by Freeman et al [34]. The highest temperature, 105°C, was observed with 15 mol/L reagents. By comparison, maintaining a constant concentration of the reagents and increasing the volume injected did not make a large difference in the temperature. At histology, ablated regions identified grossly were confirmed via examination of H&E stained sections. Tissue architecture is more frequently preserved at lower concentration, and there was a tendency to less cavitation with 5 mol/L treatment. If lower concentrations are sufficient for cell death, the potential with the lower dose for systemic exposure could be decreased. Although mild to moderate congestion was noted in the immediate ablation margin, vascular damage outside the immediate ablation zone was not noted in this study.

Relationships among total injected volumes to final volumes for the zones of coagulation were not straightforward. The lowest concentration, 5 mol/L produced similar results across all of the volumes injected with no apparent relationship to the amount injected. The largest coagulation volume observed in this study was not obtained using the highest concentration as might be initially expected (i.e. the ‘strongest’ conditions), but rather at the midpoint for concentration (10 mol/L). The coagulation volumes obtained using 15 mol/L reagents did not vary a great deal, similar in this respect to the results observed at 5 mol/L. Shape analysis revealed no drop in sphericity

with increases in volume injected. This was somewhat unexpected since the prototype device was essentially a point source situated in a complex, heterogeneous environment. The rate of injection was established at 4 mL/minute based on prior studies suggesting this would be an adequate rate to generate a detectable amount of heat energy released. This corresponds to 0.07 mL/sec, which is within the range reported with ethanol in which shape distortion was noted with increasing injection rates greater than 0.4 mL/sec [35]. Comparison is limited, however, as the study with ethanol utilized ex vivo tissue, injection was done manually, and volume was limited to 1 mL.

The difference between chemical ablation alone with acetic acid and using the reagent in thermochemical ablation deserves further comment. In a particularly pointed example, a volume of 11.9 mL of coagulum was obtained in thermochemical ablation with only 0.5 mL of 15 mol/L acetic acid when combined with base. This is noteworthy from the standpoint that the coagulum volume is nearly 24 times the amount of the acid that was injected. This represents a very high ratio of coagulum to reagent volume and becomes yet more interesting if one considers that the product in the tissues is merely sodium acetate rather than acetic acid. The use of 0.5 mL of 50% acetic acid alone, in contrast, would be expected to produce a volume of 1.5 mL of coagulum [11]. This is substantially smaller than the volume obtained with thermochemical ablation using this amount of acid when mixed with the base.

The injections were tolerated well in general with no statistical correlation between

the changes observed in vital signs and either concentration or volume of injected reagents. All 12 animals survived until the completion of the planned series of treatments for each, allowing collection of a complete data set for all animals. In two cases of bradycardia with hypotension, these were followed by tachycardia with hypertension that declined over the observation period. Since both resolved without any intervention, and the animals in each case went on with the remainder of the assigned injections without further incident, we believe that these may have been vagal responses with subsequent rebound. These responses were not seen at the most extreme conditions in which the largest total volumes (4 mL) and the highest concentration (15 mol/L) were employed. The total dose with 4 injections using 2 mL of acid each was therefore 8 mL of 15 mol/L acid. Given that 50% acetic acid corresponds to concentration of approximately 8.5 mol/L, the equivalent total amount of 50% acetic aid would be approximately 14 mL in a single setting. This is above the range reported in most human studies for a single treatment [11].

Temperature excursions likely play a role in the outcome despite the fact that they are both relatively brief and that the recorded temperatures were obtained within a short distance (several mm at most) of the tip of the device. Combination effects of temperature and other conditions, such as osmolarity, are thought to contribute to the final result. A 2.5 molar salt product solution, the lowest tested, is 5 osmolar. This is well above the normal physiologic range of just 270-300 milliosmolar. This underscores that that local hyperosmolarity is therefore a potential avenue for destruction of the tissues.

The procedure causes an abrupt change in concentration in the local environment that is an order of magnitude or more in size. In the extreme case tested at 15 mol/L, the final salt concentration was 7.5 mol/L. Accounting for the binary nature of the salt and placing this in units for easy physiologic comparison, this is 15,000 milliosmolar. The composition of individual salts can also affect the propensity to denature tissues, with some salts more prone to cause denaturation than others [36,37]. A more detailed discussion of the mechanism of action regarding denaturation is beyond the scope of this discussion but there is clearly potential for more work on this issue.

The study had a number of limitations. An unrefined, prototype device was used in an acute setting using healthy pigs, which differs from actual conditions in a tumor. As noted earlier, however, models of cirrhosis in pigs with tumor are not readily available. A single thermocouple was employed for temp measurements giving a limited perspective on the temperature change and the distribution of the change in tissue. Future work will address some of these issues with detailed temperature studies using thermography, demonstration in an animal tumor model, and in vitro studies to elucidate the mechanisms of action.

We conclude that the procedure was well tolerated in the acute setting even at the highest dose. Sphericity of the resulting lesions overall was relatively preserved and the volumes were substantially larger than the predicted amount if acetic acid were to be used as a single agent for ablation [11]. Peak temperatures at intermediate and high

concentrations were readily achieved and exceeded the threshold required for coagulation of tissues from hyperthermia. Increasing the reagent concentrations and volumes did increase the amount of the coagulum obtained but not in a simple linear fashion. Further work to delineate the mechanism of action and the time course are warranted.

B.5. ACKNOWLEDGEMENTS

University of Minnesota Department of Radiology

This work was supported in part by NIH 1R21CA133263-01 and NIH P30 CA77598 utilizing the following Masonic Cancer Center, University of Minnesota shared resource: Biostatistics and Bioinformatics Core. We also thank Mr. Bill Gallagher for assistance with animal preparation, and Dr. Afshin Divani for the use of ultrasound equipment. Finally, we thank Dr. Jared Verdoorn, Dr. Reza Talaie, Dr. Joseph Farnam, Ms. Rina Farah and Dr. Anthony Zbacnik for assistance with data collection.

B.6. REFERENCES

1. Kuo YH, Lu SN, Chen CL, Cheng YF, Lin CY, Hung CH, et al. Hepatocellular carcinoma surveillance and appropriate treatment options improve survival for patients with liver cirrhosis. Eur J Cancer 2010 Mar;46(4):744-751.
2. Schumacher PA, Powell JJ, MacNeill AJ, Buczkowski AK, Erb SR, Ho SG, et al. Multimodal therapy for hepatocellular carcinoma: a complementary approach to liver transplantation. Ann Hepatol 2010 Jan-Mar;9(1):23-32.
3. Cabibbo G, Enea M, Attanasio M, Bruix J, Craxi A, Camma C. A meta-analysis of survival rates of untreated patients in randomized clinical trials of hepatocellular carcinoma. Hepatology 2010 Apr;51(4):1274-1283.
4. Rimassa L, Santoro A. Sorafenib therapy in advanced hepatocellular carcinoma: the SHARP trial. Expert Rev Anticancer Ther 2009 Jun;9(6):739-745.
5. Llovet JM, Ricci S, Mazzaferro V, Hilgard P, Gane E, Blanc JF, et al. Sorafenib in advanced hepatocellular carcinoma. N Engl J Med 2008 Jul 24;359(4):378-390.

6. Lee WJ, Lee JL, Chang SE, Lee MW, Kang YK, Choi JH, et al. Cutaneous adverse effects in patients treated with the multitargeted kinase inhibitors sorafenib and sunitinib. Br J Dermatol 2009 Nov;161(5):1045-1051.
7. Dhanasekaran R, Kooby DA, Staley CA, Kauh JS, Khanna V, Kim HS. Comparison of conventional transarterial chemoembolization (TACE) and chemoembolization with doxorubicin drug eluting beads (DEB) for unresectable hepatocelluar carcinoma (HCC). J Surg Oncol 2010 May 1;101(6):476-480.
8. Raoul JL, Sangro B, Forner A, Mazzaferro V, Piscaglia F, Bolondi L, et al. Evolving strategies for the management of intermediate-stage hepatocellular carcinoma: Available evidence and expert opinion on the use of transarterial chemoembolization. Cancer Treat Rev 2010 Aug 17.
9. Kooby DA, Egnatashvili V, Srinivasan S, Chamsuddin A, Delman KA, Kauh J, et al. Comparison of yttrium-90 radioembolization and transcatheter arterial chemoembolization for the treatment of unresectable hepatocellular carcinoma. J Vasc Interv Radiol 2010 Feb;21(2):224-230.
10. Ibrahim SM, Lewandowski RJ, Sato KT, Gates VL, Kulik L, Mulcahy MF, et al. Radioembolization for the treatment of unresectable hepatocellular carcinoma: a clinical review. World J Gastroenterol 2008 Mar 21;14(11):1664-1669.
11. Clark TW. Chemical ablation of liver cancer. Tech Vasc Interv Radiol 2007 Mar;10(1):58-63.
12. Clark TW, Soulen MC. Chemical ablation of hepatocellular carcinoma. J Vasc Interv Radiol 2002 Sep;13(9 Pt 2):S245-52.
13. Boutros C, Somasundar P, Garrean S, Saied A, Espat NJ. Microwave coagulation therapy for hepatic tumors: review of the literature and critical analysis. Surg Oncol 2010 Mar;19(1):e22-32.
14. Kudo M. Radiofrequency ablation for hepatocellular carcinoma: updated review in 2010. Oncology 2010 Jul;78 Suppl 1:113-124.
15. Cho YB, Lee KU, Suh KS, Kim YJ, Yoon JH, Lee HS, et al. Hepatic resection compared to percutaneous ethanol injection for small hepatocellular carcinoma using propensity score matching. J Gastroenterol Hepatol 2007 Oct;22(10):1643-1649.
16. Fartoux L, Arrive L, Andreani T, Serfaty L, Chazouilleres O, Tubiana JM, et al. Treatment of small hepatocellular carcinoma with acetic acid percutaneous injection. Gastroenterol Clin Biol 2005 Dec;29(12):1213-1219.
17. Tsai WL, Cheng JS, Lai KH, Lin CP, Lo GH, Hsu PI, et al. Clinical trial: percutaneous acetic acid injection vs. percutaneous ethanol injection for small hepatocellular carcinoma--a long-term follow-up study. Aliment Pharmacol Ther 2008 Aug 1;28(3):304-311.
18. Schoppmeyer K, Weis S, Mossner J, Fleig WE. Percutaneous ethanol injection or

percutaneous acetic acid injection for early hepatocellular carcinoma. Cochrane Database Syst Rev 2009 Jul 8;(3)(3):CD006745.

19. Germani G, Pleguezuelo M, Gurusamy K, Meyer T, Isgro G, Burroughs AK. Clinical outcomes of radiofrequency ablation, percutaneous alcohol and acetic acid injection for hepatocelullar carcinoma: a meta-analysis. J Hepatol 2010 Mar;52(3):380- 388.
20. Bouza C, Lopez-Cuadrado T, Alcazar R, Saz-Parkinson Z, Amate JM. Meta-analysis of percutaneous radiofrequency ablation versus ethanol injection in hepatocellular carcinoma. BMC Gastroenterol 2009 May 11;9:31.
21. Mahnken AH, Bruners P, Gunther RW. Local ablative therapies in HCC: percutaneous ethanol injection and radiofrequency ablation. Dig Dis 2009;27(2):148-156.
22. Lencioni R, Crocetti L, Cioni D, Pina CD, Oliveri F, De Simone P, et al. Single session percutaneous ethanol ablation of early-stage hepatocellular carcinoma with a multipronged injection needle: results of a pilot clinical study. J Vasc Interv Radiol 2010 Oct;21(10):1533-1538.
23. Kuang M, Lu MD, Xie XY, Xu HX, Xu ZF, Liu GJ, et al. Ethanol Ablation of Hepatocellular Carcinoma Up to 5.0 cm by Using a Multipronged Injection Needle with High-Dose Strategy. Radiology 2009 Aug 25.
24. Ho CS, Kachura JR, Gallinger S, Grant D, Greig P, McGilvray I, et al. Percutaneous ethanol injection of unresectable medium-to-large-sized hepatomas using a multipronged needle: efficacy and safety. Cardiovasc Intervent Radiol 2007 Mar-Apr;30(2):241-247.
25. Arnulf F, Monika S, Herwig S, Monika H, Johannes PD, Gregor U, et al. Atropine for prevention of cardiac dysrhythmias in patients with hepatocellular carcinoma undergoing percutaneous ethanol instillation: a randomized, placebo-controlled, doubleblind trial. Liver Int 2009 May;29(5):715-720.
26. Burton KR, O'Dwyer H, Scudamore C. Percutaneous ethanol ablation of hepatocellular carcinoma: periprocedural onset alcohol toxicity and pancreatitis following conventional percutaneous ethanol ablation treatment. Can J Gastroenterol 2009 Aug;23(8):554-556.
27. Sidi A, Naik B, Urdaneta F, Muehlschlegel JD, Kirby DS, Lobato EB. Treatment of ethanol-induced acute pulmonary hypertension and right ventricular dysfunction in pigs, by sildenafil analogue (UK343-664) or nitroglycerin. Ann Card Anaesth 2008 Jul-Dec;11(2):97-104.
28. Sidi A, Naik B, Muehlschlegel JD, Kirby DS, Lobato EB. Ethanol-induced acute pulmonary hypertension and right ventricular dysfunction in pigs. Br J Anaesth 2008 Apr;100(4):568-569.
29. Farnam JL, Smith BC, Johnson BR, Estrada R, Edelman TL, Farah R, et al.

Thermochemical ablation in an ex-vivo porcine liver model using acetic acid and sodium hydroxide: proof of concept. J Vasc Interv Radiol 2010 Oct;21(10):1573-1578.

30. Okuda S, Kuroda K, Oshio K, Mulkern RV, Colucci V, Morrison PR, et al. MRbased temperature monitoring for hot saline injection therapy. J Magn Reson Imaging 2000 Aug;12(2):330-338.
31. Goldberg SN, Grassi CJ, Cardella JF, Charboneau JW, Dodd GD,3rd, Dupuy DE, et al. Image-guided tumor ablation: standardization of terminology and reporting criteria. J Vasc Interv Radiol 2009 Jul;20(7 Suppl):S377-90.
32. Mulier S, Ni Y, Frich L, Burdio F, Denys AL, De Wispelaere JF, et al. Experimental and clinical radiofrequency ablation: proposal for standardized description of coagulation size and geometry. Ann Surg Oncol 2007 Apr;14(4):1381-1396.
33. Tsai IC, Huang JW, Chu TS, Wu KD, Tsai TJ. Factors associated with metabolic acidosis in patients receiving parenteral nutrition. Nephrology (Carlton) 2007 Feb;12(1):3-7.
34. Freeman LA, Anwer B, Brady RP, Smith BC, Edelman TL, Misselt AJ, et al. In vitro thermal profile suitability assessment of acids and bases for thermochemical ablation: underlying principles. J Vasc Interv Radiol 2010 Mar;21(3):381-385.
35. Tapani E, Vehmas T, Voutilainen P. Effect of injection speed on the spread of ethanol during experimental liver ethanol injections. Acad Radiol 1996;3(12):1025-1029.
36. Shimizu S, McLaren WM, Matubayasi N. The Hofmeister series and protein-salt interactions. J Chem Phys 2006;124:234905.
37. Zhang Y, Cremer PS. Interactions between macromolecules and ions: the Hofmeister series. Curr Opin Chem Biol 2006;10(6):658-663.

Appendix C

Use of Tumor Necrosis Factor–alpha-coated Gold Nanoparticles to Enhance Cryoablation in a Translational Model of Renal Tumors

This chapter describes investigations involving nanoparticle preconditioning to enhance cryoablation in a translational tumor model.

C.1. INTRODUCTION

With the increased utilization of cross-section imaging modalities such as computed tomography and magnetic resonance imaging, renal masses are now diagnosed at an early stage and small size [1]. With this migration towards smaller tumor size, tumor treatment has changed as well. Minimally invasive techniques such as cryoablation have offered reduced morbidity, shorter duration of hospitalization, shorter convalescence, and greater preservation of renal function [2]. However, this procedure whether performed percutaneously or laparoscopically has limitations. It is well established that tissue at the edge of the cryoablation ice ball will not be killed but instead will only be injured by the cryoablation. The true kill zone (region where all cells are killed) resides within the ice ball at lower temperatures. Clinicians compensate for this "transition zone" between the kill zone and the edge of the ice ball by pushing the edge of the ice ball well beyond the tumor (**Figure C.1**). While this has been effective for treatment of select patients, this technique not only results in unnecessary damage to normal renal parenchyma, but may potentially limit the number of patients that are candidates for this procedure as other vital structures such as ureter and intestine need to be a significant distance away from the ablation. Finally, there can be a significant rate of incomplete ablation of up to 12.5%, reported [3]. This has been attributed to incomplete kill of tumor within the ice ball formed during ablation [3].

In order to address these issues, researchers have attempted to augment tumor cell

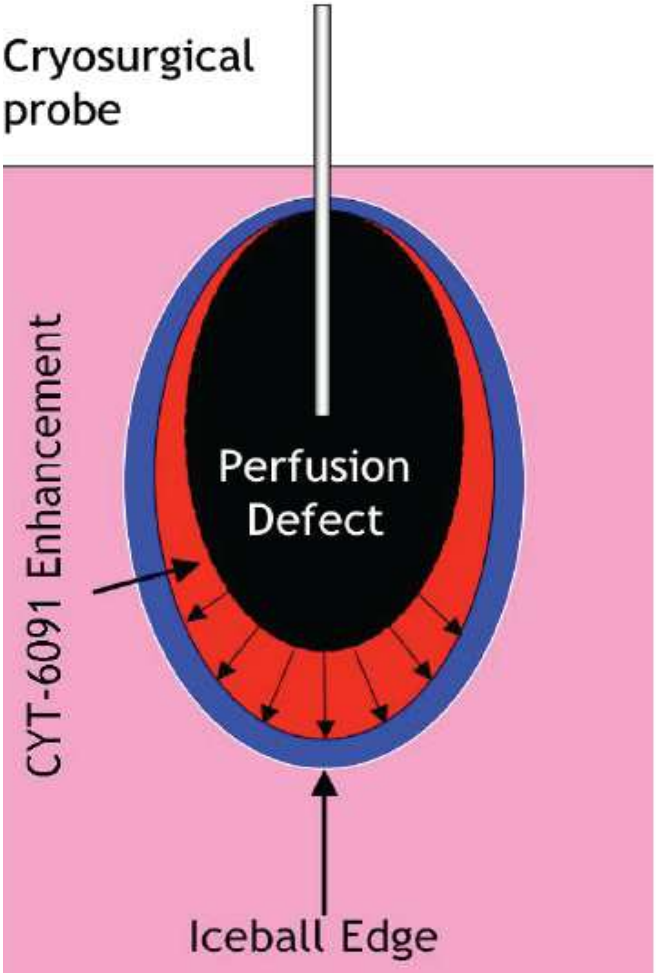

Figure C.1. Schematic of TNF-α nanoparticle (CYT-6091) enhancement of cryosurgical injury by extending it to the edge of the iceball volume.

death following cryoablation therapy by administering a variety of different adjuvant medication including antifreeze proteins, chemotherapeutics, etc [4, 5]. One promising agent that has been identified is the multifunctional cytokine tumor necrosis factor alpha (TNF-α). Unfortunately the use of TNF-α has been limited by toxic systemic side effects. To overcome this, Paciotti et al. described a colloidal gold nanoparticle coated with TNF-α (CYT-6091) as a standalone solid cancer therapy. The nanoparticle delivery system serves to deliver a large percentage of TNF-α within the tumor thus minimizing systemic side effects [6]. Our purpose with this study was to determine if a TNF-α coated nanoparticle (CYT-6091) could enhance and enlarge a cryoablation lesion while avoiding systemic toxicity.

C.2. MATERIALS AND METHODS

VX2 tumor implantation

After approval from our institutional IACUC was obtained twenty New Zealand female rabbits weighing 2.2-2.7 kg were implanted with VX2 tumor by the following procedure. The animals were first anesthetized with an intramuscular injection of a cocktail solution containing ketamine (40 mg/kg), xylazine (5 mg/kg) and acepromazine (1 mg/kg). The animals were subsequently intubated and maintained on anesthesia for the surgical procedure by administering 0.75% isoflurane along with 1L/min of oxygen. Standard perioperative monitoring was performed. A midline abdominal incision was made and both kidneys were exposed. A 1 mm^3 piece of VX2 tumor was then implanted in the

subcapsular region of the lower pole in both kidneys. The tumors were allowed to grow for 14 days before injection of CYT-6091 and cryoablation of the renal tumor. The animals were weighed prior to implantation of the tumor, as well as prior to cryoablation, and necropsy. Following implantation of tumor, the rabbits were randomly assigned to one of two groups: TNF-α nanoparticle plus cryoablation (CYT-6091 group) or cryoablation alone group. There were 10 rabbits in each group.

TNF-α coated Nanoparticle

CYT-6091 (Cytimmune Sciences Inc., Rockville, MD) is a suspension of colloidal gold nanoparticles (average diameter = 33 nm) to which TNF-α and thiol-derivatized polyethylene glycol are covalently bonded.9 For the 10 rabbits in the CYT-6091 group, CYT-6091 was given at a dose of 200 microgram/kg intravenously four hours before the cryoablation procedure. Rabbits in the cryoablation alone group did not receive CYT-6091 or any placebo.

Cryoablation

All 20 rabbits from both the CYT-6091 and cryoablation alone groups received identical cryoablation procedures. The cryoablation was performed after induction and maintenance of anesthesia as described above. The midline incision was re-entered and the renal tumor mass was isolated from the surrounding tissue. The Seednet system (Galil Medical Inc., Yokneam, Israel) was used with 1.58mm diameter cryoprobes (IceRod^{TM}, 15mm active region at tip). Thermocouples of 1.58mm diameter were inserted under

ultrasound guidance (Ultramark 9.0 with 10 Mhz probe, Advanced technology laboratories Inc, WA, USA). A thermocouple was placed at the visible edge of the tumor at a depth of 4mm from the surface. Then a cryoprobe was placed 5mm away from the thermocouple at a depth of 8 mm from the surface. A plexiglas jig was used for accurate placement of the probes (**Figure C.2**). Experiments done on phantom models in our laboratory demonstrated that the maximum diameter of the iceball was obtained at 4mm proximally from the tip of the probe. The cryoablation was delivered until the thermocouple recorded a temperature of 0^{o}C. The tumor was subsequently thawed to room temperature passively. This was followed by another similar freeze-thaw cycle. The probe tracts were marked by placing a 2.0 PROLENE polypropylene suture (Ethicon Inc., Piscataway, NJ) in the tract.

Post ablation monitoring and Histologic Analysis

From the injection of CYT-6091 through the perioperative period following the cryoablation procedure, the blood pressure, oxygen saturation, and temperature were monitored. Subsequently, the rabbits were checked daily for signs of malaise, poor appetite, low activity level, respiratory difficulty, or other signs of systemic illness. Post operative monitoring was done with the intent of identifying side effects caused by CYT-6091. The animal was then weighed and necropsy was performed 7 days after the procedure with full examination of the animal for metastatic disease.

Treated kidneys were placed in formalin overnight for partial fixation prior to

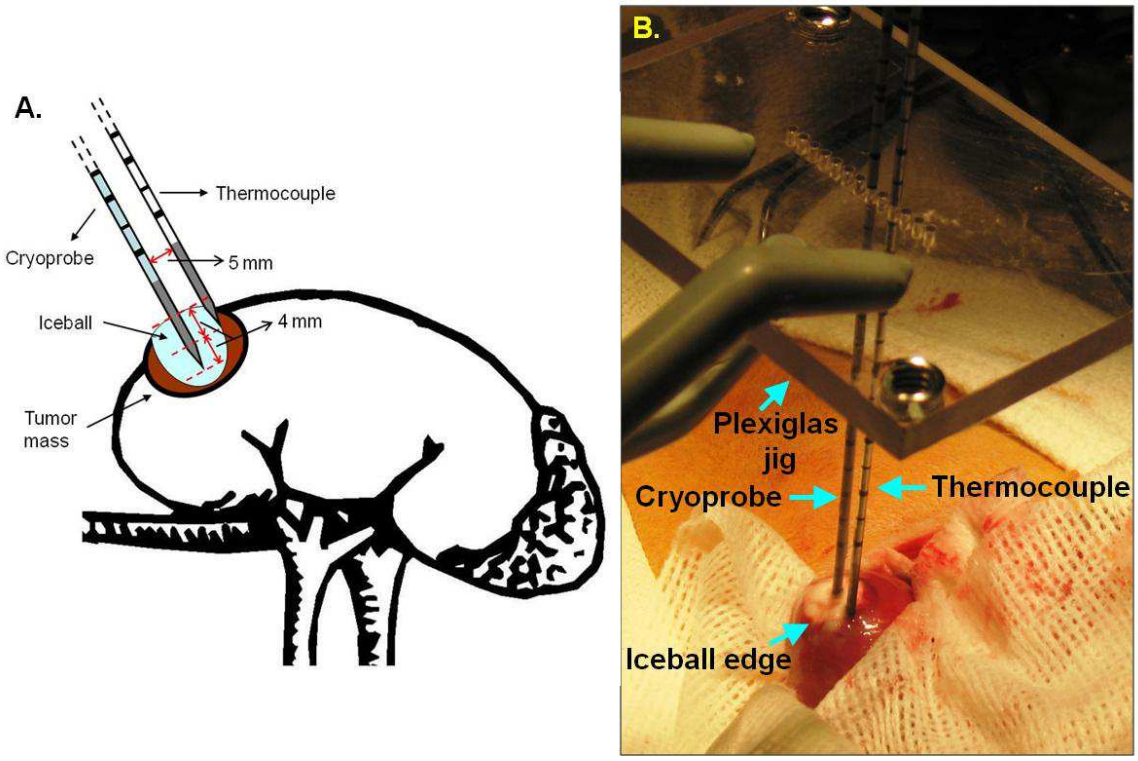

Figure C.2. A. Schematic of the placement of cryoprobe and thermocouple in relation to the tumor. B. Plexiglas jig is used for accurate placement of cryoprobe and thermocouple within the tumor during the cryoablation procedure.

sectioning. Sectioning was done at 3mm intervals in the plane perpendicular to the path of the probe tracts. Probe tracts were identified by the previously placed PROLENE polypropylene suture. After sectioning, the probe tracts were marked using tissue marking dyes. Tissue sections underwent standard histological processing with hematoxylin and eosin staining. The slides were scanned at a magnification of 20X using an Aperio scanscope CS scanner (Aperio Technologies, CA). All measurements were made by two blinded observers in the second section which is at a depth of 6 mm from the cortical surface. The zones of complete necrosis were measured from the centre of cryoprobe tract. The zone of complete necrosis was measured from the center of the cryoprobe to the first viable cell. The measurements were performed using Aperio Image scope software (v.9.0.19.1516). Two tailed student's 't' test and Fisher's exact test were conducted to determine statistical significance between different groups; $P < 0.05$ was considered significant.

C.3. RESULTS

All rabbits tolerated injection of CYT-6091 without signs of systemic complications. There were no large changes in blood pressure or temperature. Additionally, there was no subjective difference between the two groups in post-cryoablation activity level or recovery. Post-cryoablation weight loss was not significantly different between the two groups (0.30 ± 0.08 kg CYT-6091 group, 0.35 ± 0.05 kg cryoablation alone group, $P = 0.11$) (**Table C.1**).

Outcome measure	Cryo alone	Cryo + CYT-6091	*P* value
Number of animals developing metastases	8	1	0.04
Diameter of zone of complete necrosis	7.05 ± 1.60 mm	6.31 ± 1.38 mm	0.14
Post ablation weight loss	0.30 ± 0.08 kg	0.35 ± 0.05 kg	0.11

Table C.1. Summary of results comparing the cryoablation only and the cryoablation + CYT-6091 groups (number of animals = 10 for each group)

Macroscopic Findings

Kidneys harvested at Day 7 after treatment with cryoablation alone or with CYT-6091 preadministration had pale ellipse-shaped ablation areas that were distinct from surrounding normal renal parenchyma. The thermocouple and cryoprobe tracts were clearly identifiable (**Figure C.3A**). Preliminary experiments conducted with kidneys harvested at Day 3 after cryoablation revealed pulpy edematous lesions that could not be sectioned uniformly for histological analysis even after formalin fixation, thus the kidneys in the current study were harvested at Day 7 after treatment. A significant difference was obtained in the rate of peritoneal metastases between the two treatment groups. Peritoneal metastasis was characterized by numerous tumor nodules (< 1 mm diameter) present in the peritoneal cavity including the surface of the intestines. 8 out of 10 cases in the cryoablation alone group developed peritoneal metastases, while only 1 out of 10 cases in the cryoablation plus CYT-6091 group developed metastasis ($P = 0.04$) (**Table C.1**).

Microscopic Findings

Histological analysis revealed an area of coagulative necrosis immediately adjacent to the cryoprobe tract. In general, the region of coagulative necrosis was characterized by cell debris with a dominant eosinophilic staining pattern with distorted tumor cells having small dense nuclei with no discernible chromatin structure (**Figure C.3**). Inflammatory cells were present in a diffuse band between the zone of coagulative necrosis and viable tumor tissue. However there was no consistency in the shape or size of the lesions among

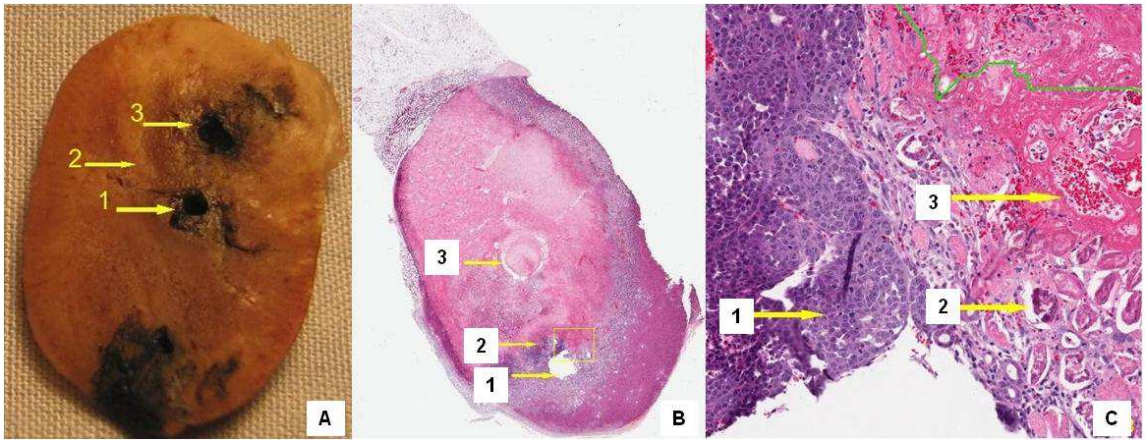

Figure C.3. (A) Kidney section after fixing in formalin marked with India ink. 1. edge of the cryolesion, 2. thermocouple tract, 3. cryoprobe tract. (B) H&E staining of the ablation area. 1. thermocouple tract, 2. transitional zone consisting of viable and necrotic tumor cells, 3. cryoprobe tract. (C) 20X magnification of transitional zone. 1. viable tumour cells, 2. transitional zone, 3. zone of complete necrosis.

sections within each treatment group. In several sections distinct tracts of viable tumor cells are seen infiltrating the cryolesion (**Figure C.4**). With a standardized cryoablation protocol, no significant difference was obtained between the mean diameters of complete necrosis in the CYT-6091 and cryoablation alone groups (6.31 ± 1.38 mm vs. 7.05 ± 1.60 mm, P=0.14).

C.4. DISCUSSION

Cryoablation has gained in popularity for treatment of renal tumors. To date, most work with cryoablation has occurred via a laparoscopic approach but recent studies have shown the feasibility of the less invasive percutaneous approach. While both of these techniques have been very successful at treating select tumors, the indications for cryoablation have been limited by two separate problems. First is a size limitation. Most series have limited tumor size to 4 cm or less. Second is the risk of injury to surrounding structures. The presence of residual viable tumour has been one of the major concerns with cryoablation. It was reported by Davol et al. that the need for salvage procedure in their series was 12.5% [3]. The intermediate-term (minimum 3-year follow-up) report of Gill et al updating their patient series reported that the positive biopsy rate was 5.6% and that residual radiographic lesions continued to decrease in volume over time [2]. In parallel to these clinical findings, several in vitro and in vivo studies have been conducted in order to elucidate the mechanisms of tissue destruction and cell death following cryoablation. Previous authors have found that for complete necrosis of renal tissue a temperature of

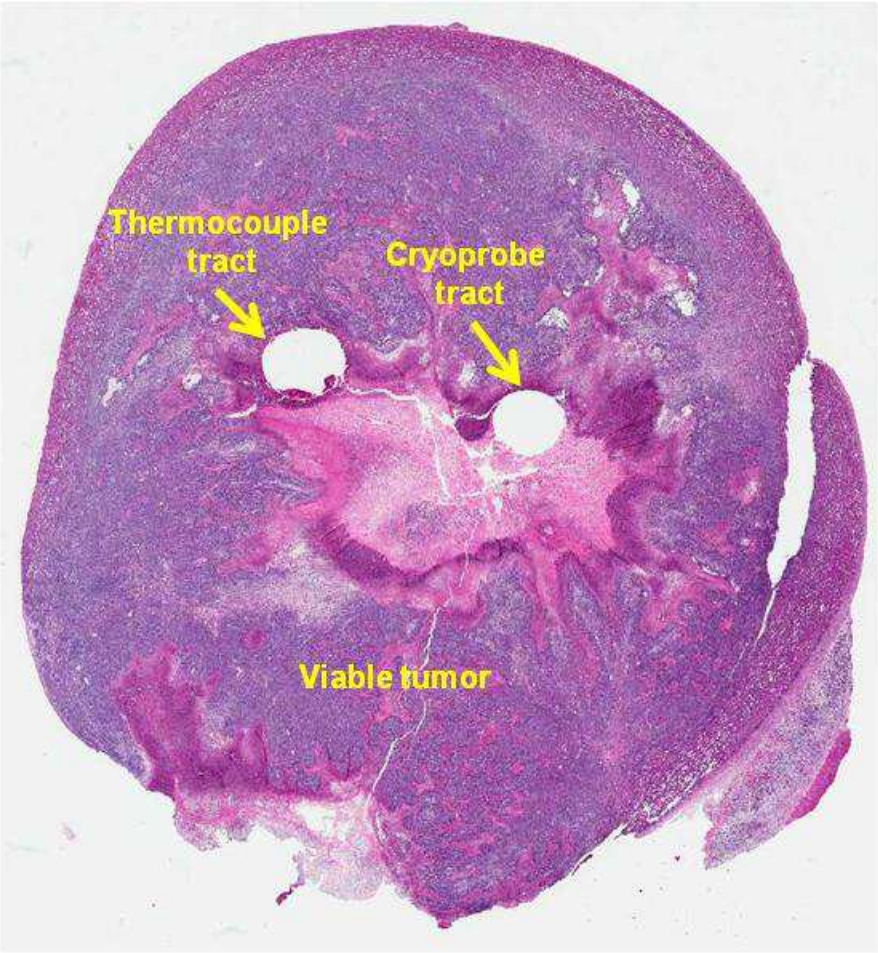

Figure C.4. H&E section of VX2 kidney tumor cryolesion on Day 7 after cryoablation showing regrowth of tumor into the lesion.

near -20^{o}C is needed and the area of total necrosis is about 3.1mm inside the edge of the iceball [7-9]. Most of the clinical protocols usually over-freeze the lesion so as to reduce the chance of tumor recurrence, thus rendering more damage to the surrounding normal parenchyma. This is highly undesirable, especially in deep and centrally located tumors. Since the ice formation during cryoablation lends itself to image contrast in the body, maximizing the tumor death inside the iceball will also ensure less collateral damage to adjacent structures, which are vital for kidney and prostate function, via real time imaging techniques (CT, MRI, US).

Adjunctive therapy to maximize the cancer cell death in cryosurgery has been attempted before. Researchers have used a combination of therapies like antifreeze proteins, hyperthermia, chemotherapeutics, etc [4, 10]. In this study we used a nanoparticle-based drug carrier as an adjuvant to increase the cryosensitivity within the periphery of the iceball (0 to -40^{o}C). Our efforts were directed to extend the edge of necrosis up to the periphery of the iceball which in turn spares the adjacent normal tissue. CYT-6091 is a multivalent drug that is assembled on 33-nm colloidal gold nanoparticles which sequester recombinant human TNF-α within solid tumors and subsequently incites inflammation [11, 12]. This utilizes the inherent leakiness of the tumor endothelium associated with relatively increased basal interstitial fluid pressure compared to normal tissues. CYT-6091 has been successfully used previously to augment cryo and RFA ablation in small animals [11, 12].

In our study, the VX-2 tumor was chosen so as to address the biggest issue with cryoablation of renal tumors i.e. tumor size. Although the VX2 tumor is derived from a papilloma instead of a renal cell carcinoma, it represents the largest animal model of a renal tumor available. A murine model with a renal cell carcinoma tumor was considered but the tumor volume would not have been large enough for the experiment. However, use of the VX2 tumor as a model for renal tumor cryoablation is fraught with difficulties as is apparent from the results of our study.

Previous work by Goel et al have shown that CYT-6091 preadministration retarded the growth of human prostate carcinoma cell line in a nude mouse [12]. Based on the results of our radiofrequency ablation study (see Chapter 4), the primary goal of the current study was to demonstrate a larger zone of tumor destruction with CYT-6091 preadministration compared to cryoablation alone. Ideally, the region of coagulative necrosis would have been evaluated at Day 3 after cryoablation when vascular events following the ablation would lead to the maximal extent of tumor necrosis before wound healing events kick in to reduce the size of the cryolesion [12]. However, the gross appearance and texture of the VX2 tumor after cryoablation precluded sectioning and any meaningful histologic analysis at Day 3. Instead the Day 7 timepoint after cryoablation was chosen to evaluate the impact of CYT-6091 preadministration. This facilitated gross sectioning and histological analysis of the cryolesion however the rapid growth kinetics of the VX2 tumor lead to tumor regrowth within the cryolesion thus severely confounding the results of the study [13].

Interestingly, our study revealed an unexpected finding in that we observed that CYT-6091 preadministration decreased the rate of metastasis following cryoablation. We believe that the reduced rate of metastasis in the drug group is due to a combination of the direct insult on the tumor and augmentation of cryoinjury. However the role of an augmented immune response cannot be discounted [14].

Based on our findings, a different experimental approach should be considered for demonstrating the impact of CYT-6091 preadministration on enhancing cryoablation in the VX2 kidney tumor model which takes into account the rapid growth kinetics of the tumor. A more aggressive freezing protocol similar to the one employed by Nakada et al with an experimental endpoint of disease-free status as opposed to region of tumor necrosis will likely yield results more in line with preclinical models [12, 15, 16].

C.5. REFERENCES

1. Luciani LG, Cestari R, and Tallarigo C: Incidental renal cell carcinoma-age and stage characterization and clinical implications: study of 1092 patients (1982–1997). Urology 56: 58–62, 2000.
2. Gill IS, Remer EM, Hasan WM, et al: Renal cryoablation: outcome at 3 years. J Urol 173: 1903–1907, 2005.
3. Davol PE, Fulmer BR, Rukstalis DB. Long-term results of cryoablation for renal cancer and complex renal masses. Urology. 2006 Jul;68(1 Suppl):2-6.
4. Pham L, Dahiya R, Rubinsky B. An in vivo study of antifreeze protein adjuvant cryosurgery. Cryobiology 1999;38:169–75.
5. Chao BH, He X, Bischof JC. Pre-treatment inflammation induced by TNF-a augments cryosurgical injury on human prostate cancer. Cryobiology 2004;49:10–27.
6. Paciotti GF, Myer L, Weinreich D, et al. Colloidal gold: a novel nanoparticle

vector for tumor directed drug delivery. Drug Deliv 2004;11: 169–83.
7. Rupp CC, Hoffmann NE, Schmidlin FR, Swanlund DJ, Bischof JC, Coad JE Cryobiology. Cryosurgical changes in the porcine kidney: histologic analysis with thermal history correlation. 2002 ;45:167-82.
8. Chosy SG, Nakada SY, Lee FT, et al: Monitoring renal cryosurgery: predictors of tissue necrosis in swine. J Urol 159: 1370–1374, 1998.
9. Campbell SC, Krishnamurthi V, Chow G, et al: Renal cryosurgery: experimental evaluation of treatment parameters. Urology 52: 29–33, 1998.
10. Hakimé A, Hines-Peralta A, Peddi H, Atkins MB, Sukhatme VP, Signoretti S, Regan M, Goldberg SN. Combination of radiofrequency ablation with antiangiogenic therapy for tumor ablation efficacy: study in mice. Radiology 2007;244:464-70.
11. Visaria R, Bischof JC, Loren M, Williams B, Ebbini E, Paciotti G, Griffin R. Nanotherapeutics for enhancing thermal therapy of cancer. Int J Hyperthermia. 2007 Sep;23(6):501-11
12. Goel R, Swanlund D, Coad J, Paciotti GF, Bischof JC TNF-alpha-based accentuation in cryoinjury--dose, delivery, and response. Mol Cancer Ther. 2007 Jul;6(7):2039-47
13. Aravalli RN, Golzarian J, Cressman EN. Animal models of cancer in interventional radiology. Eur Radiol. 2009 May;19(5):1049-53.
14. Sabel MS. Cryo-immunology: a review of the literature and proposed mechanisms for stimulatory versus suppressive immune responses. Cryobiology. 2009 Feb;58(1):1-11.
15. Nakada SY, Jerde TJ, Warner T, Lee FT. Comparison of cryotherapy and nephrectomy in treating implanted VX-2 carcinoma in rabbit kidneys. BJU Int. 2004 Sep;94(4):632-6.
16. Nakada SY, Jerde TJ, Warner TF, Lee FT Jr. Comparison of radiofrequency ablation, cryoablation, and nephrectomy in treating implanted VX-2 carcinoma in rabbit kidneys. J Endourol. 2004 Jun;18(5):501-6.

Appendix D

Nanoparticle Preconditioning in an Immunocompetent (TRAMP-C2) Preclinical Model of Prostate Cancer

This section describes preliminary attempts to develop the TRAMP-C2 preclinical tumor model to investigate nanoparticle preconditioning mediated enhancement of cryosurgery.

D.1. INTRODUCTION

Although our lab has extensive experience working with the DSFC model in athymic nude mice, we have not yet worked with an immunocompetent murine model for assessing thermal therapies. Athymic nude mice are deficient in T cells which are an important component of the inflammatory response following thermal therapy. A model using cells capable of metastasizing in immunocompetent mice will more closely reflect the human situation and improve clinical application of nanoparticle preconditioning. In particular, more work is needed using poorly differentiated metastatic tumors since, in humans, nanoparticle preconditioning enhanced thermal therapy will likely have its greatest and most immediate impact in patients with high grade tumors with significant probability for local failure (recurrence) and metastasis.

One of the best characterized and widely used mouse models of prostate cancer is the TRAMP model. It targets the prostate epithelium using a tissue-specific probasin (PB) promoter that drives the expression of SV40 T antigen (Tg), and leads to progressive disease from epithelial hyperplasia to prostatic intraepithelial neoplasia (PIN) and adenocarcinoma with both local and disseminated disease [1, 2]. The versatility of the TRAMP model has been extended further by the establishment of several TRAMP-derived prostate tumor cell lines (including TRAMP-C2) that can be injected into the syngeneic male C57BL/6 host to induce ectopic prostate tumorigenesis [3]. TRAMP-C2 cells metastasize to regional lymph nodes and other organs following an interval of

chronic primary tumor growth. Following primary tumor resection in this model, metastatic recurrence occurs at a high rate (i.e., >95% of mice) and in a predictable pattern [4]. Metastatic recurrence in this model emanates from the outgrowth of established nodal micrometastases that are present at the time of primary tumor resection. Hence, metastatic disease progression is not a consequence of seeding. Furthermore, this model mimics the clinical paradigm in which distant metastases represent the direst consequence of surgical treatment failure. Because of these attributes, this model readily lends itself to the testing of adjuvant therapies for their ability to eliminate poorly differentiated metastatic prostate cancer in immunocompetent host.

Our goal with these set of experiments was to establish the TRAMP-C2 model in our lab to study the effects of nanoparticle preconditioning and subsequent enhancement of thermal therapy in this preclinical immunocompetent tumor model.

D.2. MATERIALS AND METHODS

TRAMP-C2 Cell Culture

The TRAMP-C2 cell line was purchased from ATCC (Manassas, VA). These cells grow as adherent monolayers in T-flasks. Cells were grown in ATCC-modified DMEM (ATCC, Manassas, VA) supplemented with 5% FBS, 5% Nu-Serum V, 100 U/ml penicillin, 100 µg/ml streptomycin, 5 µg/ml insulin and 0.01 nM dihydrotestosterone. Cultures were maintained in a 37°C/5% CO2/95% humidified air environment. Cells

were subcultured (1:14) once or twice/week, by rinsing flasks with Hank's balanced salt solution (HBSS), followed by trypsinization, enzyme neutralization, and reseeding.

DSFC/tumor implantation, nanoparticle administration, cryosurgery and vascular stasis measurement

Male NU/J and C57BL/6J mice were obtained from the Jackson Laboratory (Bar Harbor, ME). Experiments were performed when mice were 6-8 weeks old. The dorsal skin fold chamber (DSFC) was implanted and 1-2 million TRAMP-C2 cells suspended in PBS were implanted (see DSFC implantation, tumor implantation, Chapter 2). Prior to DSFC implantation on C57BL/6J mice, hair was removed from the dorsal skin surface by treatment with Nair (Church & Dwight Co., Inc.). CYT-6091 (5 µg TNF) was injected via tail vein 4 hours prior to cryosurgery. At 4 hours after CYT-6091 administration the cryosurgery procedure was performed (see DSFC cryosurgery, Chapter 2). Stasis radius was measured at day 1, 3 and 7 post cryosurgery (see vascular stasis measurement, Chapter 2). Animals were sacrificed at day 7 after stasis radius measurement and The entire tumor tissue within DSFC was processed and stained with hematoxylin-eosin (H&E) (see Histology and Immunohistochemistry, Chapter 3).

D.3. RESULTS

The TRAMP-C2 tumor cells grew well in DSFCs of both NU/J and C57BL/6J mice. However, it was not possible to maintain the DSFC preparation in C57BL/6J mice for

more than a week after implantation. Implantation of DSFCs in C57BL/6J mice resulted in severe scratching by the mice of the skin around the chamber resulting in bleeding and infection. These mice had to be sacrificed before any thermal therapy could be administered. No such issues were encountered with the NU/J mice.

Intravital vascular stasis measurements made after cryosurgery in DSFC TRAMP-C2 tumors grown in NU/J mice decreased continuously from Day 1 to Day 7 (**Figure D.1**). The maximum stasis area post cryosurgery of 36.42 ± 2.96 mm^2 was observed at Day 1 and decreased to 23.85 ± 2.62 mm^2 at Day 3 and 10.87 ± 1.67 mm^2 at Day 7. This trend was also seen with CYT-6091 preadministration 4 hours prior to cryosurgery. In this group, the maximum stasis area of 40.02 ± 2.51 mm^2 was observed at Day 1 which decreased to 27.69 ± 1.86 mm^2 at Day 3 and 3.84 ± 1.45 mm^2 at Day 7. Only the Day 7 timepoint was statistically higher than the cryosurgery alone group ($p = 0.02$). Day 7 histology of the cryolesion showed a central necrotic zone immediately adjacent to the cryoprobe tract, characterized by intense eosinophilic staining of cells, loss of hematoxylin staining and loss of cellular detail (**Figure D.2**). No blood vessels were observed in the central necrotic zone. Viable tumor tissue was present close to the edge of the DSFC. A distinct band of inflammatory cells characteristic of cryosurgical lesions was not readily identifiable, however, a zone of thrombosis and hemorrhage and ischemic necrosis was evident between the zone of central necrosis and viable tumor tissue.

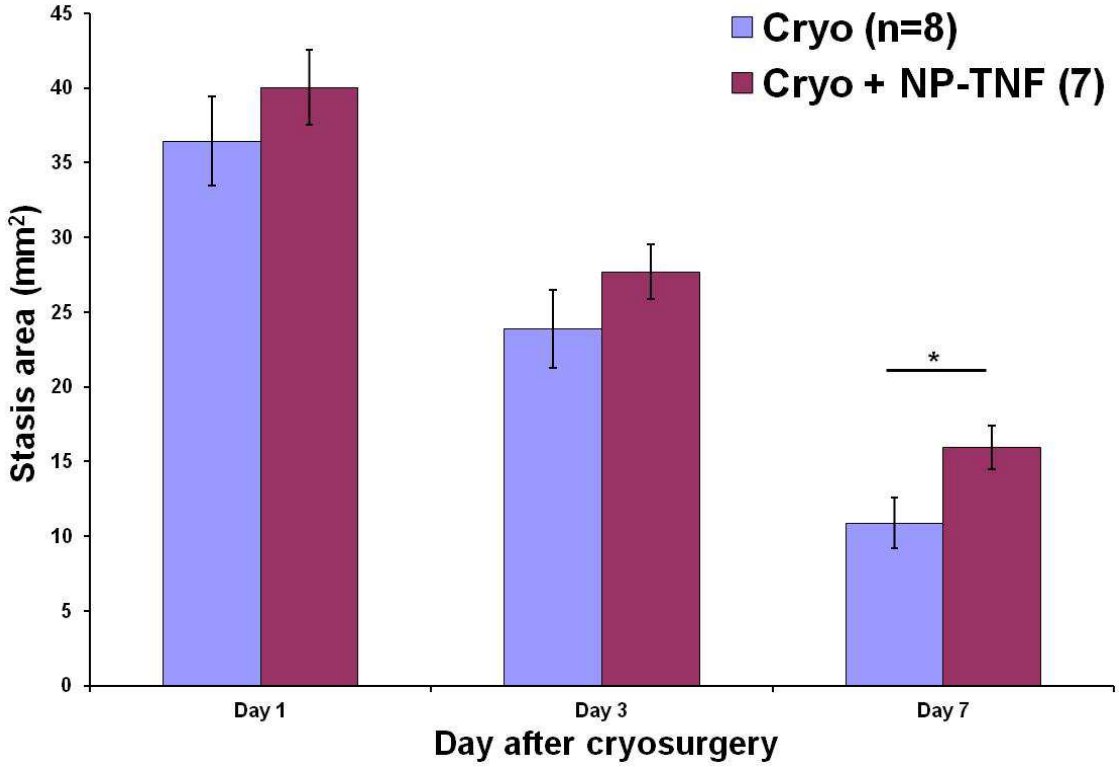

Figure D.1. Effect of nanoparticle preconditioning on cryosurgery of TRAMP-C2 tumors grown in DSFC of NU/J mice. NP-TNF (CYT-6091, 5 µg TNF) was administered 4 hours prior to cryosurgery. Values presented are mean ± SE from 7-8 animals in each group. Stasis areas were statistically higher in the NP-TNF group at Day 7 (*, p=0.04).

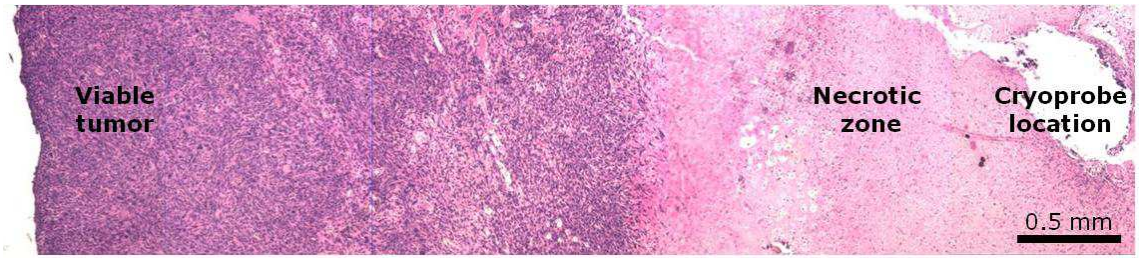

Figure D.2. Histology (H&E stain) of TRAMP-C2 tumor grown in DSFC of NU/J mice at Day 7 after cryosurgery.

D.4. DISCUSSION

The evolution of the cryosurgical lesion in TRAMP-C2 tumors was markedly different compared to our previous work in the DSFC LNCaP tumor model [5, 6]. The maximum stasis area after cryosurgery occurs at Day 3 after cryosurgery in the DSFC LNCaP tumor model due to the actions of inflammatory cells that infiltrate the lesion and extend the direct cell injury caused by the freeze-thaw event [5, 6]. The trend seen in our results with the TRAMP-C2 model is similar to cryosurgical injury of normal skin in the DSFC which also displays a continuously diminishing vascular stasis area following cryosurgery due to the wound healing response (wound contraction) which is delayed in the presence of LNCaP tumor cells [6]. Our Day 7 histology results confirm the presence of TRAMP-C2 tumor cells in the DSFC along with the typical histological zones concentric to the cryoprobe tract characteristic of a cryosurgical lesion [6]. Hence the decreasing trend of the stasis area is likely due to the rapid growth kinetics of the TRAMP-C2 cell line compared to the LNCaP cell line. Also, the growth of the TRAMP-C2 cell line would be even more rapid in nude mice lacking T cells used in the study. This trend of tumor growth kinetics overwhelming the wound healing and inflammatory cell response to cryosurgical injury is similar to that observed in the VX2 tumor in the rabbit kidney model (see Discussion, Appendix C) and acts as a confounding factor when comparing the effect of CYT-6091 preadministration with cryosurgery alone. Even so, a statistically significant higher stasis area was obtained at Day 7 in the CYT-6091 group implicating a beneficial role of nanoparticle preconditioning in enhancing cryosurgery in this aggressive tumor model. Future investigations geared towards overcoming the technical

difficulties of maintaining the DSFC preparation in C55BL/6J mice for an extended period (2.5-3 weeks) are needed to continue developing this immunocompetent preclinical model to understand the role of the adaptive immune response, specifically T cells, in nanoparticle preconditioning.

D.5. REFERENCES

1. Gingrich JR, Barrios RJ, Morton RA, Boyce BF, DeMayo FJ, Finegold MJ, Angelopoulou R, Rosen JM, Greenberg NM. Metastatic prostate cancer in a transgenic mouse, Cancer Res 1996 (56) 4096-102.
2. Hurwitz AA, Foster BA, Allison JP, Greenberg NM, Kwon ED. The TRAMP mouse as a model for prostate cancer, Curr Protoc Immunol 2001 20.5.1-20.5.23.
3. Frost GI, Lustgarten J, Dudouet B, Nyberg L, Hartley-Asp B, Borgstrom P, Novel syngeneic pseudo-orthotopic prostate cancer model: vascular, mitotic and apoptotic responses to castration, Microvasc Res 2005 (69) 1-9.
4. Kwon ED, Foster BA, Hurwitz AA, Madias C, Allison JP, Greenberg NM, Burg MB. Elimination of residual metastatic prostate cancer after surgery and adjunctive cytotoxic T lymphocyte-associated antigen 4 (CTLA-4) blockade immunotherapy, Proc Natl Acad Sci U S A 1999 (96) 15074-9.
5. Goel R, Swanlund D, Coad J, Paciotti GF, Bischof JC TNF-alpha-based accentuation in cryoinjury--dose, delivery, and response. Mol Cancer Ther. 2007 Jul;6(7):2039-47
6. Jiang J, Goel R, Schmechel S, Vercellotti G, Forster C, Bischof J. Pre-conditioning cryosurgery: cellular and molecular mechanisms and dynamics of TNF-α enhanced cryotherapy in an in vivo prostate cancer model system. Cryobiology. 2010 Dec;61(3):280-8.